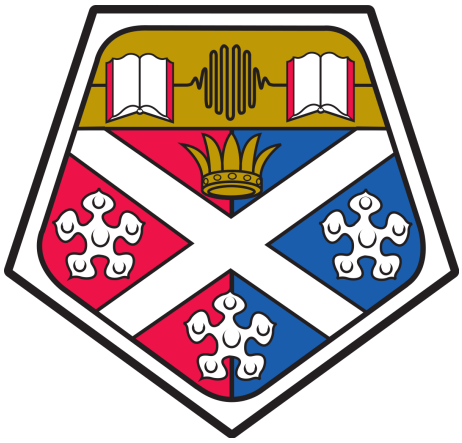

Quantum Information Scrambling in Tunable Range Quantum Spin Models

PhD Thesis

Sridevi Kuriyattil

Quantum Optics and Quantum Many-Body Physics

Department of Physics

University of Strathclyde, Glasgow

This thesis is the result of the author's original research. It has been composed by the author and has not been previously submitted for examination which has led to the award of a degree.

Abstract

Quantum information scrambling refers to the spreading of initially localised information across a system's many degrees of freedom, generating many-body entangled states. The fastest known scramblers achieve this at a timescale that grows logarithmically with the system size N and black holes are conjectured to saturate this bound. Such fast scramblers are also potentially useful for generating resource states within the system's coherence time. This thesis investigates efficient entanglement generation using models with tunable-range interactions, allowing interpolation between different geometries with varying notions of locality. We show that this crossing between the geometries leads to a dynamical phase transition, marking the onset of fast scrambling in quantum circuits with different levels of long-range connectivity. This enables the identification of regimes where resource states can be generated on timescales of $O(\log N)$, allowing the relevant system sizes to grow exponentially with coherence time. We further demonstrate the utility of states generated from sparse coupling graphs in quantum-enhanced metrology. We show both analytically and numerically that in certain regimes, sparse graphs can emulate dynamics associated with dense all-to-all coupling, with example applications including generating states with Heisenberg scaling for quantum metrology. We also propose models to implement both the dynamical transition and generation of metrologically relevant states in neutral atom arrays with the aid of tweezer-assisted shuffling operations. With these results, we provide a solid foundation for further exploration of the rich physics and applications that sparse coupling graphs with tunable-range interactions have to offer.

Dubito, ergo sum, vel, quod idem est, cogito, ergo sum.

René Descartes

Contents

Acknowledgements

In the grand tradition of procrastination, I finally find myself writing this acknowledgment section, possibly the most crucial and longest part of my thesis. This section is also meant to be long because I am pretty sure I wouldn't have completed my PhD without a lot of support from many people. First and foremost, I want to express my deepest gratitude to my advisor, Andrew Daley, for the incredible opportunity to be part of the QOQMS group and for everything you have offered me over the past three years. Thank you for your wisdom, patience, and confidence in me throughout this PhD. I am especially grateful for the many opportunities you provided, from traveling to new places and attending conferences to engaging in meaningful scientific discussions with researchers I had only known through their academic papers. I also feel incredibly fortunate to have been warmly welcomed into Jonathan Pritchard's lab group. The discussions I had with Jon always left me motivated and energized. Thank you so much, Jon, for your support and encouragement!

I was fortunate to begin my PhD as part of an ongoing project with Tomohiro Hashizume and Gregory Bentsen, and I cannot thank both of you enough for your unwavering support throughout the project and beyond. Greg, thank you for your incredible ability to break down the most complex mathematical problems into simple, understandable terms. And Tomohiro, thank you for your endless patience, no matter how many times I asked the same question. In the second half of my PhD, I was lucky to work with Pablo Poggi and Johannes Kombe, and I'm grateful that we are still collaborating today. I can't express enough how much it meant to me that both of you welcomed all my ideas without the slightest hesitation and were always eager to explore something new.

Thank you also for pushing me to create better figures—it truly made a difference! I would also like to thank my viva committee, Silvia Pappalardi, Viv Kendon, and Alison Yao, for organising my viva, engaging in insightful discussions, and providing constructive feedback on my thesis.

QOQMS is indeed a massive group, and I am truly grateful for that. Having traveled a long way from home, I gradually began to feel like part of this vast, nerdy family that shares a love for books, comics, and, of course, board games. Sebastian and Ewen, I'm so glad to have had you as fellow travelers on my PhD journey. I'm extremely thankful for all the conversations we had—whether they were about science or not. Sebastian, I cherished our time exploring Oxford together, and Ewen, our time in Las Vegas for the APS March meeting was a great experience. A big thank you to Gerard and Tomas for all the insightful work-related discussions. Tomas, those crazy bad movie nights were a blast, and Gerard, I'll always remember our hikes in the Highlands with fondness. I also want to express my sincere gratitude to Grant for always being in the office and helping me a lot during my writing phase. I also want to thank Simon, Lorenzo, Alessandro, Kathryn, Peter, Callum, Tom, Stuart, and Elliot. You are all incredibly talented physicists, and your graciousness and patience have meant so much to me. I am incredibly grateful to Ieva, Rosaria, and Natalie for all the great chats about physics, the awesome gym sessions, and for supporting me throughout my PhD journey. A special thanks, of course, to Elmer the pup and Bailey the Scot cat for being the best companions. Emanuele, thank you for bringing the sunshine from Italy to Glasgow. The past two years of knowing you, talking to you, and working together on physics have been an incredible experience. To Ryan, thank you for your help with tensor networks and for your constant encouragement. The last few months of thesis writing wouldn't have been nearly as sane without you. 🐰🐰 And yes, I'm pretty sure I can sneak a rabbit emoji into my PhD thesis!

While the acknowledgment page of a thesis typically focuses on academic contributions, I wouldn't have completed this journey without the support of many wonderful

people. I remember meeting Elita at a DRG social, and our immediate connection led to memorable study sessions, tiny celebrations of our wins, and writing retreats. Giorgia, Arundhathi, and Megan, thank you for the movie nights, lunch dates, and birthday celebrations—they were crucial in keeping me grounded. A special thanks to my best friends Amrita and Shobhna, whose constant support and welcoming presence made me feel at home and offered me those much-needed breaks. Krishnaprasad, the greatest fluid mechanician in the world, thank you for believing in me, sharing nerdy memes, pushing me to think outside the box, and for handling countless proofreading duties. My heartfelt thanks also go to Rukmani, without whom I don't think I would have survived the pandemic and prepared myself for this PhD journey. This acknowledgment section wouldn't be complete without mentioning Greshma, Harsha, Greeshma, and Fathima. Greshma, I'm so grateful we're now in the same time zone! Thank you for listening to my late-night woes, helping with tough decisions, our artsy holidays, and being the pragmatic voice when needed. Harsha, since our time as roommates at IISER, you've been a constant source of encouragement and support. Greeshma, your subtle yet impactful encouragement was a lifeline during some of the toughest moments of my PhD, and our yearly trips keep me motivated. Fathima, thank you for your constant reassurance during my imposter syndrome and for flying from Canada to meet me during conferences. I cherish everything you've all done for me—thank you!

To my mother Prasanna and father Sivasankaran, thank you for always believing in my potential and for your unwavering support. I remember my father encouraging me to "hitch my wagon to the stars," and I've done my best to follow that advice. Mom, your example of perseverance has been a guiding light throughout these three years. To my brother Appus, I love you, and I'm deeply grateful for being the support I needed at times. Finally, I want to extend my heartfelt thanks to the Department of Physics at the University of Strathclyde and the administrative staff for their assistance with travel plans and for ensuring a smooth journey throughout my PhD. To everyone who has been a part of this journey, your support has been invaluable. Honestly, none of this would have been possible without each and every one of you!!

List of Figures

List of Figures

Chapter 1

Introduction

> Invention, it must be humbly admitted, does not consist in creating out of void, but out of chaos
>
> Mary Shelley, Frankenstein (1831)

The spreading of information is a phenomenon deeply embedded in our daily lives and is not just native to quantum mechanics. Information spreading is central to human interactions, driving the dissemination of ideas, knowledge, and innovations. Thanks to the ever-increasing use of social media platforms, how information spreads through society has changed significantly over the past decade. Just as information proliferates through social networks and communities, it also has the capacity to distort, giving rise to the rapid spread of misinformation. In such a scenario, once the source of information is lost or corrupted, reconstructing the original message becomes nearly impossible, leading to lasting confusion and misunderstanding. In social contexts, individuals or groups become interconnected through shared information, beliefs, and experiences. Over time this sharing of information creates complex networks of influence, much like the complex network connections we consider here in quantum systems.

In quantum systems, the spreading of information may be attributed to dynamical

coupling that leads to a build-up of entanglement in the system. Quantum entanglement plays a crucial role in a wide range of phenomena, from the thermalisation dynamics of closed quantum systems [1–3] to the foundations of quantum computing [4–7] to quantum metrology [8–14] and even the dynamics of black holes [15–18]. Despite the significant progress in understanding these phenomena and developing useful quantum algorithms that exploit entanglement, much remains unexplored in this complex field [19]. One of the helpful frameworks in navigating this intricate landscape is the concept of *quantum information scrambling* [15–17, 20, 21].

1.1 Quantum Information Scrambling

What exactly is meant by quantum information *scrambling*? It is a process in which initially localised quantum information spreads throughout a quantum system, becoming inaccessible to local measurements. The mechanism responsible for the loss of information from local measurements is the generation of entanglement between the objects in the quantum system. For instance, consider a system of qubits, where qubits are the quantum analogs of traditional binary bits, 0s, and 1s [7, 22]. Initially, the information is encoded in a locally accessible state. During the scrambling process, the state undergoes time evolution driven by some random unitary operator U. As a result, the information becomes highly delocalised across the entire system. Importantly, no information is lost during this process; it is merely hidden from local measurements. This is because the operator is unitary and therefore the dynamics are reversible simply by applying the adjoint $U^{\dagger}$.

There are several mathematical definitions of scrambling that can be used interchangeably. The definition mentioned by Lashkari *et al.* describes how initially distinguishable states evolve to become indistinguishable, which characterises the dynamics of the system rather than the quantum state itself [20]. Although this definition makes no explicit mention of entanglement, the indistinguishability of states is related to the presence of many-body entanglement [20]. In contrast, a state-centric notion of scrambling can be defined using the concept of the Page limit [17], which relates to the entropy of

subsystems, and which we discuss in detail in Ch. 2 (see Eq. (2.4)). The crucial point here is that a state is Page-scrambled if, for any subsystem, there is maximal entanglement with the rest of the system. Thus, if two distinguishable states both saturate to the Page limit due to the dynamics of the system, it indicates that the system has scrambled these states, resulting in complex entanglement throughout.

Understanding the speed at which information scrambles in a quantum system is crucial because it directly impacts how quickly entanglement can be generated. This knowledge is particularly relevant in noisy quantum devices, where the goal is to create entangled resource states within a limited coherence time. By knowing how fast scrambling and entanglement generation occurs, we can better engineer these states before decoherence sets in, which is essential for achieving reliable quantum computation and simulation [23–27]. For a system of N particles, the scrambling time t is the time required for initially localised information to spread across all N particles. In quantum systems defined on regular lattices in D dimensions, $t \propto N^{1/D}$ [28]. For so-called "fast scramblers", the scrambling time scales $t \propto \log N$. The *fast scrambling conjecture* proposes that fast scramblers are the fastest dynamic processes, capable of spreading information across the system within this logarithmic timescale, and black holes are conjectured to saturate this bound [15, 16, 21, 29–35].

1.2 Fast Scrambling

Fast scramblers are quantum systems that achieve a conjectured upper bound on the speed limit ($t \propto \log N$) for information spreading in quantum systems. These timescales were initially studied in the context of the black hole information paradox [15, 36]. Susskind, Thorlacius, and Sekino calculated the timescale required for an observer outside a black hole to recover a quantum state from Hawking radiation, considering the constraints imposed by the no-cloning theorem. Their work suggests that black holes are conjectured to be fast scramblers [15, 16, 36]

An important element that enables the rapid spreading of information in quantum systems is the presence of non-local interactions. One of the early examples of Hamiltonian fast scramblers is the Sachdev-Ye-Kitaev (SYK) model [37–40], which is a model of Majorana Fermions with random nonlocal 4-body interactions. The SYK model is analytically solvable in the large N limit [38], thereby allowing one to compute the dynamics and show that quantum information is scrambled in the minimum possible time allowed by the fast scrambling conjecture. Interestingly, the SYK model also appears to have a close connection to specific models of black holes [41].

We can also construct quantum fast scramblers that are not a conventional Hamiltonian system [15, 16]. An important example is a quantum circuit model consisting of random two-qubit unitary transformations ("quantum gates") as shown in Fig. 1.1(a). This circuit model, also called a random all-to-all model allows the time evolution of a N qubit state by parallel application of the random two-qubit gates on $N/2$ non-overlapping pairs of qubits at each layer. The time is proportional to the number of circuit layers, also called the depth of the circuit. It is known that scrambling quantum information localised in a single qubit in this random all-to-all circuit model requires a number of circuit layers that scale as $O(\log N)$, making this model a fast scrambler [15, 16]. In addition to its theoretical importance, fast scrambling has attracted attention from experimentalists as well, particularly due to recent progress in atomic, molecular, and optical physics that enables the generation of non-local interactions in experimental platforms. Both conventional Hamiltonian systems and digital circuit models share a common element: *randomness* in long-range interactions. However, randomness is not a necessary condition for fast scrambling. As demonstrated in [33, 34], long-range spin interactions with additional symmetry-breaking terms can achieve fast scrambling. Moreover, a non-disordered spin model of sparsely connected spin-$1/2$ particles, as described in [30], also exhibits fast scrambling.

These results highlight that deterministic fast scramblers are feasible, providing exciting possibilities for experimental realisations as we will discuss in Sec. 1.4.

1.3 Quantum Information Scrambling in Sparsely Coupled Graphs

In this thesis, we study quantum information scrambling in sparsely coupled graphs, as proposed by Gubser *et al.* [45]. The model interpolates between two incompatible geometries: linear and treelike. The main distinct factor between these two geometries is that they have different notions of locality. The idea of locality is based on the effect of a change in a particular point on the rest of the system. This change affects its immediate neighbours. To fully understand this, let us consider the all-to-all model discussed in Sec. 1.2. Here, there is no geometric notion of locality whatsoever, this is because all the qubits are connected to all others.

In the case of linear geometry (Euclidean geometry) as illustrated in Fig. 1.1(b), a perturbation at site 0 will first travel to site 1 and then to further neighbours. So the perturbation propagates in space, starting from the points that have the smallest Euclidean distance and moving to the points with the largest Euclidean distance from the initial site. By contrast, in the case of treelike geometry (p-adic geometry, where p is a prime number), the notion of locality and distance is governed by the definition of p-adic distance, discussed in detail in Sec. 5.2. But the main point is that it depends on the number of branches of the tree between the two qubits shown in Fig. 1.1(b). Thus some points that are far away in the linear geometry are close in the treelike geometry. This incompatibility between the notion of locality between these two geometries motivated Gubser *et al.* to study a sparsely coupled model with $p = 2$ as depicted in Fig. 1.1(b) (middle), which we also call the *powers of two (PWR2) model* as the edges or interactions are present if and only if the site indices differ by an integer value of two. Gubser *et al.* observed similarities between the p-adic field theory and a model on the PWR2 graph defined by the Hamiltonian

$$H = \sum_{ij} \chi_{\mathrm{sp}}(i \quad j)\phi_i\phi_j \quad \sum_j \phi_j, \tag{1.1}$$

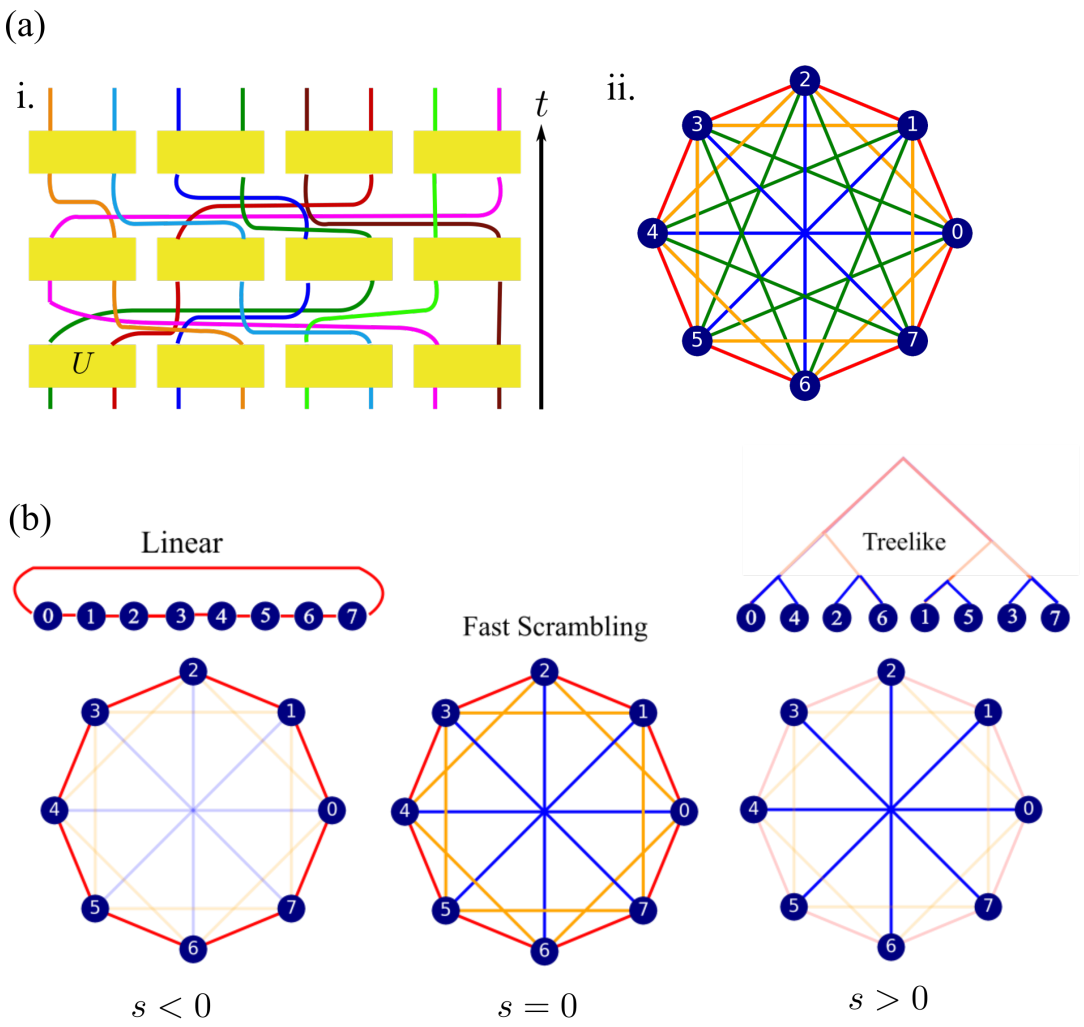

Figure 1.1: **Examples of Fast Scramblers** (a) i. Random all-to-all circuit model, where each qubit connects to every other qubit. The qubits evolve via random two-qubit gates (yellow rectangles) with $N/2$ randomly selected qubit pairs coupled simultaneously per layer. Each qubit's world line is shown in a distinct colour. (a) ii. The corresponding graph representing the all-to-all connectivity of qubits. (b). Two incompatible geometries in the sparsely coupled PWR2 model for $N = 8$: linear (left) and treelike (right). Blue circles represent vertices, and lines represent edges; line crossings are incidental and carry no physical meaning. The tunable parameter s, allows a smooth interpolation between these two geometries according to Eq. (1.2). For $s < 0$, vertices separated by smaller powers of two couple more strongly, as shown by the opacity of the edges. For $s > 0$, vertices separated by larger powers of two couple more strongly. At $s = 0$, vertices separated by integer powers of two are coupled with equal strength, representing a fast scrambling regime [30, 42–45].

where ϕ is a real scalar field, and

$$\chi_{\mathrm{sp}}(i \quad j) = \begin{cases} ji \quad jj^{s} & \text{when } ji \quad jj = 2^{m}, m = 0, 1, 2, \ldots, \\ 0 & \text{otherwise.} \end{cases} \tag{1.2}$$

By tuning the parameter s 2 R, the model can be smoothly interpolated between the two geometries. When s ! 1 , the model converges to the nearest-neighbour model in the linear geometry Fig. 1.1(b) (left). In contrast, as s ! + 1 , it converges to the nearest-neighbour model in the treelike geometry Fig. 1.1(b) (right). This smooth transition forms the basis for much of the analysis in this thesis, where we also explore how such changes in the underlying geometry occur in fully quantum mechanical systems. At s = 0, where the geometry is neither linear nor treelike, fast-scrambling dynamics emerge. We further show that, in this regime, fast scrambling can be observed without the need for random interactions.

1.4 Towards Experimental Observation of Scrambled States

We have discussed that there is no requirement for random interactions, rather non-local couplings between spins can also lead to fast scrambling dynamics [30, 33–35, 42]. This has sparked interest among experimentalists as it provides a way to create entangled resource states within the coherence time. Technological advancements in atomic, molecular, and optical physics have enabled the manipulation of atoms and photons possible. This includes the ability to coherently control and transport atoms while minimising decoherence, which is crucial for building scalable quantum information systems. Examples of such systems include trapped ions [46–52], neutral atom arrays [53–58], atoms in optical cavities [59–62], and solid-state systems [63–66].

In optical cavity experiments, non-local long-range interactions have been experimentally demonstrated by programming spin-exchange interactions in an array of atomic ensembles in the atomic cavity. Usually, the cavity-mediated interactions create all-to-all connectivity, however, the introduction of a magnetic field gradient breaks this

and allows frequencies of optical drives to control the spins that need to be coupled [59]. Techniques have also been explored using trapped ions or atoms to create different geometries by tailoring the frequency spectrum of a drive field [30, 48, 49].

One other promising platform is the ensemble of neutral atoms (Rydberg atoms) equipped with optical tweezers. The shuffling operations generated by the optical tweezers explore rich geometries that can generate fast scrambling. $D = \log_2 N$ dimensional hypercube, which is a sparse graph and generate fast scrambling as suggested by Susskind and Sekino [15] is native to Faro shuffling operations that can be generated using the optical tweezers (see Sec. 6.4). This remarkable flexibility in atom manipulation along with good scalability, and coherent control of each atom, makes neutral atom arrays a powerful platform for quantum information processing [53, 58, 67–74], and quantum simulations [54, 56, 57, 75, 76]. In this thesis, we focus on studying the scrambling dynamics more on the sparse models that are native to the neutral atom platforms.

1.5 Thesis Overview

Building upon Gubser's work on p-adic field theory [45], which introduced a smooth interpolation between two incompatible geometries, we extend the investigation into sparse coupling models, particularly focusing on the intersection between these geometries. This crossover point gives rise to fast scrambling dynamics, and prior work has already demonstrated the feasibility of constructing deterministic fast scramblers at this crossover point without relying on random interactions [30, 35]. In this thesis, we demonstrate that this transition in geometry is also reflected as a dynamical transition, marking the onset of fast scrambling. Furthermore, we propose investigating this transition on near-term experimental platforms, such as cold atom arrays in optical tweezers. As part of our exploration of sparse coupling graphs, we also demonstrate their potential utility in quantum-enhanced metrology, where the efficient generation of entanglement plays a crucial role.

The rest of the thesis is organised as follows. In the following three chapters, we introduce the background and tools required. In Ch. 2, we discuss various measures of quantum information scrambling. We introduce the concepts of lightcones, entanglement entropy, and tripartite mutual information. We establish how the negativity of the tripartite mutual information serves as an indicator of many-body entanglement in the system. By the end of Ch. 2, we also try to understand the interplay between scrambling, chaos, and thermalisation. In Ch. 3, we introduce central concepts related to quantum-enhanced metrology. First, we review the classical and quantum Fisher information (QFI) to quantify how much information the measurable data contains about an unknown parameter. We also discuss how metrologically relevant states can be generated using spin squeezing. Finally, in Ch. 4, we introduce the numerical methods that are used to study the scrambling dynamics in this thesis. These three chapters provide the foundation and framework for the analyses in later chapters.

In Ch. 5, we examine the connection between geometry, entanglement build-up, and lightcones. Our approach involves studying a family of random circuits on sparse coupling graphs with a parameter that changes the probability distribution for choosing two-site gates as a function of distance. By tuning this parameter, we observe a transition in the underlying geometry of the model—from linear to treelike—accompanied by the emergence of a fast scrambling regime at the crossover between these geometries. We show that this transition is reflected in the entanglement structure of states that appear in the dynamics.

The crossover regime offers a compelling region for the exploration of interesting physics, and we will further investigate the transition between the geometries in Ch. 6. We identify a dynamical transition marking the onset of scrambling in quantum circuits with varying degrees of long-range connectivity. Specifically, we demonstrate that as a function of the tunable parameter and on a timescale of $O(1)$, the tripartite mutual information exhibits a scaling collapse around a critical point, distinguishing two regimes with different dynamical behaviours. This transition is evident in both sparse and

dense circuit models, and we observe similar features regardless of whether the model functions as a deterministic or random scrambler. To gain an analytical understanding, we also study an associated Brownian circuit model, mapping it to a long-range Ising model within a particular region of parameter space. This transition has practical applications in noisy devices, especially in identifying regimes where resource states can be generated on shorter timescales, staying within the relevant coherence time.

Sparse coupling graphs with limited connectivity have been shown to generate entanglement efficiently. Quantum states with extensive multipartite entanglement are a valuable resource for quantum-enhanced metrology. However, the robust generation of such states in unitary dynamics typically requires all-to-all interactions among particles. In Ch. 7, we demonstrate that optimal states for quantum sensing can be generated with sparse interaction graphs featuring only a logarithmic number of couplings. We show that certain sparse graphs can mimic the dynamics of all-to-all models, even for larger system sizes. Furthermore, we propose that these states can be efficiently produced in neutral atom arrays through dynamical shuffling of the atoms.

Finally, in Ch. 8, we summarise our findings and present an outlook on potential directions for future research.

1.6 Contributions During the PhD

The author of this thesis has contributed to the following publications and presentations for the completion of this PhD.

1.6.1 Publications on Work Related to the Thesis

- Tomohiro Hashizume, Sridevi Kuriyattil, Andrew J. Daley, and Gregory Bentsen, "Tunable Geometries in Sparse Clifford Circuits", Symmetry **14**, 666 (2022) [42].

  The author of this thesis has produced data for Figure 1, has written sections 2 and 3, and has contributed to the various parts of the main text. The author of

this thesis has also written sections C and D in the appendix. This is presented in Ch. 5.

- Sridevi Kuriyattil, Tomohiro Hashizume, Gregory Bentsen, and Andrew J. Daley, "Onset of Scrambling as a Dynamical Transition in Tunable-Range Quantum Circuits", PRX Quantum **4**, 030325 (2023) [44].

  The author of this thesis has produced all the data except for Figure 1, has written sections I and IV, and has contributed to the various parts of the main text. The author of this thesis has also written sections A, C, D, and E of the Appendix. This is presented in Ch. 6

- Sridevi Kuriyattil, Pablo Poggi, Johannes Kombe, and Andrew J. Daley, "Sparse graphs for quantum-enhanced metrology", *In preparation*

1.6.2 Presentations and Posters on Work Related to the Thesis

- **Presentation:** *"Onset of scrambling as a dynamical transition in tunable range circuit models"*, APS DAMOP, Forth Worth, Texas (June 2024)
- **Presentation:** *"Quantum Information scrambling in tunable range circuit models"*, Quantum Simulation Mini-Workshop, University of Oxford (February 2024)
- **Presentation:** *"Quantum Information scrambling in tunable range circuit models"*, DesOEQ/QSUM, University of Strathclyde (July 2023)
- **Presentation:** *"Onset of scrambling as a dynamical transition in tunable range circuit models"*, APS March Meeting, Las Vegas (March 2023)
- **Poster:** *"Onset of scrambling as a dynamical transition in tunable range circuit models"*, AQC, University of Strathclyde (June 2024)
- **Poster:** *"Onset of scrambling as a dynamical transition in tunable range circuit models"*, IQTN, University of Strathclyde (January 2024)
- **Poster:** *"Tunable Geometries in Sparse Clifford Circuits"*, DesOEQ/QSUM, University of Strathclyde (July 2022)

1.6.3 Other Publications

- Aparna Sreedharan, Sridevi Kuriyattil and Sebastian Wüster, "Hyper-entangling mesoscopic bound states," New Journal of Physics, **25**, 083028 (2023)

- Aparna Sreedharan, Sridevi Kuriyattil, Sarthak Choudhury, Rick Mukherjee, Alexander Streltsov, and Sebastian Wüster, "Solitary waves explore the quantum-to-classical transition," EPL, **140**, 35003 (2022)

Chapter 2

Measures of Quantum Information Scrambling

> Imagination is the Discovering Faculty, pre-eminently. It is that which penetrates into the unseen worlds around us, the worlds of Science
>
> Ada Lovelace

2.1 Introduction

The concept of entanglement traces its roots back to 1935 when Erwin Schrödinger introduced it in a letter to Albert Einstein [77]. This followed the publication of a seminal paper by Albert Einstein, Boris Podolsky, and Nathan Rosen, which presented a thought experiment now famously known as the EPR paradox [78]. Schrödinger coined the term Verschränkung (which he translated as entanglement) to describe the peculiar correlations between two particles that interact and subsequently separate, as illustrated in the EPR experiment. This concept laid the foundation for a significant area of study, extending the classical definition of entropy—originally introduced phenomenologically by Rudolf Clausius in the early 19th century within the context of

the thermodynamics of heat engines [79]. The idea was further developed by pioneers like Ludwig Boltzmann [80], Claude Shannon [22], and John von Neumann [81], who expanded its implications into the disciplines of statistical mechanics and information theory.

In Ch. 1, we introduced the concept of quantum information scrambling, which refers to the loss of quantum information such that it becomes inaccessible to local measurements. For a quantum system to become scrambled, correlations must build up between all N particles. This process inevitably leads to the build-up of entanglement. Theoretically, the build-up of these correlations can be quantified using various tools, and this chapter is dedicated to discussing the methods employed to measure quantum information scrambling. The rest of the chapter is structured as follows: In Sec. 2.2, we introduce the theory of quantum entanglement entropy and explore how its scaling with system size can be utilized to study both scrambling and the underlying geometry of quantum systems. Next, in Sec. 2.3, we examine how the spread of information manifests in a lightcone-like structure, reminiscent of the lightcones observed in relativistic theory, but different, as they arise from the structure of the system's dynamics, not from fundamental physical limits like the speed of light. Following this, in Sec. 2.4, we introduce another measure of information scrambling known as tripartite mutual information and discuss its significance in detecting scrambling. In Sec. 2.5, we address the differences and similarities between between three tightly related concepts: quantum information scrambling, quantum chaos, and thermalisation. Finally, the chapter concludes with a summary of the key ideas discussed in Sec. 2.6.

2.2 Quantum Entanglement Entropy

In quantum systems, the bipartite entanglement entropy measures the degree of entanglement between two subsystems. This is also called the bipartite von Neumann

entanglement entropy and is defined as

$$S_A = \mathrm{Tr}[\rho_A \log \rho_A], \tag{2.1}$$

where $\rho_A = \mathrm{Tr}_B(\rho_{AB})$ is the reduced density matrix of subsystem A, which is obtained by tracing out the degrees of freedom of subsystem B. The choice of base for the logarithm determines the units of entropy: base 2 yields entropy in bits, while the natural logarithm (base e) gives entropy in nats. Any given pure state $|\psi\rangle$, can be written as $|\psi\rangle = \sum_{i=1}^{m} \alpha_i |u_i\rangle_A |v_i\rangle_B$, using the Schmidt decomposition, where $|u_i\rangle_A$ and $|v_i\rangle_B$ are orthonormal states of subsystem A and subsystem B respectively. Thus, the reduced density of subsystem A is $\rho_A = \sum_i |\alpha_i|^2 |u_i\rangle_A \langle u_i|_A$ and the entanglement entropy is simply

$$S_A = \sum_i |\alpha_i|^2 \log |\alpha_i|^2. \tag{2.2}$$

This form also makes it clear that $S_A = S_B$. The Schmidt values follow $\sum_i |\alpha_i|^2 = 1$ and give us valuable insight into the entanglement properties of the system. If $\alpha_1 = 1$, and $\alpha_{i\neq 1} = 0$, then $|\psi\rangle = |u\rangle_A |v\rangle_B$ is a product state and thereby has zero von Neumann entanglement entropy. However, if all the α_i are equal, then the entropy is maximal. Hence, a large amount of entanglement between subsystems A and B is characterized by a flat distribution of Schmidt values. Studying the dynamics of entanglement growth has become particularly crucial in the study of many-body quantum systems out of equilibrium [4, 5, 7, 25, 82–86]. Hence, numerical methods to efficiently simulate these systems on classical computers are necessary, and this will be introduced in Ch. 4. To better understand these quantum systems, it is important to look at how entanglement scales as the system size grows.

2.2.1 Area Law and Volume Law Scaling

Having established the concept of quantum entanglement entropy, we now turn to a critical question: how does entanglement scale during the dynamics as the size of a quantum system increases? Two primary scaling behaviours, known as the area law

and the volume law, describe how entanglement entropy grows with system size. This behaviour may be linked to the properties of the energy spectrum of the system under study. For example, in 1-dimensional gapped systems, it is proven that the low-energy eigenstates of the Hamiltonian exhibit an entanglement entropy that follows area-law scaling [87–93]. This means that the bipartite entanglement entropy S_A of subsystem A increases proportionally to the area of the boundary of the region A, which in 1-dimensional systems is $S_A \propto O(1)$. A good example of a gapped Hamiltonian is a 1D transverse field Ising model

$$H = \chi \sum_i \sigma_i^z \sigma_{i+1}^z \quad h \sum_i \sigma_i^x, \tag{2.3}$$

where σ_i^z and σ_i^x are the Pauli matrices, χ is the coupling constant, and h is the transverse field. For $h > J$, the system has a non-zero energy gap between the ground state and the first excited state, making it a gapped Hamiltonian [90, 94]. In such systems, long-range correlations may not be expected in the low-energy regime, as the generation of long-range interactions in a local system typically requires excitations.

When a state that follows area-law entanglement scaling undergoes out-of-equilibrium quench dynamics-where a sudden change in a parameter of the Hamiltonian drives the system away from equilibrium-the initially localised quantum information, such as a spin excitation confined to a specific site or region, begins to spread across more distant sites. Specifically, for example, in systems that exhibit thermalisation, which will be introduced in Sec. 2.5, the entanglement entropy of a subsystem A reaches its maximal value. In such a scenario, the entanglement entropy grows with the system size, i.e., $S_A \propto |A|$, leading to what is called volume-law entanglement scaling, as the entanglement entropy is proportional to the volume of the region A. For a random state of N qubits, Page showed that the average entropy of the state is [1]

$$S_A = |A| \log 2 \quad \frac{1}{2} 2^{2|A| \quad |N|}, \tag{2.4}$$

[1] One can generalise this for any system with a local dimension D. Here, we consider qubits, and therefore $D = 2$.

where A is an arbitrary subsystem with $jAj < N/2$. This implies that the entanglement entropy of an arbitrary subsystem in such random state differs from the maximal by less than a single bit. The state that saturates this random state limit is called a Page-scrambled state [17] and is volume law entangled.

2.3 Lightcones and Information Spreading

In Sec. 2.2.1, we discussed different scaling of entanglement entropy with system size, emphasising the spreading of quantum information. In this section, we adopt an approach involving lightcones to further explore this phenomenon. Analogous to causal lightcones in relativistic theories, many-body lightcones limit the spread of quantum information. However, unlike relativistic lightcones, these arise from the specific structure of the system's dynamics, rather than from fundamental physical limits. Once the lightcone extends across the complete system (say, N spins or qubits), the quantum information becomes fully delocalised and is encoded in a many-body entangled state.

For 1-dimensional systems with only short-range interactions, this causal region is determined by the maximum velocity at which quantum information can spread, known as the Lieb-Robinson (LR) bound [28]. Information spreading can be studied by quantifying the degree of operator mixing, which is done by taking commutators between an operator P at site i at time $t = 0$ and an operator Q at site j at time $t = T$. The following inequality

$$jj[P_i(t = 0), Q_j(t = T)]jj \quad Ce^{\ \mu(d(i,j)\ \ vT)}, \tag{2.5}$$

sets a bound at a velocity v at which the information spreads, where $[.,.]$ is the commutator, $jj\,jj$ is the operator norm, $d(i,j)$ is the distance between sites i and j, and C and μ are constants. This means that for a pair of sites, i, j where $d(i,j) > vT$, the correlations are exponentially suppressed. Similar bounds can also be derived for systems with long-range and sparse interactions [32, 95–98]. Understanding the lightcone structure and the LR velocity is crucial for determining the timescales over which

entanglement and correlations are generated in quantum systems. By combining the scaling of the entanglement entropy with the LR bounds, it is established that if the subsystem A lies within the lightcone, the entanglement entropy exhibits a volume law scaling. Conversely, if A is outside the lightcone, the entanglement entropy follows an area law scaling. This relationship demonstrates that studying lightcones and the LR velocity provides valuable insights into the underlying geometry of the quantum system as we will discuss in Ch. 5. In systems with non-local interactions, the effective linear lightcone collapses allowing for fast scrambling, where system-wide entanglement builds up on timescales as short as $t \sim \log N$ [15, 20, 29–35]. In Ch. 5, we calculate this time for circuit models featuring sparse interactions of different strengths.

2.4 Tripartite Mutual Information

In the following section, we turn our attention to the tripartite mutual information as a key measure for studying quantum scrambling.

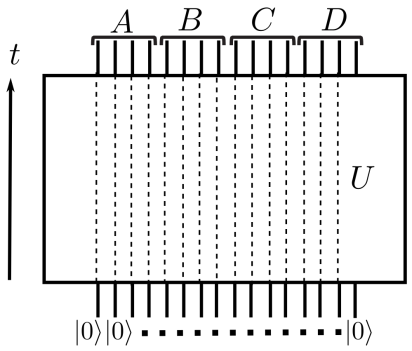

Figure 2.1: **Setup to Study Scrambling Using Tripartite Mutual Information** An initially separable state $|0\rangle^{\otimes N}$ undergoes time evolution under a unitary U, and the final state is divided into four contiguous subregions A, B, C and D. Due to the delocalisation of quantum information, the combined region BC contains more information about A, than the individual regions B and C do about A. This leads to a negative tripartite mutual information.

To understand this quantity, we refer to the Fig. 2.1. Here, an initial separable state $|0\rangle^{\otimes N}$, where N is the system size, undergoes a time evolution according to a given unitary U. We consider the system to be divided into four contiguous subregions A,

B, C and D as illustrated in Fig. 2.1. If U scrambles the system, the initial localised information cannot be retrieved by local measurements in the output state. This means that the mutual information $I(A;B)$, which measures the amount of information one can learn about a given subregion A by measuring the subregion B, must be small. This is mathematically given as

$$I(A;B) = S_A + S_B \quad S_{AB}, \tag{2.6}$$

where S_A, S_B, and S_{AB} are the entanglement entropies of the respective subregions. Similarly, $I(A;C)$ will also be small as C is also a local region. However, the combined region BC will have more information about A than B or C separately. This naturally allows us to combine all three mutual information and using Eq. (2.6) to construct

$$I_3 = I(A:B:C) = I(A;B) + I(A;C) \quad I(A;BC) \tag{2.7}$$

$$= S_A + S_B + S_C \quad S_{AB} \quad S_{BC} \quad S_{AC} + S_{ABC}. \tag{2.8}$$

This quantity is called the tripartite mutual information [21, 99–104][2]. I_3 vanishes when the regions ABC are uncorrelated, as the amount of information subregions B and C have about A is exactly equal to the information the combined region BC have about A. This is because the quantum information is localised. However, when quantum correlations have spread across the system, $I(A;BC) > I(A;B) + I(A;C)$ and $I_3 < 0$. This means that the information contained in the quantum state is delocalised across all three regions A, B, C and reconstruction of this information requires access to all of them. Hence, the negativity of the tripartite mutual information serves as a natural measure of many-body entanglement in the system [21, 99, 101, 103, 105].

For random states, we can show that the tripartite mutual information is typically negative. By applying the entanglement entropy from Eq. (2.4) into Eq. (2.8), it is

[2]The tripartite mutual information is also referred to as the topological entanglement entropy in the condensed matter community. However, we use the term "tripartite mutual information" in the thesis.

straightforward to see that for these states

$$I_3 = \frac{1}{2}\left[3\left(2^{4jAj\ \ N}\right)\quad 2^{6jAj\ \ N}\quad 3\left(2^{2jAj\ \ N}\right)\right] < 0. \tag{2.9}$$

This can be attributed to the monogamous nature of entanglement, which arises from the sub-additive property of entanglement entropy $S_{AB}\quad S_A + S_B$. In simple terms, quantum correlations between regions A and B cannot be shared with region C without spoiling the original entanglement. It has been shown that for holographic systems[3] the tripartite mutual information is always negative, i.e. $I_3\quad 0$. This is often referred to as monogamy of mutual information [21, 101, 103, 104]. However, in general quantum systems, there will be both quantum and classical correlations. In systems where classical correlations dominate, this monogamy does not hold. For example, permutationally symmetric (PS) states, such as the GHZ state, have a positive I_3. Permutation symmetry, which will be discussed in detail in Sec. 3.3.2, allows us to reduce the effective dimension of the Hilbert space to $N+1$, rather than 2^N, for a system of N qubits. One clear property of such states is that $S_A\quad \log(A+1)$ for a subsystem A, as the rank of the reduced density matrix is at most $A+1$. With this, we can estimate the behaviour of I_3 for a permutationally symmetric state. Using Eq. (2.8), we find that

$$I_3^{PS}\quad 3\log(A+1)\quad 3\log(2A+1)+\log(3A+1), \tag{2.10}$$

$$= \log\left[\frac{(3A+1)(A+1)^3}{(2A+1)^3}\right] > 0. \tag{2.11}$$

This approximation is valid for large N and A [21, 102]. Although we have omitted corrections here, this is enough to demonstrate the positivity of I_3. This means that the mutual information that A shares individually with B and C is greater than the mutual information combined region BC shares with A. Thus, the subregions share correlations with other parties. This contrasts sharply with random, nonsymmetric states as shown in Eq. (2.9). Studies on non-integrable quantum spin systems with permutationally symmetric initial states have shown that such systems can produce states with positive

[3]Class of quantum systems described by the holographic principle, which posits that a higher-dimensional theory can be fully described by a lower-dimensional one [15, 106, 107].

I_3 [102, 108]. These findings suggest that scrambling does not directly align with conventional quantum chaos, which we will explore further in Sec. 2.5

2.5 Scrambling vs Chaos vs Thermalisation

In this section, we explore the intricate relationships between quantum information scrambling, quantum chaos, and thermalisation. While these concepts are often used interchangeably due to their interconnected nature, it is essential to distinguish them to fully understand their implications. Our discussion will remain focused on the core aspects relevant to this thesis, providing clear and concise explanations.

Chaos in classical mechanics refers to the sensitivity to slight perturbations in the phase-space trajectories. A classic example is the double-rod pendulum [109], which shows an exponential divergence in the dynamics for slightly different initial conditions. The notion of trajectories which is well established in classical systems does not work in quantum mechanical systems by virtue of the Heisenberg uncertainty principle forbidding simultaneous measurement of coordinates and velocity. This is why quantum chaos is a difficult concept to define and study in contrast to its classical counterpart. Studying the level statistics of the Hamiltonian is the usual approach. Level statistics of a Hamiltonian is the distribution of the eigenenergies of the Hamiltonian. The level spacing between adjacent energy levels is given by $\lambda_i = E_{i+1} \quad E_i$, when the energy levels are ordered as a monotonically increasing sequence $E_1 \quad E_2 \quad \ldots$. In a chaotic system, the level spacings tend to follow the Wigner-Dyson distribution [110], which is characteristic of random matrix theory (RMT) [111, 112]. This distribution shows level repulsion, meaning that small spacings are less likely. This typically occurs for non-integrable quantum systems [113] and for Hamiltonians obtained by quantizing classical chaotic systems [114]. In contrast, integrable systems have level statistics that typically follow a Poisson distribution. Having briefly introduced the concept of quantum chaos from the perspective of level spacing statistics and random matrix theory, we next discuss how this is related to the eigenstate thermalisation hypothesis (ETH).

This concept was initially inspired by early works of Berry [115, 116] and later formalized by Deutsch [117] and Srednicki [118–120].

To understand ETH, let us consider a generic, non-integrable Hamiltonian H. For a given pure state $|\psi\rangle = \sum_u C_u |u\rangle$, evolving under this Hamiltonian H, the expectation value of an observable $\hat{O}$ can be calculated at a given time t with respect to $|\psi(t)\rangle$ as

$$\langle \hat{O} \rangle_t = \langle \psi(t) | \hat{O} | \psi(t) \rangle \tag{2.12}$$

$$= \sum_{uv} C_v C_u e^{-i(E_u - E_v)t} O_{uv} \tag{2.13}$$

$$= \sum_u |C_u|^2 O_{uu} + \sum_{u \neq v} C_v C_u e^{-i(E_u - E_v)t} O_{uv}, \tag{2.14}$$

where $O_{uv} = \langle u | \hat{O} | v \rangle$ are the matrix elements. ETH states that for generic Hamiltonians, the diagonal elements of a local observable O correspond to the microcanonical average prescribed by statistical mechanics, i.e., O_{uu} averaged over a small energy window is a smooth function of energy. Specifically, the eigenstates of such Hamiltonians behave equal to the microcanonical or thermal density matrix. The off-diagonal elements oscillate over time $e^{-i(E_u - E_v)t}$, and these oscillations tend to average out to zero over long times. As a result, the long-time behaviour is dominated by the diagonal elements. RMT provides valuable insights into the statistical properties of these off-diagonal matrix elements [2, 119, 120]. Generally, Hamiltonians exhibit eigenstate thermalisation along with quantum chaos, often behaving like random matrices as discussed in [1], although certain exceptions exist [121]. The ETH as stated by Srednicki and Deutsch talk about the equilibration or relaxation of the local observables to the micro-canonical predictions. However, systems may equilibrate to other values [4], which means that thermalisation is a special case of equilibration [122–125]. While a comprehensive explanation of the eigenstate thermalisation hypothesis (ETH) is beyond the scope of this thesis, the main message is that thermalisation, quantum chaos, and

[4] For example, integrable systems equilibrate to a state that retains the memory of the initial state [122].

random matrix theory (RMT) are closely related and often go hand in hand. For a more detailed analysis of ETH, readers are referred to [2].

How are these related to quantum information scrambling? Even though we have introduced measures of scrambling like tripartite mutual information in Sec. 2.4, to understand the relationship between quantum chaos, ETH, and quantum information scrambling, we use the out-of-time order correlator (OTOC) [126–133]. It is a time-dependent function defined as the expectation value of double commutators

$$C_{WV} = \langle [\hat{W}(t), \hat{V}]^\dagger [\hat{W}(t), \hat{V}] \rangle. \tag{2.15}$$

Here $\hat{V}$ and $\hat{W}$ are operators and they evolve under the Hamiltonian H according to the Heisenberg picture $W(t) = e^{iHt} W e^{-iHt}$. Even though this definition holds for an arbitrary pair of operators, we aim to characterise physical observables and hence the operators are hermitian. This gives us

$$C_{WV} = \langle [\hat{W}(t), \hat{V}]^2 \rangle, \tag{2.16}$$

$$C_{WV} = 2(1 - \mathrm{Re}\{F_{W,V}(t)\}), \tag{2.17}$$

$$\text{where} \quad F_{W,V}(t) = \langle \hat{W}^\dagger(t) \hat{V}^\dagger \hat{W}(t) \hat{V} \rangle. \tag{2.18}$$

An OTOC describes information scrambling by measuring how quickly the initially commuting operators W and V ($C_{W,V}(t = 0) = 0$) fail to commute. The growth of the commutator as described by $C_{W,V}$, is constrained by Lieb-Robinson velocity given in Eq. (2.5) for 1-dimensional systems with short range interactions. The behaviour of OTOCs has been studied in various systems and exponential growth in OTOCs is interpreted as a signature of scrambling and chaos [127]. However, this definition of chaos does not align with the spectral one [134–138]. Many focused studies have been conducted to find the intricate differences between these two processes. One such quantum system that is integrable (does not have a Wigner Dyson distribution for its level statistics), but shows exponential growth in the OTOC calculations is the Floquet XXZ model [138]. This is an example where we see that scrambling is necessary, but is not

sufficient for chaos. Finally, fast scrambling is often associated with chaotic dynamics, but the converse is not necessarily true [102, 108, 139, 140]. A simple example is a randomly coupled nearest-neighbour model, which does not exhibit fast scrambling but has level statistics that demonstrate chaotic behaviour [139, 140]. Thus, while the spectral properties of a Hamiltonian may not predict fast scrambling, they serve as a useful initial check to assess whether a system may possess fast scrambling.

While both the dynamical indicators of chaos and the spectral definition of chaos are commonly studied, there is not yet agreement on what quantum chaos really is. This remains an open question in the field, with various Hamiltonians and models being explored to understand the connections between spectral and dynamical properties. In this thesis, we adopt the more traditional definition of chaos based on spectral properties. For studying scrambling, we use bipartite entanglement entropy and tripartite mutual information as key indicators. Building on the definition of fast scrambling provided in Sec. 1.2, we also define a system as fast scrambling if the time for extensive contiguous subregions to reach volume-law entanglement scales logarithmically with the system size. Using this criterion, the tripartite mutual information saturates to a given value corresponding to the system becoming volume-law entangled. For fast scramblers, the time it takes to reach this value scales logarithmically with the system size.

In summary, Sec. 2.5 discusses the distinctions and relationships between quantum information scrambling, quantum chaos, and thermalisation. Quantum chaos and the eigenstate thermalisation hypothesis (ETH) are connected through random matrix theory (RMT). While scrambling and chaos are linked by the behaviour of out-of-time-ordered correlators (OTOCs), they are not identical. Scrambling can occur without the typical signatures of quantum chaos, and chaotic Hamiltonians do not necessarily exhibit fast scrambling behaviour. Thus, although quantum chaos, ETH, and scrambling are related, they remain distinct phenomena with their own specific signatures and behaviours. While this section outlines key similarities and distinctions between

quantum chaos, ETH, and scrambling, the discussion is intentionally kept within the scope of this thesis.

2.6 Summary

In Ch. 2, we established the foundational framework essential for the analyses presented throughout this thesis and explored the key concepts related to quantum information scrambling. We started by introducing the concept of entanglement entropy and explored how its scaling with system size can reveal the underlying geometry in Sec. 2.2. This understanding is crucial for identifying the geometry in our sparse Clifford circuit models, which we explore further in Ch. 5. Next, we discussed the concept of lightcones to explore the relationship between entanglement spreading and the underlying geometry of the quantum system in Sec. 2.3. In Sec. 2.4, we introduced the tripartite mutual information and established that its negativity may be used as an indicator of quantum information scrambling. Finally, in Sec. 2.5, we tried to outline the connections between three commonly discussed concepts: quantum information scrambling, quantum chaos, and thermalisation. This chapter serves as a backbone for the calculations and analyses in both Ch. 5 and Ch. 6, providing the necessary theoretical groundwork for the discussions that follow. In the next chapter, we introduce the concepts surrounding quantum-enhanced metrology and study a prototypical model to create metrologically relevant states.

Chapter 3

Quantum Enhanced Metrology

> What we observe is not nature itself, but nature exposed to our method of questioning.
>
> Werner Heisenberg

3.1 Introduction

Metrology, the science of measurement, is fundamental to scientific inquiry and technological advancement. Its relevance in science and technology can be seen ubiquitously. For example, the scientific theory of gravitational waves proposed by Albert Einstein in 1916 was verified and tested experimentally by LIGO in 2016, thanks to the development of advanced optical measurement technique [141]. Metrology is also critical in the field of biology, where precise measurement techniques are essential for understanding complex biological processes. For instance, the use of Doppler ultrasound to measure blood flow velocity is a prime example [142]. Similarly, metrology also plays a crucial yet often overlooked role in engineering and architecture, where precision in measurement is essential for ensuring the reliability and safety of buildings, bridges, and all other kinds of infrastructure. Extracting useful information from the measurements is a central challenge in metrology. While certain fundamental quantities, such as length, and mass, can be directly measured with high precision using standardized

instruments, many physical parameters of interest cannot be directly measured. It is more accurate to say that such parameters are estimated. The process of constructing an estimate still relies on measuring a related (measurable) quantity. For example, the direct measurement of blood flow velocity within arteries and veins is not feasible because inserting a measuring device into blood vessels could cause damage or disrupt normal flow. Instead, the Doppler ultrasound measures the frequency shift of sound waves as they bounce off moving red blood cells. Frequency, which is directly measurable using instruments like oscilloscopes, is determined by observing the periodicity of a waveform and calculating its oscillations over a known time interval. In this way, it is intrinsically related to time—a fundamental quantity that can be measured with high precision. The frequency shift is then used to calculate the velocity of blood flow indirectly. Mathematically, estimation theory addresses this problem of estimating unknown parameters from measured empirical data. With the frequentist approach [143, 144], in principle, with a sufficient set of empirical data from the measured quantity, the physical parameter of interest may be estimated with a given degree of precision set by the mean-squared error.

Estimation theory was extended to quantum information by Holevo and Helstrom [10, 145]. Quantum metrology, a discipline born from these developments, has found applications in diverse areas, including but not limited to magnetometry [146–149], thermometry [150–152], and clock synchronization [153–156]. In this context, our primary focus is on the canonical problem of phase estimation, where the goal is to retrieve an unknown phase encoded in a given state using appropriate measurement strategies. By leveraging quantum phenomena such as entanglement [11, 12], quantum-enhanced metrology promises to surpass the classical limits of measurement accuracy. The process of phase estimation can be broadly divided into two main components: state generation and measurement, as illustrated in Fig. 3.1 by the blue and pink dotted boxes, respectively. State generation involves using the concept of entanglement discussed in Sec. 2.2 to produce resource states that are used as probes to encode and measure an unknown phase.

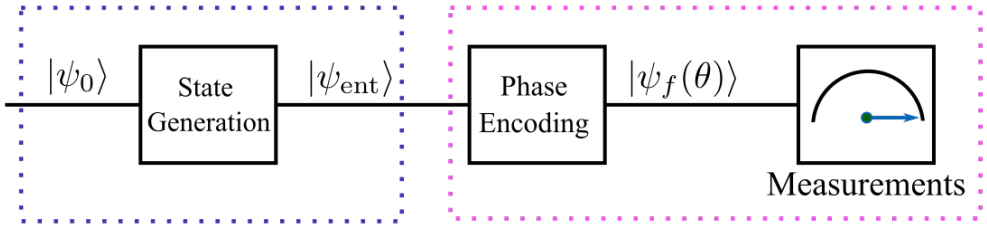

Figure 3.1: **A Schematic Diagram Showing the Usual Steps of Phase Estimation** An initial product state $j\psi_0 i$ undergoes dynamics to generate an entangled state $j\psi_{\text{ent}} i$. This highly sensitive state is used for encoding a phase via unitary evolution, which is extracted through measurements. The blue dotted box shows the state generation part and the pink shows the measurement part.

A key strategy for this is *spin squeezing* which will be introduced in Sec. 3.4 and the prototypical model used is the one-axis twisting model with all-to-all connectivity [8, 13, 14, 157]. This model has been implemented in experiments using atoms in optical cavities [60–62, 82], and trapped ions [158, 159]. Beyond all-to-all interactions, other approaches have been explored to generate metrologically useful states, including short-range interacting models using Rydberg atoms [160–162], and low-depth variational circuit models designed for neutral atom platforms and trapped ions [163–165]. Another experimental platform that has been investigated is dipolar interacting spin systems, where highly entangled states are generated through uniform single-qubit rotations and free evolution under dipolar interactions [166].

In this chapter, we introduce the key concepts related to generating states with metrological relevance. The following sections are organised as follows: In Sec. 3.2, we begin by introducing the Cramér-Rao bound and quantum Fisher information, which forms the theoretical foundation of parameter estimation in quantum metrology. We then introduce collective spin operators in Sec. 3.3, which are crucial for understanding the collective spin nature of quantum systems. Following this, in Sec. 3.4, we discuss spin-squeezing, a practical technique for enhancing measurement precision in quantum systems, within which we introduce the one-axis twisting Hamiltonian (see Sec. 3.4.1),

explore its dynamics, and examine how this system generates states of interest for metrology. This foundation is important for our analysis in Ch. 7, where we utilize sparse coupling graphs where the number of couplings per site scales logarithmically with system size N, i.e., $\log_2 N$ to generate metrologically useful states. These results are then compared with those produced by the one-axis twisting Hamiltonian.

3.2 Cramér-Rao Bound and Fisher Information

3.2.1 Classical Description

The question of efficient extraction of information from a set of data is native to statistics. The basic idea is to estimate the value of the unknown *latent parameters* [144] using the measured or provided data of *observables*. Formulating this mathematically, let X be a random variable that has N different discrete values $x = \{x_1, ..x_N\}$. Let $P(x_i|\theta)$ be the conditional probability of the measurement data x_i given the latent parameter θ. The probability distribution function $P(X|\theta)$ dictates the distribution of the observed data. After measuring a suitable variable, in this case X, the latent parameter θ is estimated using an estimator function which we call as $\theta_{\text{est}}(x)$ whose input is the collected data x. Ideally, the expectation value of the estimator function should be equal to the true value of the parameter as shown

$$\langle\theta_{\text{est}}\rangle = \int P(x|\theta)\theta_{\text{est}}(x)dx = \theta. \tag{3.1}$$

While the assumption given in Eq. (3.1) may not always hold, we consider this for the purpose of deriving a bound on the sensitivity of parameter estimation [167]. Here, we consider the observed data to take on a continuum of values, which can be treated similarly to a sum in the discrete case. The mean and variance of the estimator function are well-defined as it is a function associated with a random variable. The mean squared error (MSE) is defined as

$$(\quad\theta)^2 = \langle(\theta_{\text{est}}(x) \quad \theta)^2\rangle = \int P(x|\theta)(\theta_{\text{est}}(x) \quad \theta)^2 dx, \tag{3.2}$$

and since Eq. (3.1) holds, MSE is equal to the variance of the latent parameter θ. The Cramér-Rao bound [168] assigns the lowest possible value to the MSE. This can be deduced by writing Eq. (3.1) as

$$\int P(x|\theta)(\theta_{\text{est}} - \theta)dx = 0. \tag{3.3}$$

Thus,

$$\begin{aligned} 0 &= \frac{\partial}{\partial\theta}\int P(x|\theta)(\theta_{\text{est}} - \theta)dx, \\ &= \int P(x|\theta)\frac{\partial \log P(x|\theta)}{\partial\theta}(\theta_{\text{est}} - \theta)dx - 1. \end{aligned} \tag{3.4}$$

To calculate the bound, we use the Cauchy–Schwarz inequality

$$\left|\int f(x)g(x)dx\right|^2 \leq \left(\int f(x)^2dx\right)\left(\int g(x)^2dx\right), \tag{3.5}$$

with $f(x) \to \sqrt{P(x|\theta)}\frac{\partial \log P(x|\theta)}{\partial\theta}$ and $g(x) \to \sqrt{P(x|\theta)}(\theta_{\text{est}} - \theta)$. Applying this in Eq. (3.4), gives

$$1 \leq \left(\int P(x|\theta)\left(\frac{\partial \log P(x|\theta)}{\partial\theta}\right)^2 dx\right)\left(\int P(x|\theta)(\theta_{\text{est}} - \theta)^2 dx\right). \tag{3.6}$$

Rearranging the terms gives us the Cramér-Rao bound

$$(\Delta\theta)^2 \geq \frac{1}{F(P(x|\theta))}, \tag{3.7}$$

$$\text{where} \quad F(P(x|\theta)) = \int P(x|\theta)\left(\frac{\partial \log P(x|\theta)}{\partial\theta}\right)^2 dx = \int \frac{1}{P(x|\theta)}\left(\frac{\partial P(x|\theta)}{\partial\theta}\right)^2 dx \tag{3.8}$$

is the Fisher Information [169]. This quantity is interpreted as how much information can be extracted about an unknown parameter θ from the probability distribution. The Cramér-Rao bound can be equivalently represented as

$$(\Delta\theta)^2 \geq \frac{1}{NF(P(x|\theta))}, \tag{3.9}$$

because F is a non-negative quantity and x is N independent realizations of the random variable X. From here, using the central limit theorem, as $N \to \infty$, the sample average will take a normal distribution with a variance of $O(N^{-1})$.

3.2.2 Quantum Description

In the quantum realm, the basics of parameter estimation remain unchanged [10, 145]. The main difference is that the measurement outcomes (x in Sec. 3.2.1) may no longer be independent due to the presence of entanglement in the system. In quantum formalism, we must account for all possible measurements in order to make the Fisher information independent of specific measurement strategies. Thus, by maximising the classical Fisher Information F over all Positive Operator-Valued Measures (POVMs) [7, 170], which are sets of positive semi-definite (Hermitian) operators $\{M\}$, such that $\sum_n \hat{M}(x_n) = \mathbb{I}$, we obtain the quantum Fisher information (QFI) F_Q. In essence, the QFI provides a bound on how well we can estimate a parameter θ from a quantum state $\rho(\theta)$, which is created from an initial state $|\psi_0\rangle$ by a unitary evolution $\hat{U}(\theta) = \exp\{-i\hat{H}\theta\}$. If ν is the number of times the quantum measurement is done to estimate θ on the state $\rho(\theta)$, then $(\Delta\theta)^2 \geq \frac{1}{\nu F_Q(\theta)}$. The probability of getting a particular measurement outcome x_n on the state $\rho(\theta) = |\psi(\theta)\rangle\langle\psi(\theta)|$ given the parameter θ is

$$P(x_n|\theta) = \langle\psi(\theta)|\hat{M}(x_n)|\psi(\theta)\rangle = \mathrm{Tr}[\rho(\theta)\hat{M}(x_n)]. \tag{3.10}$$

Going back to the Eq. (3.8), we need to calculate

$$\begin{aligned}\frac{\partial P(x_n|\theta)}{\partial\theta} &= \left[\frac{d}{d\theta}\langle\psi(\theta)|\right]\hat{M}(x_n)|\psi(\theta)\rangle + \langle\psi(\theta)|\hat{M}(x_n)\left[\frac{d}{d\theta}|\psi(\theta)\rangle\right] \\ &= -2\mathrm{Im}\{\langle\psi(\theta)|\hat{H}\hat{M}(x_n)|\psi(\theta)\rangle\}.\end{aligned} \tag{3.11}$$

Following reference [171], one may introduce an arbitrary real function $G(\theta)$. Since it is a real value function, it does not affect Eq. (3.11) and we obtain

$$\frac{\partial P(x_n|\theta)}{\partial\theta} = 2\mathrm{Im}\{\langle\psi(\theta)|[\hat{H} - G(\theta)]\hat{M}(x_n)|\psi(\theta)\rangle\}. \tag{3.12}$$

Calculating $\left(\frac{\partial P(x_n|\theta)}{\partial\theta}\right)^2$ for continuous values, one may obtain

$$\begin{aligned} F(P(x|\theta)) &= \int \frac{1}{P(x|\theta)}\left(\frac{\partial P(x|\theta)}{\partial\theta}\right)^2 dx, \\ &= 4\langle\psi(\theta)|[\hat{H} - G(\theta)]^2|\psi(\theta)\rangle. \end{aligned} \tag{3.13}$$

If we choose $G(\theta) = \langle\psi_0|\hat{H}|\psi_0\rangle$, and by applying the Baker-Campbell-Hausdorff (BCH) formula, we rewrite the expectation value $\langle\hat{H}\rangle = \langle\psi_0|\hat{H}|\psi_0\rangle = \langle\psi(\theta)|\hat{H}|\psi(\theta)\rangle$, then Eq. (3.13) may be expressed as

$$\begin{aligned} F &= 4\langle\psi(\theta)|\left(\hat{H} - \langle\hat{H}\rangle\right)^2|\psi(\theta)\rangle, \\ &= 4\left(\langle\psi(\theta)|\hat{H}^2|\psi(\theta)\rangle + \langle H\rangle^2\langle\psi(\theta)|\psi(\theta)\rangle - 2\langle H\rangle^2\right), \\ F &= F_Q = 4\left(\Delta\hat{H}\right)^2, \end{aligned} \tag{3.14}$$

where $\left(\Delta\hat{H}\right)^2 = \langle\hat{H}^2\rangle - \langle H\rangle^2$ is the variance. This is the QFI for a pure state [170]. This is a powerful tool for describing the sensitivity of a state to a given parameter θ and is independent of the procedure of measurement.

The QFI of any separable state of N qubits is bounded by $F_Q \leq N$ [14]. As a result, the maximum sensitivity achievable for a separable state corresponds to the classical limit or *standard quantum limit* (SQL), given by $(\Delta\theta)^2 = O(N^{-1})$. However, the presence of entanglement can surpass this limit. When entanglement is introduced, the classical limit $(\Delta\theta)^2 = O(N^{-1})$ is no longer the upper bound, and the sensitivity improves, leading to $(\Delta\theta)^2 > O(N^{-1})$, which implies $F_Q > N$. This bound has been mathematically discussed in [14, 172]. The maximum value of the attainable quantum

Fisher information is called the *Heisenberg limit* with $F_Q = N^2$. It's important to note that not all entangled states are advantageous for metrology. Among those that are, their effectiveness in quantum-enhanced metrology can vary. One prominent quantum strategy for creating metrologically relevant states, first introduced by Kitagawa and Ueda [8], is spin squeezing. Before introducing the concept of spin squeezing in Sec. 3.4, we will first review the foundational concepts related to the collective nature of spin systems in Sec. 3.3.

3.3 Collective Spin Operators and Phase Space Visualisation

3.3.1 Collective Spin System

Since we are interested in studying the scaling of the QFI with the number of particles N, an ensemble of N distinguishable qubits is introduced and described with a collective spin vector $\hat{J} = (\hat{J}_x, \hat{J}_y, \hat{J}_z)$, where

$$\hat{J}_x = \frac{1}{2}\sum_{l=1}^{N} \hat{\sigma}_l^x, \qquad \hat{J}_y = \frac{1}{2}\sum_{l=1}^{N} \hat{\sigma}_l^y, \qquad \hat{J}_z = \frac{1}{2}\sum_{l=1}^{N} \hat{\sigma}_l^z, \tag{3.15}$$

and $\hat{\sigma}_l = (\hat{\sigma}^x, \hat{\sigma}^y, \hat{\sigma}^z)$ is the Pauli vector of the l^{th} particle and $\hbar = 1$. The operators given in Eq. (3.15) satisfy the angular-momentum commutation relations

$$[\hat{J}_x, \hat{J}_y] = i\hat{J}_z, \qquad [\hat{J}_z, \hat{J}_x] = i\hat{J}_y \qquad [\hat{J}_y, \hat{J}_z] = i\hat{J}_x, \tag{3.16}$$

and the associated uncertainty principle is $\langle J_\mu^2\rangle\langle J_\nu^2\rangle \geq \frac{1}{4}|\langle J_\tau\rangle|^2$, where μ, ν, τ denote the components of any three orthogonal directions. The dimension of the Hilbert space for an N spin-1/2 system grows exponentially as 2^N when symmetry is not considered. However, by imposing exchange symmetry among the spins, this dimension is significantly reduced to $(N + 1)$. A common choice of basis in this reduced Hilbert space is the Dicke states [52, 173–176]. The Dicke basis provides an orthonormal set of states for the collective spin system and is crucial in various quantum information

processing tasks, including quantum metrology. We will introduce the Dicke basis in the following section, Sec. 3.3.2.

3.3.2 Dicke States

The N-spin Dicke state $|J, M\rangle$ with $M = J, J-1, \ldots, -J$ is a uniform, permutation-symmetric, superposition of N-bit strings $|x\rangle$, such that there are $J + M$ bits in 0 where $J = N/2$. The normalisation of such a state is $\binom{2J}{J+M}^{-1/2}$. For example, for $N = 4$, the state $|J = \frac{4}{2}, M = 0\rangle = \frac{1}{\sqrt{6}}(|0011\rangle + |0101\rangle + |0110\rangle + |1001\rangle + |1010\rangle + |1100\rangle)$. It is a simultaneous eigenstate of $\hat{J}_z$ and $\hat{J}^2$:

$$\hat{J}_z|J, M\rangle = M|J, M\rangle, \tag{3.17}$$

$$\hat{J}^2|J, M\rangle = J(J+1)|J, M\rangle. \tag{3.18}$$

This generates $(N + 1)$ mutually orthogonal states. In the next section, we introduce coherent spin states, which offer a complementary perspective by highlighting the more classical behaviour of quantum spins.

3.3.3 Coherent Spin States

Coherent spin states (CSS) are pure, separable states of a symmetric ensemble of N spins with $J = N/2$. This state can be created by an arbitrary rotation of $|J, \quad J\rangle$ or $|J, J\rangle$. Starting from $|J, \quad J\rangle$, the spin coherent state in the Dicke basis can be written as [177–179]

$$|\theta, \varphi\rangle = \hat{R}_{\theta\varphi}|J, \quad J\rangle, \tag{3.19}$$

where φ is the angle in which the Cartesian axes (x, y, z) are rotated around the z axis to create new axis $\vec{k}$, $\vec{n}$ and θ is the angle in which the axis $\vec{n}$ is rotated [180]. The

transformed collective spin operators are given by

$$\hat{J}_z = \hat{J}_z, \tag{3.20}$$

$$\hat{J}_n = \hat{J}_x \sin\varphi \quad \hat{J}_y \cos\varphi, \tag{3.21}$$

$$\hat{J}_k = \hat{J}_x \cos\varphi + \hat{J}_y \sin\varphi, \tag{3.22}$$

and the rotation operation is

$$\hat{R}_{\theta\varphi} = e^{\ i\theta\hat{J}_n}, \tag{3.23}$$

$$= e^{\ i\theta(\hat{J}_x \sin\varphi \quad \hat{J}_y \cos\varphi)}, \tag{3.24}$$

$$= \exp\left\{\zeta\hat{J}_+ \quad \zeta^* \hat{J}^-\right\}, \tag{3.25}$$

where $\zeta = \frac{\theta}{2} e^{\ i\varphi}$, $\hat{J}_x = \frac{1}{2}(\hat{J}_+ + \hat{J}^-)$, and $\hat{J}_y = \frac{1}{2i}(\hat{J}_+ \quad \hat{J}^-)$. Eq. (3.19), thereby can be written as

$$|\theta,\varphi\rangle = \hat{R}_{\theta\varphi}|J, \quad J\rangle, \tag{3.26}$$

$$= \sum_{M=\ J}^{M=J} \sqrt{\binom{2J}{J+M}} \left(\cos\frac{\theta}{2}\right)^{J \quad M} \left(\sin\frac{\theta}{2}\right)^{J+M} e^{\ i\varphi(J+M)} |J, M\rangle, \tag{3.27}$$

showing that a general CSS can be described as a superposition of Dicke states. This state can be visualised on a generalised Bloch sphere, as shown in Fig. 3.2(a), using the Husimi Q distribution, which we introduce in the following section.

3.3.4 Visualisation of Quantum States

Phase space representation provides a powerful framework to describe quantum states and their dynamics. The two widely used approaches for visualisation are the Husimi Q function and the Wigner function [181–184]. In this chapter, we will focus on using the Husimi Q function [184]. In general, the Husimi Q function on a Bloch sphere for a quantum state $\rho = |\psi\rangle\langle\psi|$ is defined as the expectation value of the density matrix in the coherent state $|\theta,\varphi\rangle$, where θ,φ are azimuthal and polar angles, respectively.

Mathematically, it is expressed as:

$$Q(\theta,\varphi) = \frac{1}{\pi}\langle\theta,\varphi|\rho|\theta,\varphi\rangle\,. \tag{3.28}$$

The interpretation of this representation on a generalised Bloch sphere differs from that of a single spin-1/2 on the Bloch sphere. A single spin-1/2 has a Hilbert space dimension of two, and representation of this single spin on a two dimensional Bloch sphere hence will be exact. However, for the collective spin system, the dimension is $2J+1$, making such an exact mapping impossible. Consequently, the representation of a spin N system on the generalised Bloch sphere gives the mean spin direction and its fluctuations adhering to the Heisenberg uncertainty principle as shown below Eq. (3.16). The Husimi Q function is non-negative. An example of the Husimi Q function for a CSS and spin squeezed state which will be introduced in Sec. 3.4 is shown in Fig. 3.2(a) and Fig. 3.2(b) respectiviely.

Having established the foundational concepts of collective spin operators, coherent spin states, and the phase space representation on the generalised Bloch sphere, we now discuss the topic of spin squeezing. In Sec. 3.4, we will examine spin squeezing in detail and introduce the one-axis twisting Hamiltonian—a prototypical model that effectively generates spin-squeezed states with metrological relevance.

3.4 Spin Squeezing

Spin squeezing is a quantum phenomenon in which the uncertainties (variances) in two conjugate spin components (directions) are redistributed in such a way that one component's uncertainty is reduced (squeezed) at the expense of increasing the uncertainty in the other component (anti-squeezed) [8, 9, 157, 185]. The squeezing parameter is a crucial concept used to characterize the phenomenon of squeezing and hence multiple definitions have been employed [8, 9]. The idea put forth by Kitagawa and Ueda [8] is to compare the uncertainty with respect to the non-squeezed state, that is the coherent

spin state, and is given as

$$\xi_S^2 = \frac{N\min(\quad \hat{J}_?)^2}{|\langle \hat{J}_{\mathrm{CSS}} \rangle|^2} = \frac{4\min(\quad \hat{J}_?)^2}{N}, \tag{3.29}$$

where $?$ denotes the perpendicular direction to the mean-spin direction $\mathbf{s}$ and $(\quad \hat{J}_?)^2$ is the variance. Here, the minimum value is calculated by taking the smallest eigenvalue of the covariance matrix $C_{\mu\nu} = \frac{1}{2}\langle \{\hat{J}_\mu, \hat{J}_\nu\} \rangle \quad \langle \hat{J}_\mu \rangle \langle \hat{J}_\nu \rangle$, where μ and ν are two mutually perpendicular directions in the plane perpendicular to the mean-spin direction $\mathbf{s}$ and $\{\ \}$ is the anticommutator. A stronger condition was introduced later by Wineland [9], and is given by

$$\xi_R^2 = \frac{N(\quad \hat{J}_?)^2}{|\langle \hat{J}_{\mathbf{s}} \rangle|^2}. \tag{3.30}$$

If $\xi_R^2 < 1$, the state is said to be spin squeezed along the $?$ axis. Since $|\langle \hat{J}_{\mathbf{s}} \rangle| \quad N/2$, we obtain $\xi_S^2 \quad \xi_R^2$. Interestingly, one application of spin squeezing is to detect quantum entanglement [186–191]. The Kitagawa and Ueda spin squeezing parameter ξ_S^2 has been studied in relationship with pairwise entanglement [192] and [193] proved that a many body spin-$1/2$ state is entangled if it is spin squeezed with $\xi_R^2 < 1$.

Alongside the calculation of the spin squeezing parameter, to gauge metrological relevance, the QFI can also be calculated for the spin system, as it describes the sensitivity of a given state $|\psi\rangle$ to a parameter θ as mentioned in Sec. 3.2.2. For spin systems, the standard scenario corresponds to θ being a phase encoded by a small rotation of the probe state around a given axis, $\hat{J}_\mu$, the generator of a rotation around axis μ. In such a case, it is possible to maximize the QFI by optimising over all the rotation directions [194]. For pure states, this optimum is given by the maximum eigenvalue of the covariance matrix $C_{\mu\nu} = \frac{1}{2}\langle \{\hat{J}_\mu, \hat{J}_\nu\} \rangle \quad \langle \hat{J}_\mu \rangle \langle \hat{J}_\nu \rangle$, where μ and ν are two mutually perpendicular directions and can take values $\mu, \nu = x, y, z$. This gives us

$$F_Q[\theta, J_\mu] = 4(\quad \hat{J}_\mu)^2 \ . \tag{3.31}$$

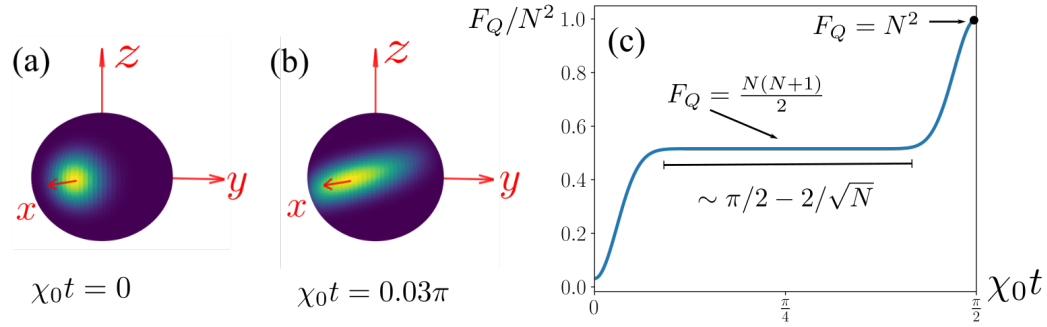

Figure 3.2: **One Axis Twisting Dynamics** (a). A Coherent Spin State of $N = 32$ spins initialised in the x-polarized state with the mean spin direction along the x-axis. The effect of the one-axis twisting Hamiltonian in Eq. (3.32) is to shear this distribution. (b) A spin squeezed state at $\chi_0 t = 0.03\pi$. (c). The normalised quantum Fisher information as a function of $\chi_0 t$ for the OAT model for $N = 32$. This shows an initial steady rise in QFI which is also the spin-squeezed region, followed by a plateau where the QFI scales as N^2, and a rise to reach the GHZ state with $F_Q = N^2$.

3.4.1 One Axis Twisting Hamiltonian (OAT)

The most studied model on spin-squeezed states and the generation of metrologically useful states is the One Axis Twisting (OAT) model [8, 13, 14, 157]. The OAT Hamiltonian along the z axis is given by:

$$H_{OAT} = \chi_0 \sum_{i,j=1}^{N} S_i^z S_j^z = \chi_0 J_z^2, \tag{3.32}$$

where χ_0 is the OAT squeezing strength, N is the number of spins in the system, and the spin z operator $S_i^z = \sigma_i^z/2$ in terms of Pauli-Z operator on spin i. The OAT Hamiltonian creates states in the Dicke manifold introduced in Sec. 3.3.2. An initial state of N spins in the x-polarized state is depicted on the Bloch sphere as shown in Fig. 3.2(a). This is the CSS introduced in Sec. 3.3.3, where all the qubits are pointing along the same mean-spin direction $\mathbf{s}$, x in this case. The states are visualised using the Husimi Q representation introduced in Sec. 3.3.4. The OAT Hamiltonian in Eq. (3.32) shears this distribution, resulting in a squeezed state with reduced variance along the z-axis Fig. 3.2(b). This reduced variance hence allows for an enhanced measurement sensitivity to rotations of the collective spin state along the anti-squeezed axis (y-axis

in this case).

In the case of the OAT Hamiltonian in Eq. (3.32), for $\chi_0 t \ll 1/\sqrt{N}$, the state is spin squeezed, i.e. $\xi_R^2 < 1$. However, once $\chi_0 t \gg 1/\sqrt{N}$, the state wraps around the Bloch sphere, and spin squeezing is lost $\xi_R^2 > 1$. But the state is still entangled and the quantum Fisher information follows $F_Q[|\psi_{\mathrm{OAT}}(t)\rangle] > N$, where $|\psi_{\mathrm{OAT}}(t)\rangle$ is the state after allowing the Hamiltonian to evolve up to t. Using the expression of variances calculated with respect to axis x and y given in [8, 14], we can calculate the QFI of this state $F_Q[|\psi_{\mathrm{OAT}}(t)\rangle] = N(N+1)/2$ for $2/\sqrt{N} \lesssim \chi_0 t \lesssim \pi/2 \quad 2/\sqrt{N}$ [13, 14]. At $\chi_0 t = \pi/2$, the Greenberger-Horne-Zeilinger (GHZ) state is formed with a maximum QFI: $F_Q = N^2$, and we have a complete revival of initial dynamics at $\chi_0 t = \pi$. All this is illustrated in Fig. 3.2(c), where we observe how the QFI changes as a function of evolution time $\chi_0 t$. The OAT model features infinite range interactions and a dense all-to-all connectivity. While these can be engineered via indirect interactions (e.g, photon-mediated interactions between atoms in an optical cavity [60–62, 82, 159]), this degree of connectivity is challenging to realize with direct interactions in most physical setups. In Ch. 7, we show that this all-to-all dynamics can be emulated by sparsely coupled graphs.

3.5 Summary

In Ch. 3, we discussed various concepts related to quantum-enhanced metrology. In Sec. 3.2, we explored estimation theory, discussed the bounds on precision limits in both classical and quantum contexts, and introduced key concepts such as the quantum Fisher information and the Cramér-Rao bound. We established the standard quantum limit (SQL) and the Heisenberg limit for parameter estimation.

Following this, in Sec. 3.3, we laid out the mathematical foundations necessary for understanding quantum spin systems within the framework of quantum metrology. These included collective dynamics, coherent spin states, the Dicke basis, and the Husimi

representation. With these foundations in place, we introduced spin squeezing as an effective strategy for creating metrologically relevant states. Additionally, we examined the prototypical one-axis twisting Hamiltonian, a powerful tool for generating spin-squeezed states, as discussed in Sec. 3.4.

This chapter sets the stage for our analysis in Ch. 7, where we leverage sparse coupling graphs to create metrologically relevant states, comparing these results to those obtained using the one-axis twisting Hamiltonian. In Ch. 4, we introduce the concepts and methods necessary for efficiently simulating many-body systems, both in discrete and continuous time models.

Chapter 4

Numerical Methods

> The purpose of computing is insight, not numbers
>
> Richard Hamming

In this chapter, we introduce the numerical methods employed to solve the dynamics of quantum systems in both discrete and continuous time evolution. In Sec. 4.1, we begin by presenting a formalism for the efficient representation of a quantum state and its time evolution in a circuit model fashion. This formalism, known as the stabilizer formalism, not only simplifies the description of quantum states and operations but also demonstrates efficiency in implementing gate-based operations. Following this, in Sec. 4.2, we introduce the matrix product state (MPS) and matrix product operator (MPO) representations, which are powerful tools for describing quantum states and operators. In this section, we discuss how the MPS-MPO representation enables efficient time evolution of states through the time-dependent variational principle (TDVP). We also introduce methods for calculating entanglement entropy and tripartite mutual information, as detailed in Sec. 4.2.4. Together, these techniques provide a comprehensive tool-set for exploring quantum dynamics, allowing for precise and scalable simulations of complex systems.

4.1 Discrete Time Models

For our calculations pertaining to digital circuit models, we utilize the stabilizer formalism, a powerful mathematical tool that simplifies the description of quantum states and operations. In the sections that follow, we introduce this formalism and proceed to calculate entanglement entropy within this framework, as this quantity will be central to our analyses in Ch. 5 and Ch. 6.

4.1.1 Stabilizer Formalism

In classical systems, an N bit state is fully specified by one of the 2^N possible configurations, with each bit deterministically taking a value of 0 or 1. In contrast, an N-qubit state in quantum mechanics, exists in a superposition of all the 2^N configurations, each with its own probability amplitude. This exponential growth of the number of parameters complicates the efficient simulation of many-body dynamics of quantum systems in classical computers. This is one of the major reasons for the development of classical algorithms to handle the exponentially growing number of variables. The *stabilizer formalism* is one such tool that helps in representing certain quantum many-body states (stabilizer states) and operations on them [23, 195, 196].

Let us begin this section by introducing the Pauli group $P(N)$, which consists of the tensor product of Pauli matrices

$$X = \begin{pmatrix} 0 & 1 \\ 1 & 0 \end{pmatrix}, \qquad Y = \begin{pmatrix} 0 & i \\ i & 0 \end{pmatrix},$$

$$Z = \begin{pmatrix} 1 & 0 \\ 0 & 1 \end{pmatrix}, \qquad \text{and} \quad I = \begin{pmatrix} 1 & 0 \\ 0 & 1 \end{pmatrix}.$$

Elements of the Pauli group act on a system of N qubits[1], with each element of $P(N)$ being a tensor product of N Pauli matrices, combined with a multiplicative factor of

[1] We use X, Y, Z here instead of $\sigma_x, \sigma_y, \sigma_z$

1 or i. The Pauli matrices satisfy the identities:

$$X^2 = Y^2 = Z^2 = I, \tag{4.1}$$

$$XY = iZ,\ YZ = iX,\ ZX = iY. \tag{4.2}$$

Thus, the Pauli group $P(N)$ has $|P(N)| = 4^{N+1}$ total number of operators. Consider two Pauli operators $P = i^k p_1..p_N$ and $Q = i^l q_1..q_N$, where p_j, q_j are Pauli matrices acting on qubit j, and k, l control the multiplicative factor. P commutes with Q if and only if the number of indices $j \in \{1,..N\}$ such that p_j anticommutes q_j are even; otherwise P anticommutes with Q.

A stabilizer group Stab($|\psi\rangle$) of a wavefunction $|\psi\rangle$ on a D-dimensional Hilbert space consists of all unitary operators that leave the state $|\psi\rangle$ unchanged. In other words, $U|\psi\rangle = |\psi\rangle$. For example, let us consider a single qubit state $|\psi\rangle = \frac{1}{\sqrt{2}}(|0\rangle + |1\rangle)$. This state is stabilized by Pauli operator X, i.e., $X|\psi\rangle = |\psi\rangle$. The identity operator I stabilizes all states and $-I$ stabilizes no state. The reason we call Stab($|\psi\rangle$) a group is that if we have $U, V \in$ Stab($|\psi\rangle$), then UV, U^{-1} and V^{-1} also belong to Stab($|\psi\rangle$). Here, we are specifically interested in an abelian subgroup S satisfying $S(|\psi\rangle) =$ Stab($|\psi\rangle$) $\cap\, P(N)$, or the group of Pauli operators that stabilize $|\psi\rangle$. Also, the state $|\psi\rangle$ is stabilized by exactly 2^N Pauli operators [196]. Using the principles of group theory which state that any finite group G has a generating set of size at most $\log_2|G|$, one can construct a generator set of linearly independent, mutually-commuting N Pauli strings for S, such that $N = \log_2|S|$. Given a stabilizer group S one can construct a *stabilizer state*

$$\rho_N(S) = 2^{-N} \sum_{g \in S} g\ , \tag{4.3}$$

which is the unique density matrix *stabilized* by S: $g\rho_N(S)g = +\rho_N(S)$ for all elements $g \in S$.

4.1.2 Clifford Circuits

A Clifford group C_N on N qubits is the group of all unitary operators $C \in C_N$ that maps elements of the Pauli group to other elements of the Pauli group i.e. $CP(N)C^\dagger = P(N)$. Therefore elements of the Clifford group also map every stabilizer state $\rho_N(S)$ onto another stabilizer state $\rho_N(S')$ with stabilizer group S'. The Clifford group is generated by three special gates, controlled-NOT (CNOT), Hadamard (H), and Phase gates (P)

$$H = \frac{1}{\sqrt{2}}\begin{pmatrix} 1 & 1 \\ 1 & -1 \end{pmatrix}, \qquad P = \begin{pmatrix} 1 & 0 \\ 0 & i \end{pmatrix},$$

$$\text{and} \quad \text{CNOT} = \begin{pmatrix} 1 & 0 & 0 & 0 \\ 0 & 1 & 0 & 0 \\ 0 & 0 & 0 & 1 \\ 0 & 0 & 1 & 0 \end{pmatrix}.$$

The time evolution using unitaries from the Clifford group can be computed classically in polynomial time, as shown by the Gottesman-Knill theorem [23, 195]. This is done by mapping the dynamics onto linear algebra operations over the Galois field (GF(2), i.e., binary numbers mod 2). The GF(2) contains just two elements, 0 and 1, with arithmetic operations performed modulo 2. The unitary operations of the Clifford group can be represented as matrices over GF(2), reducing their dynamics to efficient linear algebra problems in this field. This reduction allows classical algorithms to simulate these quantum operations in polynomial time. This is accomplished by considering the generators g of the stabiliser group, that are Pauli strings, as $g = \prod_i X_i^{x_i} Z_i^{z_i}$, where $i = 0, 1, ..N - 1$ are the qubit labels and $x_i, z_i = 0, 1$ specify whether a particular Pauli operator X_i, Z_i is present in the string. If $x_i = z_i = 0$, then the i^{th} Pauli operator is I. If $x_i = z_i = 1$, then it is the Y_i operator. Further, the stabilizer state is mapped onto a binary $N \times 2N$ matrix M, where each row $\ell = 1, \ldots, N$ of the matrix is a binary string $\vec{b}_\ell = (x_1, \ldots, x_N, z_1, \ldots, z_N)$ corresponding to the generator $g_\ell = \prod_i X_i^{x_i} Z_i^{z_i}$. The time evolution of the states represented using these matrices under the Clifford group involves performing row and column linear algebra operations [196, 197]. The

Hadamard gate H_i on-site i exchanges the operators $Z_i \$ X_i$ which corresponds to swapping columns i and $i + N$ in the matrix M. The Phase gate P_i on-site i exchanges the operators $X_i \$ Y_i$; in the matrix M this is equivalent to setting column $i + N$ equal to the sum (mod 2) of columns i and $i + N$. Finally, a controlled-NOT gate CNOT_{ij} applied between a control qubit i and a target qubit j is equivalent to transforming Pauli strings according to the following four rules:

$$X_i I_j \; ! \; X_i X_j, \tag{4.4}$$

$$I_i X_j \; ! \; I_i X_j, \tag{4.5}$$

$$Z_i I_j \; ! \; Z_i I_j, \tag{4.6}$$

$$\text{and} \quad I_i Z_j \; ! \; Z_i Z_j, \tag{4.7}$$

which correspond to setting column j equal to the sum of columns i and j (mod 2), and setting column $i + N$ equal to the sum of columns $i + N$ and $j + N$ (mod 2). With these H_i, P_i, and CNOT_{ij} gates in hand, we may systematically generate all N-qubit operators in C using standard algorithms [197].

4.1.3 Entanglement Entropy of Stabilizer States

Given a stabilizer state Eq. (4.3) and its associated stabilizer matrix M, one can readily compute the entanglement entropy of the system. The reduced density matrix of any state on a subsystem A is obtained by tracing out the rest of the system B i.e. $\rho_A = \mathrm{Tr}_B |\psi\rangle\langle\psi|$, and for a stabilizer state, it is given by,

$$\rho_A = \frac{1}{2^{|A|}} \sum_{g_A \in S_A} g_A, \tag{4.8}$$

where $S_A \quad S$ is the subgroup of stabilizers g_A. Tracing out the subregion B from a stabilizer matrix M is equivalent to simply discarding the columns corresponding to Pauli operators X_j, Z_j for $j \in B$. This is because Pauli matrices are traceless except for the identity matrix I. Further, a row reduction is applied to the remaining columns to identify a set of linearly independent set of generators g_A. First, let us calculate the

purity

$$\mathrm{Tr}\left[\rho_A^2\right] = 2^{-2jAj} \sum_{g,g' \in S_A} \mathrm{Tr}\left[gg'\right]. \tag{4.9}$$

If $g \neq g'$, then the $\mathrm{Tr}[gg'] = 0$, and if $g = g'$, then the multiplication of two Pauli matrices on the same site i gives identity matrix I, and hence $\mathrm{Tr}\left[g^2\right] = 2^{jAj}$. Hence,

$$\mathrm{Tr}\left[\rho_A^2\right] = 2^{-2jAj} 2^{jAj} |S_A| = 2^{-jAj} |S_A| . \tag{4.10}$$

Then the second-order Rényi entropy can be calculated by

$$\log \mathrm{Tr}\left[\rho_A^2\right] = -\log\left(2^{-jAj} |S_A|\right) = \log 2^{(jAj - \mathrm{rank}_{\mathrm{GF}(2)}(M_A))}, \tag{4.11}$$

where we have used the fact that $|S_A| = 2^{\mathrm{rank}_{\mathrm{GF}(2)}(M_A)}$ is the cardinality of the stabilizer group and $\mathrm{rank}_{\mathrm{GF}(2)}$ is the binary rank of the associated binary matrix of subsystem A, i.e., the number of linearly independent Pauli strings in the binary matrix M_A. The stabilizer states are said to have flat entanglement spectra, this means that all Rényi entropies are the same. In a nutshell, this is a direct consequence of the reduced density matrix being a stabilizer itself and can be written as Eq. (4.8). One can hence calculate

$$\rho_A^2 = 2^{-2jAj} \sum_{g,g' \in S_A} gg' = 2^{-2jAj} |S_A| \sum_{g \in S_A} g = \frac{|S_A|}{2^{jAj}} \rho_A. \tag{4.12}$$

Here, we are using the property of a group where the product of its elements generates other elements within the same group. One can see that $\rho_A^n = \left(\frac{|S_A|}{2^{jAj}}\right)^{n-1} \rho_A$. The nth-order Rényi entropy is given by [198]

$$S_A^n = \frac{1}{1-n} \log \mathrm{Tr}[\rho_A^n]. \tag{4.13}$$

This means that

$$S_A^n = \frac{1}{1-n} \log \mathrm{Tr}\left[\left(\frac{jS_Aj}{2^{jAj}}\right)^{n-1} \rho_A\right], \\ = \frac{1}{1-n} \log \left(\frac{jS_Aj}{2^{jAj}}\right)^{n-1} \mathrm{Tr}[\rho_A]\,. \tag{4.14}$$

We further use the expression ρ_A from Eq. (4.8), and the fact that only the identity matrix among the Pauli matrices has a non-zero trace, while all other Pauli matrices are traceless. This gives us

$$S_A^n = \frac{1}{1-n} \log \left(\frac{jS_Aj}{2^{jAj}}\right)^{n-1} \frac{1}{2^{jAj}} 2^{jAj}, \tag{4.15}$$

and thus

$$S_A^n = jAj \log 2 \quad \log(jS_Aj)\,, \tag{4.16}$$

which is equal to Eq. (4.11). Since the first order Rényi entropy is equal to the von Neumann entanglement entropy i.e. $\lim_{n \to 1} S_A^n = S_{vN}$, stabilizer states allow for straightforward calculation of the entanglement spectrum, which simplifies the study of entanglement properties. In this section, we have introduced the main technique that we employ to study our discrete-time models in Ch. 5 and Ch. 6. The Clifford group of gates do not constitute the universal set of quantum gates as some gates outside the Clifford group cannot be arbitrarily approximated with a finite set of operations. For example, the T gate

$$T = \begin{pmatrix} 1 & 0 \\ 0 & e^{i\frac{\pi}{4}} \end{pmatrix},$$

cannot be expressed as a finite sequence of gates from the Clifford group. However, the Clifford group remains an important tool in quantum information due to its classical simulability, which makes it invaluable for tasks such as quantum error correction and randomized benchmarking [7, 86, 199–201].

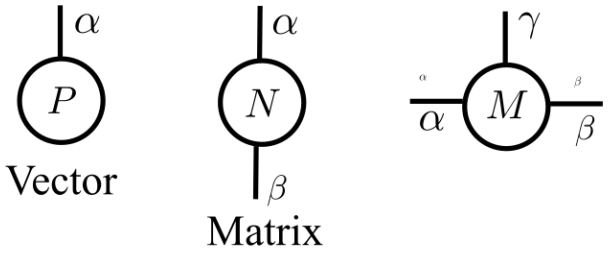

Figure 4.1: **Diagrammatic Representation of Tensors** Illustration of rank-1 (vector), rank-2 (matrix), and rank-3 tensors, where each leg represents an index of the corresponding tensor.

4.2 Matrix Product States and Matrix Product Operators

In the previous section, we introduced a numerical method that enables us to simulate quantum circuits with thousands of qubits effectively. Here, we continue our exploration of techniques that can efficiently manage the exponentially growing Hilbert space. In this section, we introduce a method to efficiently represent one-dimensional weakly-entangled states, known as Matrix Product States (MPS) [202–207]. We also introduce the concept of *time dependent variational principle* (TDVP) [208–212] which we have extensively used for our simulations in Ch. 7. Furthermore, we discuss the calculation of tripartite mutual information using MPS techniques.

4.2.1 Matrix Product States (MPS)

Tensors are multi-dimensional collections of numbers that can be either real or complex. For example, a rank 0 tensor is a scalar, a rank 1 tensor is a vector, and a rank 2 tensor is a matrix as illustrated in Fig. 4.1. Graphically, tensors can be represented as shapes (squares, circles, triangles), and each leg corresponds to an index of the tensor as illustrated in Fig. 4.1. A tensor network is a collection of tensors that contract together in a specific arrangement, of which matrix product states (MPS) are the simplest form.

Keeping this in mind, the coefficient tensor $c_{\sigma_1 \quad \sigma_N}$ of a general quantum state

$$|\psi\rangle = \sum_{\sigma_1, \quad ,\sigma_N} c_{\sigma_1 \quad \sigma_N} |\sigma_1 \quad \sigma_N\rangle \ , \tag{4.17}$$

as a product of N rank-3 tensors M_i [204–207]

$$|\psi\rangle = \sum_{\substack{\sigma_1, \quad ,\sigma_N, \\ m_0, \quad ,m_N}} M^{\sigma_1}_{1;m_0,m_1} \quad M^{\sigma_N}_{N;m_N \ 1,m_N} |\sigma_1 \quad \sigma_N\rangle \ . \tag{4.18}$$

Here, m_0 and m_N are 1-dimensional dummy indices introduced so that each tensor has the same form, and m_j is the local bond dimension connecting adjacent tensors and goes from 1 to the bond dimension D. For a given set of local states $\{|\sigma_1 \quad \sigma_N\rangle\}$, we use a single matrix $M^{\sigma_i}_i$ per site. Local physical states on-site i are given by σ_i. This is diagrammatically illustrated in Fig. 4.2(a). For a spin system, $\sigma_i \in \{|\uparrow\rangle, |\downarrow\rangle\}$, represents the local physical state. The bond dimension plays a critical role in how efficiently the quantum state can be represented. In the simplest case, when the bond dimension is 1, the MPS corresponds to a product state with no correlation between the sites. To represent some states, the bond dimension must grow exponentially with the system size, however, for states that obey area law scaling in entanglement entropy as introduced in Sec. 2.2.1, this can saturate (in 1D) [91, 205, 213]. In practice numerically we can truncate the bond dimension to a specified cutoff value. This cutoff value is set by the truncation error, which dynamically controls the bond dimension. This allows the bond dimension to grow or shrink such that the error introduced by truncating is below this set cutoff. This truncation is achieved by exploiting the singular value decomposition which will be introduced in Sec. 4.2.1.1, and this truncation effectively limits the entanglement of the system, making the method efficient for representing 1D equilibrium states, evolution close to equilibrium or short time evolution in quench dynamics with rapid entanglement growth.

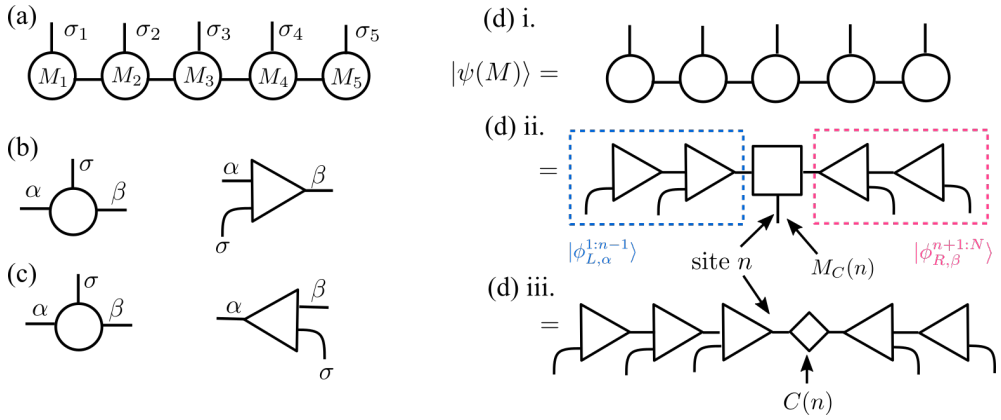

Figure 4.2: **Basic Concepts of the Matrix Product States (MPS) Representation** (a). A diagrammatic illustration of a 5-site MPS, where the horizontal lines represent the bond dimension and the vertical lines indicate physical indices with dimension σ. (b). The left and (c) the right orthonormal MPS tensors are depicted using triangles. (d) i. An MPS with general tensors can be transformed into the mixed canonical form by using a singular value decomposition (SVD) (d) ii. with one site center $M_C(n)$ at site n or (d) iii. with a zero site center $C(n)$, where the singular values correspond to the Schmidt coefficients of the state. The form of these illustrations is inspired by illustrations in [209, 210].

4.2.1.1 Canonical Forms of MPS

The power of MPS lies in its ability to efficiently represent certain classes of quantum states, which in turn allows for easy manipulation, and use in various algorithms. The simplest manipulations are done using QR decomposition and singular value decomposition (SVD). The SVD is a powerful and versatile tool in linear algebra that allows us to represent a matrix M of dimensions $D_A \quad D_B$ as

$$M = USV^{\dagger}. \tag{4.19}$$

Here,

- U is of dimensions $D_A \quad \min(D_A, D_B)$, and has orthonormal columns or in other words left singular vectors satisfying $U^{\dagger}U = I$.
- S is of dimension $\min(D_A, D_B) \quad \min(D_A, D_B)$, and is a diagonal matrix containing singular values λ_i.

- $V^\dagger$ is of dimensions $\min(D_A, D_B) \quad D_B$, and has orthonormal rows (right singular vectors) and satisfies $V^\dagger V = I$.

The number of non-zero singular values λ_i in S, also called the Schmidt rank, measures the degree of entanglement between two subsystems of a quantum state. Using this, we may calculate the entanglement entropy within the MPS framework, as we will discuss in Sec. 4.2.4. The SVD is also central in allowing us to truncate our bond dimension. One truncates an MPS in practice by performing an SVD on each bond, starting from the leftmost tensor and sweeping through the MPS, and retaining only the largest D singular values. Discarding some of the singular values will inevitably introduce a error in the MPS representation, which is calculated as the sum of the discarded singular values squared

$$\epsilon = \sum_{i>D} (\lambda_i)^2. \tag{4.20}$$

Alternatively, we may also go the other way around and introduce an ϵ as our cutoff, which further controls our bond dimension adaptively. In this case, the smallest singular values are discarded until the error saturates to ϵ. While SVD is widely used due to its ability to reveal important properties of matrices, another common matrix decomposition technique is the QR decomposition. Here, as the name suggests, it is the decomposition of a matrix $M = QR$, where Q is an orthonormal matrix and R is an upper triangular matrix. Given the dimension of M as $D_A \quad D_B$, and $D_A > D_B$, then the bottom $D_A \quad D_B$ rows of R are zero.

Due to the power of QR decomposition and SVD, the MPS given in Eq. (4.18) can be written as left, right, and mixed canonical forms. To create the left-canonical form of the MPS, one starts with the leftmost tensor, performs a QR decomposition, and proceeds to the right until reaching the end. For the right-canonical form, the process is done in reverse, starting from the right (See Fig. 4.2(b) and (c)). The most commonly used canonical form in the MPS framework is the mixed form, where one can perform an SVD by choosing a site n to be the center. Then $M^{[n]} = U^{[n]} \quad {}^{[n]}V^{[n]}$, where $U^{[n]}$ is

left-orthogonal matrix, $^{[n]}$ is diagonal with singular values and $V^{[n]}$ is right-orthogonal. Mathematically, one can write the MPS given in Eq. (4.18) in a mixed canonical form as

$$|\psi\rangle = \sum_{\alpha,\beta,\sigma_n} M(n)^{\sigma_n}_{C\ \alpha,\beta} \left|\phi^{[1:n\ \ 1]}_{L,\alpha}\right\rangle |\sigma_n\rangle \left|\phi^{[n+1:N]}_{R,\beta}\right\rangle \ , \tag{4.21}$$

where the new states $\left|\phi^{[1:n\ \ 1]}_{L,\alpha}\right\rangle$ and $\left|\phi^{[n+1:N]}_{R,\beta}\right\rangle$ form an orthonormal basis of the left and right blocks respectively [204, 210]. The mixed canonical form can be expressed as either a one-site center $M_C(n)$ at site n as shown in Fig. 4.2(d) ii. or a zero-site center $C(n)$ as shown in Fig. 4.2(d) iii., where the singular values correspond to the Schmidt coefficients of the state. In Sec. 4.2.4, we demonstrate how the mixed canonical form of the MPS is advantageous for calculating entanglement entropy. We also show its benefits in the TDVP algorithm in Sec. 4.2.3.

4.2.2 Matrix Product Operators (MPO)

Analogous to matrix product states (MPS), matrix product operators (MPO) offer a similarly structured approach for representing operators in the context of tensor networks [204, 206, 210, 214]. Here there will be N rank-4 tensors W_j as shown below (see Fig. 4.3(a))

$$\begin{aligned}\hat{O} &= \sum_{\substack{\sigma_1,\ \ ,\sigma_N,\\ \sigma_1',\ \ ,\sigma_N'}} c_{\sigma_1\ \ \sigma_N,\sigma_1'\ \ \sigma_N'} |\sigma_1\rangle\ \ |\sigma_N\rangle \langle\sigma_1'\ \ \ \sigma_N'| \\ &= \sum_{\substack{\sigma_1,\ \ ,\sigma_N,\\ \sigma_1',\ \ ,\sigma_N'\\ w_0,\ \ w_N}} W^{\sigma_1,\sigma_1'}_{1;w_0,w_1}\ \ W^{\sigma_N,\sigma_N'}_{N;w_N\ \ 1,w_N} |\sigma_1\rangle\ \ |\sigma_N\rangle \langle\sigma_1'\ \ \ \sigma_N'| \ .\end{aligned} \tag{4.22}$$

Applying an MPO to an MPS is one of the most critical operations within the framework of matrix product states. The straightforward way to do this is by tensor multiplication of the corresponding site tensors of the MPS and MPO. However, this approach results in a state with a much higher bond dimension than necessary to represent the final state efficiently.

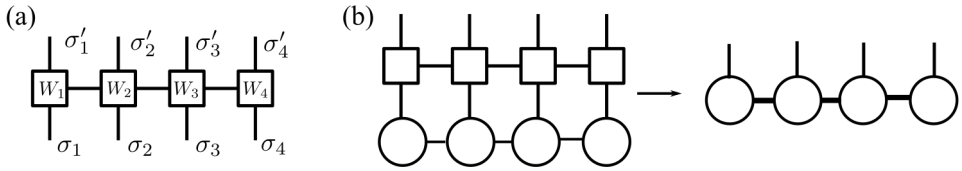

Figure 4.3: **Basic Concepts of the Matrix Product Operators (MPO) Representation** (a). A diagrammatic illustration of a 4-site MPO. The horizontal lines represent the bond dimension, whereas the vertical lines indicate physical indices with dimension d. (b). Applying an MPO directly to an MPS results in an MPS with an increased bond dimension, which is depicted by thick horizontal lines.

Despite this, we briefly discuss how the form of the MPS remains unchanged [204, 210]. While more sophisticated methods like variational application and zip-up method exist [204, 210], they are beyond the scope of this thesis. In most of our simulations in Ch. 7, after applying an MPO to an MPS, we truncate the resulting state to a specified bond dimension.

When the operator $\hat{O}$ (See Eq. (4.22)) acts on state $|\psi\rangle$ (See Eq. (4.18)), we get

$$\hat{O}|\psi\rangle = \sum_{\substack{\sigma_1, \ldots, \sigma_N, \\ \sigma'_1, \ldots, \sigma'_N, \\ \sigma''_1, \ldots, \sigma''_N}} \sum_{\substack{w_0, \ldots w_N \\ m_0 \ldots m_N}} \left(W^{\sigma_1,\sigma'_1}_{1;w_0,w_1} \cdots W^{\sigma_N,\sigma'_N}_{N;w_{N-1},w_N}\right)\left(M^{\sigma''_1}_{1;m_0,m_1} \cdots M^{\sigma''_N}_{N;m_{N-1},m_N}\right) |\sigma_1 \ldots \sigma_N\rangle \langle \sigma'_1 \ldots \sigma'_N | \sigma''_1 \ldots \sigma''_N\rangle \,. \tag{4.23}$$

This gives

$$\begin{aligned}\hat{O}|\psi\rangle &= \sum_{\substack{\sigma_1, \ldots, \sigma_N, \\ \sigma'_1, \ldots, \sigma'_N}} \sum_{\substack{w_0, \ldots w_N \\ m_0 \ldots m_N}} \left(W^{\sigma_1,\sigma'_1}_{1;w_0,w_1} M^{\sigma'_1}_{1;m_0,m_1}\right) \cdots \left(W^{\sigma_N,\sigma'_N}_{N;w_{N-1},w_N} M^{\sigma'_N}_{N;m_{N-1},m_N}\right) |\sigma_1 \ldots \sigma_N\rangle \langle \sigma'_1 \ldots \sigma'_N| \\ &= \sum_{\substack{\sigma_1, \ldots, \sigma_N, \\ w_0, \ldots, w_N \\ m_0 \ldots m_N}} N^{\sigma_1}_{1;(w_0 m_0),(w_1 m_1)} \cdots N^{\sigma_N}_{N;(w_{N-1} m_{N-1}),(w_N m_N)} |\sigma_1 \ldots \sigma_N\rangle = |\phi\rangle \,. \end{aligned} \tag{4.24}$$

The resulting state $|\phi\rangle$ is hence again an MPS, but with a larger dimension $m' = m \cdot w$ as illustrated in Fig. 4.3(b). Repeated application of an operator onto a state rapidly increases the state's dimension, necessitating truncation.

4.2.3 Time Evolution of Matrix Product States

The power of the tensor network representation of states also seeps into the studies of the dynamical properties of the system using time evolution methods. This includes *time evolving block decimation method* (TEBD) [203, 215–218] and *time-dependent variational principle* (TDVP) [208–212].

Time evolution of state with a given Hamiltonian $\hat{H}$ involves exponentiation of the Hamiltonian, and at the core, the TEBD algorithm is based on the Lie-Trotter Suzuki decomposition of $\exp\{-it\hat{H}\}$ [219, 220]. When the decomposed individual terms are local, they can be applied efficiently and the tensor network can be updated accordingly. However, the TEBD algorithm is not effective when we have systems with long-range interactions. This is where the time-dependent variational principle becomes particularly significant. Here, we focus on TDVP as we use it extensively in our simulation of dynamics in continuous time models.

4.2.3.1 Time-Dependent Variational Principle (TDVP)

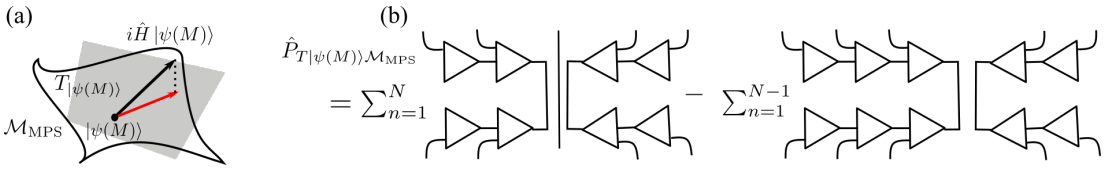

Figure 4.4: **An Illustration of MPS Manifold and Tangent Space Approximation** (a). An illustration depicting the MPS manifold $\mathcal{M}_{\mathrm{MPS}}$ as the solid frame and the black dot represents the MPS $|\psi(M)\rangle$. The grey square represents the tangent plane $T_{|\psi(M)\rangle}$. The black arrow is the direction $i\hat{H}|\psi(M)\rangle$ of time evolution, and the red arrow represents the vector that best approximates $i\hat{H}|\psi(M)\rangle$ in the tangent plane. (b). The tangent space projector operator (up to a factor of i). For an N site tensor, the first term of the projector is a summation over the different physical sites of the MPS. The second term is the summation over the bonds in the MPS. For a given MPS of N tensors, there are $N - 1$ bonds, and hence n sums from 1 to $N - 1$. The form of these illustrations is inspired by illustrations in [208, 209]

The MPS representation of a given quantum state resides in a variational manifold [2]. When a time evolution operator is applied to this MPS, it typically causes the MPS to

[2] The variational manifold of MPS refers to the set of all possible states that can be represented by an MPS with a given bond dimension.

leave this manifold. The Time-Dependent Variational Principle (TDVP) addresses this by projecting the time evolution onto the tangent space of the manifold, ensuring that the evolution remains within the MPS manifold $\mathcal{M}_{\mathrm{MPS}}$. This idea has been depicted in Fig. 4.4(a). Indeed as shown in [208], this can lead to a complicated set of equations, however, [209] showed a different scheme to understand this using the tensor network route. Mathematically, this means

$$\frac{d|\psi(M)\rangle}{dt} = -i\hat{P}_{T|\psi(M)\rangle\,\mathcal{M}_{\mathrm{MPS}}}\hat{H}|\psi(M)\rangle \ , \tag{4.25}$$

where M is a set of site-dependent matrices defined in Eq. (4.18) and the time-evolving states can be described by $|\psi(M(t))\rangle$. The tangent space projector can be decomposed as (see Fig. 4.4(b) for the diagrammatic representation)

$$\hat{P}_{|T\psi(M)\rangle\,\mathcal{M}_{\mathrm{MPS}}} = \sum_{n=1}^{N} \hat{P}_L^{[1:n-1]} \otimes \hat{\mathbb{1}}_n \otimes \hat{P}_R^{[n+1:N]} \sum_{n=1}^{N-1} \hat{P}_L^{[1:n]} \otimes \hat{P}_R^{[n+1:N]}, \tag{4.26}$$

where

$$\hat{P}_L^{[1:n]} = \sum_{\alpha=1}^{D} \left|\phi_{L,\alpha}^{[1:n]}\right\rangle \left\langle\phi_{L,\alpha}^{[1:n]}\right| \ , \tag{4.27}$$

$$\hat{P}_R^{[n:N]} = \sum_{\beta=1}^{D} \left|\phi_{R,\beta}^{[n:N]}\right\rangle \left\langle\phi_{R,\beta}^{[n:N]}\right| \ , \tag{4.28}$$

are described as a combination of left and right canonical forms as discussed in Sec. 4.2.1.1.

The state $|\psi(M)\rangle$ can be expressed in the form given by Eq. (4.21) followed by the application of $\hat{P}_{T|\psi(M)\rangle\,\mathcal{M}_{\mathrm{MPS}}}$ onto $\hat{H}|\psi(M)\rangle$. We can identify the one-site or zero-site effective Hamiltonian $H(n)$ (see Fig. 4.5(b) i.) or $K(n)$ (see Fig. 4.5(b) ii.) by appropriately choosing the center n. The construction of tangent space projector into individual sites n is a direct reflection of the Lie-Trotter splitting scheme. For a given site n, the operator $\hat{P}_L^{[1:n-1]} \otimes \hat{\mathbb{1}}_n \otimes \hat{P}_R^{[n+1:N]}\hat{H}$ applied to state $|\psi(M)\rangle$ reduces to solving the differential equation $\dot{\mathbf{M}}_C(n,t) = -iH(n)\mathbf{M}_C(n,t)$. Here, a bold notation is used for the vector representation, $M_C(n,t)$ is the matrix at site n defined in Eq. (4.18) and

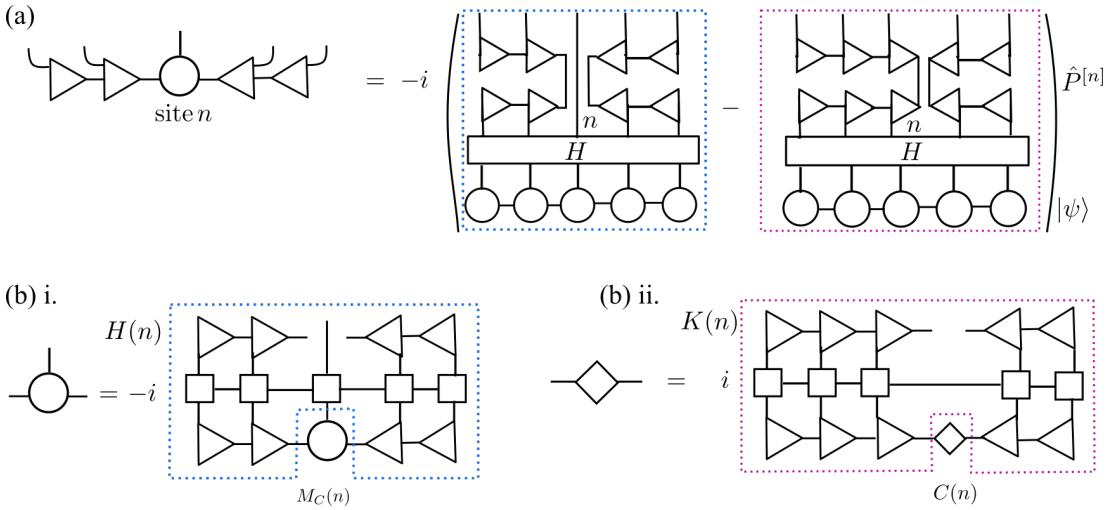

Figure 4.5: **A Diagrammatic Representation of the Time-Dependent Variational Principle (TDVP)** (a). An illustration of Eq. (4.25) within the tensor network framework, where each term in the projector operator is highlighted as blue and pink dotted boxes respectively. Each term is further decomposed into two parts: (b) i. corresponding to Eq. (4.29), and (b) ii. corresponding to Eq. (4.30). These illustrations are inspired by [209].

the subscript C signifies that this site is the center. This leads to

$$M_C(n,t) = \exp[\ \ iH(n)t]M_C(n,0). \tag{4.29}$$

In a similar vein, the second term, in the projector operators gives

$$C(n,t) = \exp[+iK(n)t]C(n,0). \tag{4.30}$$

The derivation of these equations from Eq. (4.25) is diagrammatically represented in Fig. 4.5. The evolution of C in Eq. (4.30) can be interpreted as an evolution backward in time. For this type of differential equation, it is very natural to use the Lie-Trotter decomposition approach [219, 220] along with the Krylov sub-space method. The simplest way to split this algorithm is highlighted below. For a right orthogonal MPS, start at $n = 1$ and repeat the following steps:

(1) Evolve $M_C(n)$ according to Eq. (4.29) for a time step t.

(2) Update $M_C^{\sigma_n}(n) = M_L^{\sigma_n}(n)C(n)$.

(3) Evolve $C(n)$ backwards in time according to Eq. (4.30) and then absorb it into the next site to create $M_C^{\sigma_n}(n+1) = C(n)M_R^{\sigma_n}(n+1)$.

This is known as the one-site algorithm, where, as the name implies, only a single site is updated at a time. The two-site algorithm, which is more commonly used and often more advantageous, involves updating a block of two consecutive sites simultaneously. This approach is advantageous as it enables dynamic updating of the bond dimension, which is particularly beneficial for Hamiltonian simulations where entanglement tends to increase over time. The Julia ITensor TDVP package [221, 222] implements this two-site algorithm.

4.2.4 Calculating the Measures of Scrambling Using MPS Framework

In Sec. 6.5 of Ch. 6, we study the scrambling dynamics using the tripartite mutual information introduced in Sec. 2.4. Given the importance of this measure in our analysis, we employ the MPS framework for their calculation. This approach is particularly advantageous for handling large systems and capturing the entanglement properties efficiently. While the theoretical background tripartite mutual information is covered in the aforementioned section, the focus here will be on the practical implementation of these calculations within the MPS framework.

4.2.4.1 Computing von Neumann Entanglement Entropy

The calculation of entanglement entropy using Matrix Product States (MPS) formalism is quite straightforward. The idea again utilizes singular value decomposition (SVD) of the matrix at a given center. To determine the entanglement entropy, the system is divided into two subsystems A and B. Consider a specific bipartition at site n with the MPS in a mixed canonical form, where the first n sites form bipartition A and the remaining $N \quad n$ sites constitute subsystem B. Performing an SVD at the center n, allows us to express the matrix $M_C(n) = USV^{\dagger}$, where U and V are unitary matrices and S is a diagonal matrix containing the singular values λ_i. We know that the von

Neumann entropy for a state ρ_A, as discussed in Sec. 2.2 is

$$S(\rho_A) = \mathrm{Tr}[\rho_A \log[\rho_A]] = \sum_i \lambda_i^2 \log \lambda_i^2. \tag{4.31}$$

Thus, the calculation of entanglement entropy for a pure state within the MPS formalism is notably straightforward due to the efficient application SVD.

4.2.4.2 Computing Tripartite Mutual Information

Once we have calculated the bipartite entanglement entropy for various regions, computing the tripartite mutual information simply involves performing a linear combination of these entropies. As explained in Sec. 2.4, the tripartite mutual information I_3 of three subsystems A, B, C is

$$I_3 = S_A + S_B + S_C - S_{AB} - S_{BC} - S_{AC} + S_{ABC}. \tag{4.32}$$

Computing the entanglement entropies of contiguous sub-regions (regions that share a boundary) S_A, S_B, S_C, S_{AB}, S_{BC}, and S_{ABC} is relatively straightforward because the centers can be chosen appropriately. For example, to determine S_A, the center will be the last tensor in the subsystem A touching the boundary of subsystem B as illustrated in Fig. 4.6(a). In contrast, calculating entanglement entropies for non-contiguous sub-regions, such as S_{AC}, presents greater difficulty due to the lack of shared boundaries.

One approach to address this issue involves swapping the discontiguous sub-regions B and C so that they share a boundary as illustrated in Fig. 4.6. We demonstrate in Sec. 6.5 that this method works well for small system sizes. However, as the system size increases and entanglement grows, this operation becomes more challenging. This is because the required bond dimension to represent the system increases as σD where σ is the physical dimension and D is the bond dimension of the MPS before the SWAP operation. If σD is greater than D_{cutoff}, the pre-set limit on the bond dimension of the resultant MPS, we canonicalize the MPS and then truncate the bond dimension to D_{cutoff} during the singular value decomposition.

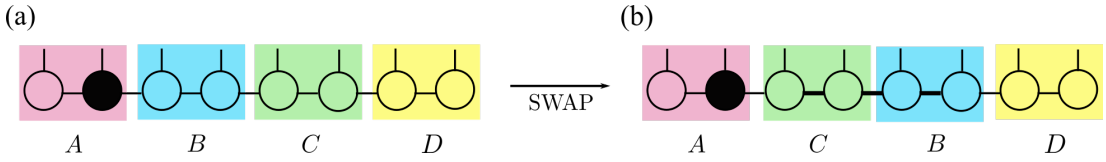

Figure 4.6: **Calculation of Entanglement Entropy and Swapping Operation Scheme in Matrix Product States Framework** (a). An 8-site MPS is divided into four contiguous subsystems: A, B, C, and D. To calculate the entanglement entropy S_A, the center of the system is marked by a filled circle, indicating the cut across which the entropy is computed. (b) For calculating the entanglement entropy S_{AC}, we first perform a SWAP operation between regions B and C. This operation increases the bond dimension to σD, where σ is the physical dimension and D is the bond dimension of the MPS prior to the SWAP. The increased bond dimension is represented by thick horizontal lines.

However, this truncation may not fully capture the underlying physics of the system. In summary, while the SWAP operation is effective for smaller systems, the increasing bond dimension for larger systems necessitates careful consideration of truncation effects. Future work may focus on optimizing these methods to better handle high entanglement scenarios and improve the accuracy of the resulting MPS representations, and the physical states for which they are applicable.

4.3 Summary

In Ch. 4, we discussed various numerical techniques that will be employed at different points throughout the thesis. In Sec. 4.1.1, we showed that circuits composed of two-qubit CNOT, and single-qubit Hadamard and Phase gates can be simulated efficiently classically in polynomial time. This efficiency is achieved because the circuit dynamics can be reduced to simple row and column operations on N $2N$ matrices, enabling the simulation of thousands of qubits efficiently. A significant aspect of our work includes the study of entanglement, and hence we used both the Stabilizer formalism and MPS/MPO frameworks to calculate the entanglement entropy as shown in Sec. 4.1.3 and Sec. 4.2.4 respectively. Furthermore, we introduced matrix product states and matrix product operators in Sec. 4.2, and showed their versatility in representing states and subsequent time evolutions. The Stabilizer formalism excels in efficiently simu-

lating certain classes of entangled states, but it is not universal and cannot generate or represent many quantum states. In contrast, the MPS-MPO framework is highly effective for simulating states with low entanglement, such as those obeying area-law scaling, but struggles with states that exhibit volume-law entanglement. Throughout the thesis, these numerical techniques are applied extensively. In Ch. 5 and Ch. 6, we use the Clifford group of gates to construct circuits for studying quantum information scrambling, exploring how information spreads. The MPS and MPO methods are particularly prominent in Ch. 7, where we investigate correlations and the metrological importance of entangled states, respectively.

Chapter 5

Probing Emergent Geometries Using Entanglement Entropy

> Science and everyday life cannot and should not be separated.
>
> Rosalind Franklin

5.1 Introduction

Quantum information scrambling as discussed in Ch. 2 involves the spreading of information to different degrees of freedom. This process is regulated by the system's inherent lightcone, which is determined by the Lieb-Robinson bound. Depending on the range of interactions, the spreading of the lightcone varies as described in Sec. 2.3. Consequently, the concepts of information spreading and geometry are closely linked. Extensive numerical, experimental, and analytical studies have been conducted to explore this relationship. A classic example is the difference between 'area-law' entanglement entropy typically found in ground states of 1D gapped systems versus the 'volume-law' ground-state entanglement found in gapless systems [87–93]. On the experimental side, the connections between patterns of entanglement and geometry have recently been explored in pioneering experiments with nonlocally-interacting spins in a cavity system [59], where spin-spin correlations were used to reconstruct the underlying geometry of

the system. Similarly, numerical simulations [30], and field theory calculations [45, 223] have been used to study sparse systems and the effective geometries that emerge from the dynamics.

In Ch. 5, we extend these ideas by numerically studying entanglement dynamics in sparse Clifford circuits with tunable-range interactions. These systems enable numerical access to strong interactions at large system sizes for a special class of many-body dynamics. We begin this chapter by introducing the two types of geometry we will explore in Sec. 5.2. Furthermore, we introduce our model in Sec. 5.3, and then use the scaling of bi-partite entanglement entropy, introduced in Sec. 2.2.1, to describe the geometry of our models in Sec. 5.4.

5.2 Euclidean and Ultrametric Geometry

Named after the ancient Greek mathematician Euclid, at heart Euclidian geometry is the way we count numbers $0, 1, 2, \quad$. This is the conventional way of ordering numbers, and the Euclidean distance between two points in the Euclidean space is defined as the length of the line segment between two points. The Euclidian norm $j \ j$ gives the distance between points x and y in the reals R.

Going beyond Euclidean (linear) geometry, we turn to an alternative numerical system: p-adic numbers forming the ultrametric space. Just like how irrational numbers along with rational numbers form the real numbers R, the p-adic numbers Q_p are an alternative extension of the rational numbers, each associated with a prime number p [224]. The distances between p-adic numbers are measured by the p-adic norm $j \ j_p$. The idea behind the p-adic norm is to use the multiplicity of the prime p in the factorization of numbers. The definition of the p-adic metric is

$$ji \quad jj_p = \begin{cases} p^{\ v_p(i \ \ j)} & (i \quad j \neq 0) \\ 0 & (i \quad j = 0), \end{cases} \tag{5.1}$$

where $v_p(\,)$ is the number of times the prime factor p is present in the factorization of the irreducible fraction $i \quad j$. Let us consider the $p = 2$-adic metric, as it will be used most frequently in this thesis. This metric gives naturally a treelike structure shown in Fig. 5.1, and this is referred to as the Bruhat-Tits tree.

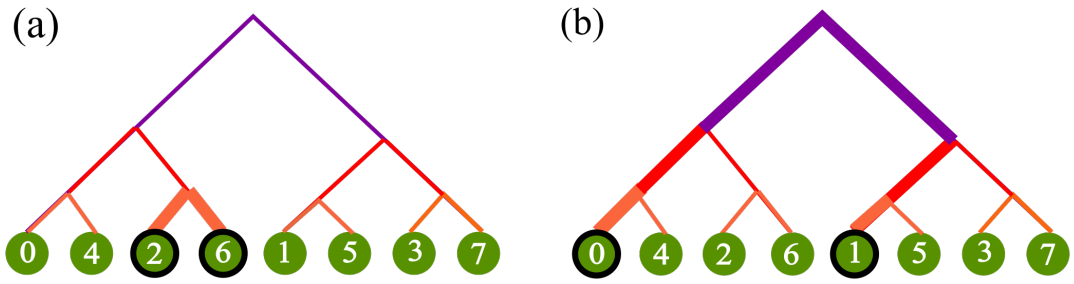

Figure 5.1: **Distances on the Bruhat-Tits Tree for $N = 8$ Sites** (a). Sites $i = 2$ and $j = 6$ are closer as within the treelike structure, one must only traverse 2 edges of the tree, thus the 2-adic norm is $ji \quad jj_2 = 2^{d_{tree}(i,j)/2}/N = 1/4$. (b). By contrast, for sites $i = 0$ and $j = 1$, one must traverse 6 edges of the tree, making it farther and $ji \quad jj_2 = 2^{d_{tree}(i,j)/2}/N = 1$.

According to Eq. (5.1), the sites $i = 2$ and $j = 6$ are separated by a 2-adic norm of $ji \quad jj_2 = 2^{\,v_2(4)} = 2^{\,2} = 1/4$, while the sites $i = 0$ and $j = 1$ are separated by a 2-adic norm of $ji \quad jj_2 = 2^{\,v_2(1)} = 2^0 = 1$. This can also be defined using the number of edges required to connect sites i and j, i.e., $d_{tree}(i, j)$. The 2-adic norm thereby can be defined as $ji \quad jj_2 = 2^{d_{tree}(i,j)/2}/N$, where N is the system size. This is illustrated in Fig. 5.1. Perhaps surprisingly, this definition satisfies the usual axioms required of a metric and therefore serves as a useful notion of distance. One of the notable and crucial properties of the p-adic numbers is their ultrametricity, thus obeying the strong triangle inequality $ji \quad jj_2 \quad \max(ji \quad kj_2\,, jj \quad kj_2)$ for all i, j, k. This gives it a hierarchical structure, where decreasing v_p implies moving deeper into the tree as shown in Fig. 5.1.

To arrange integers sequentially using the p-adic norm, one can use a map M called Monna map introduced by Monna [225]. Let $N = p^n$, where n is an integer, then

$x \; 2 \; f0, 1, 2, \ldots, N \quad 1g$ can be expressed as

$$x = \sum_{q=0}^{n \quad 1} x_q p^q, \tag{5.2}$$

where $x_q \; 2 \; f0, 1, \ldots, p \quad 1g$. Then the Monna map M is defined as

$$M(x) \quad \sum_{q=0}^{n \quad 1} x_{n \quad 1 \quad q} p^q, \tag{5.3}$$

which means that we reverse the digits in the base p of expansion x. Using this definition of Monna Map for $p = 2$, we reverse the binary equivalent of the argument. This leads to the treelike ordering of qubits as illustrated in Fig. 5.2.

5.3 Sparse Clifford Circuits

Here we explore the emergence and collapse of tunable lightcones in a family of tunable-range quantum circuit models featuring sparse interactions. In our model, pairs of qubits in a 1-dimensional chain are coupled if and only if they are separated by a power of 2: $ji \quad jj = 2^{m \quad 1}$ for $m = 1, \ldots, \log_2 N$ (See Fig. 5.2(a)). This is called the *Powers of two model (PWR2) model.* and features sparse nonlocal interactions.

A tunable parameter s controls how these couplings either decay ($s < 0$) or grow ($s > 0$) with distance as illustrated in Fig. 5.2(b). The gates are arranged in a non-local bricklayer pattern with interaction layers stacked into an alternating sequence of 'even' and 'odd' blocks. During the 'even' block, a gate Q_{ij} is placed between qubits $i < j$ with probability $p(ji \quad jj, s)$ if and only if $\mathrm{mod}(bi/2^{m \quad 1}c, 2) = 0$. During the subsequent *odd* block, gates are placed according to the same rules but with the odd-bricklayer condition $\mathrm{mod}(bi/2^{m \quad 1}c, 2) = 1$ [200].

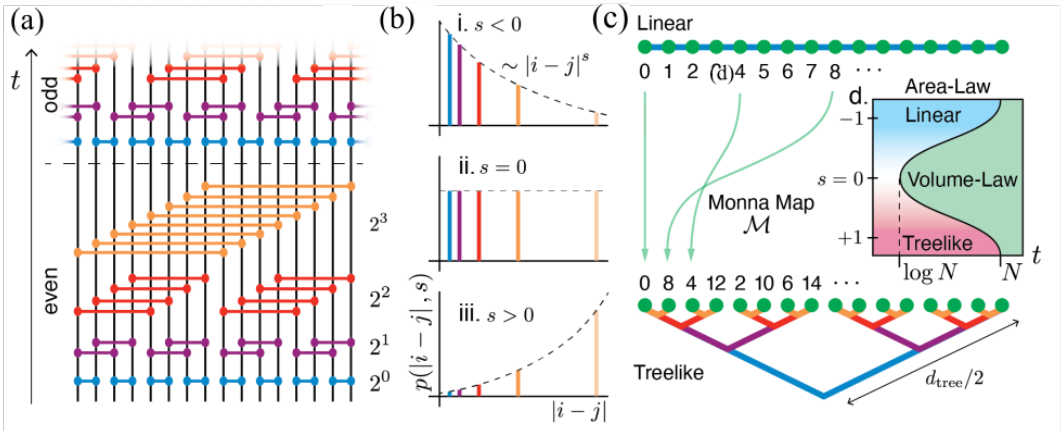

Figure 5.2: **Sparse Clifford Circuits Yielding Tunable Geometries.** (a) The powers of two model (PWR2) featuring qubits i, j arranged in a linear chain interacting pairwise if and only if they are separated by a power of two, $ji \quad jj = 2^{m-1}$ for $m = 1, 2, \ldots, \log_2 N$. To mimic continuously-tunable interactions in a discrete circuit, we arrange random two-qubit gates into even and odd bricklayer blocks and randomly apply each gate Q_{ij} with probability $p(ji \quad jj, s)$ given in Eq. (5.4). (b) A tunable power-law exponent s controls whether this distribution decays ($s < 0$, top) or grows ($s > 0$, bottom) with distance. At $s = 0$, all the qubits are coupled with all other qubits with equal probability as shown in the middle. (c) The structure of entanglement generated by these circuits indicates linear (Euclidean) geometry when $s < 0$ and the treelike geometry of the 2-adic numbers when $s > 0$. (d) Numerical studies of entanglement entropies as a function of time reveal three distinct regimes: a linear area-law regime (blue) when $s < 0$, a treelike area-law regime (red) when $s > 0$, and a volume-law regime (green) at late times. In the two local regimes $jsj > 1$, volume-law entanglement builds up on a timescale $t \quad N$ that grows linearly with the system size, but near $s = 0$ fast scrambling dynamics generates volume-law entanglement on timescales as short as $t \quad \log N$. This figure was reproduced from [42].

The probability of applying a two qubit Clifford gate $Q_{ij} = Q_{ji}$ at each timestep t is

$$p(ji \quad jj, s) = \begin{cases} J_s \, ji \quad jj^s & \text{when } ji \quad jj = 2^{m-1} \\ 0 & \text{otherwise,} \end{cases} \tag{5.4}$$

where the normalisation ensures that a single gate on average is applied per site at each timestep t. This naturally gives the value of the normalisation factor as

$$1/J_s = \frac{1}{2}\left(\frac{N}{2}\right)^s + \sum_{m=1}^{\log_2 N} 2^{(m-1)s}. \tag{5.5}$$

Thus, short-distance gates dominate the Clifford circuit when $s < 0$ while long-distance gates dominate when $s > 0$ (Fig. 5.2(b) top and bottom). At the midpoint $s = 0$, gates at all length scales are equally probable in the circuit (Fig. 5.2(b) middle). Here and throughout this chapter, we impose periodic boundary conditions, such that the linear distance $|i-j|$ between a pair of sites is the smaller of $\text{abs}(i-j)$ and $N - \text{abs}(i-j)$. The idea of the probabilistic application of gates is to mimic the continuous time coupling matrix $[J(|i-j|, s)]$ [30]. In Sec. 5.4, we study the entanglement entropies S_A of contiguous regions A of output qubits prior to the scrambling time and show that the area-law or volume-law scaling of the entropy in these regions at early times allows us to extract information about the geometry.

5.4 Results

We begin characterising the geometry generated by the circuit discussed in Sec. 5.3 by examining the pattern of entanglement present in various subregions A of the output qubits as illustrated in Fig. 5.3(a). Because the circuit is composed entirely of Clifford gates, we may completely characterise the entanglement in the system at any time t by computing Rényi entropies $S_A \quad S_A^{(2)} = \log \text{Tr}\left[\rho_A^2\right]$ of various subregions A [196, 198]. This is because the Clifford group has flat entanglement spectra, and the second-order Rényi entropy equals the von Neumann entanglement entropy as explained in Sec. 4.1.3. In this section, we study Rényi entropies of *contiguous* subregions A, where the meaning of the word 'contiguous' depends on the geometry implied by the interactions, as explained below.

A linearly-contiguous region A has the property that any bipartition $A = A_1 \bigcup A_2$ is contiguous with respect to the Euclidean metric defined in the Sec. 5.2.

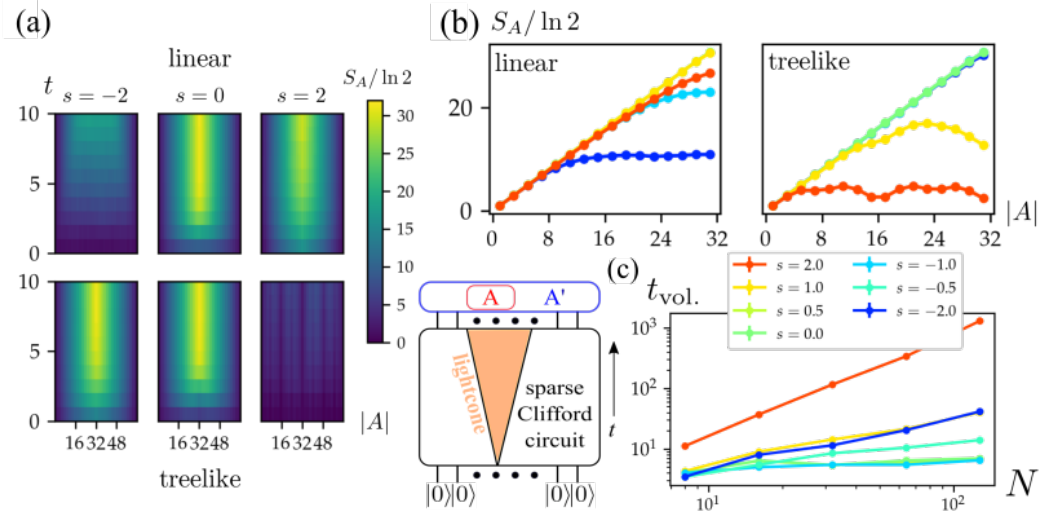

Figure 5.3: **Probing Tunable Geometry Using Entanglement Entropy** (a) Entanglement growth in contiguous subregions A in a system of $N = 64$ qubits initialized in the product state $|0\rangle^{\otimes N}$, plotted as a function of subregion size $|A|$ and time t in linear (top) and treelike (bottom) geometries. (b) A time-slice at $t = 6$ from the colormap illustrates the area-law scaling and volume-law scaling for linear (left) and treelike (right) geometries. When $s < 0$, linearly contiguous subregions A exhibit area-law entanglement at short times, while other subregions are trivially volume-law entangled. When $s > 0$, treelike subregions have area-law entanglement at short times, while other regions are volume-law entangled. (c) The timescale $t_{\text{vol.}}$ required to reach volume-law entanglement grows polynomially with system size $N = 2^3, \quad , 2^7$ when $|s| > 1$, but is much shorter near $s = 0$, consistent with a logarithmic scrambling time $t_{\text{vol.}} \quad \log N$. Error bars are shown or are smaller than data points. Data points are obtained by averaging over 10^2 trajectories. This figure was reproduced from [42].

This means that for every $i \in A_1$, there exists a $j \in A_2$ such that $|i - j| = 1$. When $s < 0$, we find that the entanglement generated by the circuit is organized into linearly contiguous subregions. By contrast, in the limit $s > 0$, we find that the entanglement in the circuit is organized into treelike-contiguous regions defined by the treelike (2-adic) metric given in Eq. (5.1). A treelike-contiguous region A is defined by the property that any bipartition $A = A_1 \bigcup A_2$ is contiguous with respect to the treelike (2-adic) metric: for every $i \in A_1$, there exists a $j \in A_2$ such that $|i - j| \quad |j_2 = 2|/N$ for N a power of 2. One can obtain the sites i, j in the treelike ordering by rearranging the qubits by the discrete Monna map M, which reverses the digits of the argument when written in base 2 as shown in Sec. 5.2. For example, in a system with $N = 8$ qubits, site 1 is

mapped to site $M(1) = 4$ under the Monna map because $M(001_2) = 100_2$ when the site numbers are written in binary. Simply relabeling the sites under the Monna map M is not enough to constitute a distinct geometry, but the treelike structure of the 2-adic metric $|i - j|_2$ endows this arrangement with a notion of distance that is entirely different from the conventional metric $|i - j|$ in linear (Euclidean) geometry [43, 226–230].

We expect typical contiguous subregions A of output qubits to be volume-law entangled $S_A \propto |A|$ when they are small enough to lie entirely inside the system's many-body lightcone, but to cross over to area-law entanglement $S_A \propto$ const. when the region becomes much larger than the extent of the lightcone at a given time, as illustrated in Fig. 5.3(a). On the contrary, geometrically disjoint subregions—for example, arbitrary subsets of $k \ll N$ qubits chosen at random from anywhere in the system—typically exhibit volume-law entanglement after only a single layer of gates, which originates trivially from the short-range entanglement in the system. This distinction between area-law and volume-law scaling in the entanglement entropy therefore provides a simple and sharp test of geometrical contiguity. Specifically, contiguous subregions A should exhibit area-law entanglement scaling at short times, whereas non-contiguous subregions should exhibit volume-law scaling. We therefore proceed to use the scaling of the Rényi entropy with subregion size $|A|$ as a quantitative probe of the system's geometry. This is clearly illustrated in Fig. 5.3, where we analyze the growth of entanglement in the sparse Clifford circuit acting on qubits initialized in a product state $|0\rangle^{\otimes N}$, where $|0\rangle$ is the ground state of the Pauli-Z operator. The colour shading in Fig. 5.3(a) shows the entanglement entropy S_A of contiguous subregions A as a function of their size $|A|$ and time t with either linearly-contiguous bipartitions (top) or treelike-contiguous bipartitions (bottom).

Taking a time-slice $t = 6$ from Fig. 5.3(a), we find area-law scaling in the linear geometry at negative values of $s < 0$ (Fig. 5.3(b), left), whereas other choices of geometry yield volume-law entanglement. Similarly, at positive values of $s > 0$ we find area-law scaling in the treelike geometry and volume-law entanglement for other choices of ge-

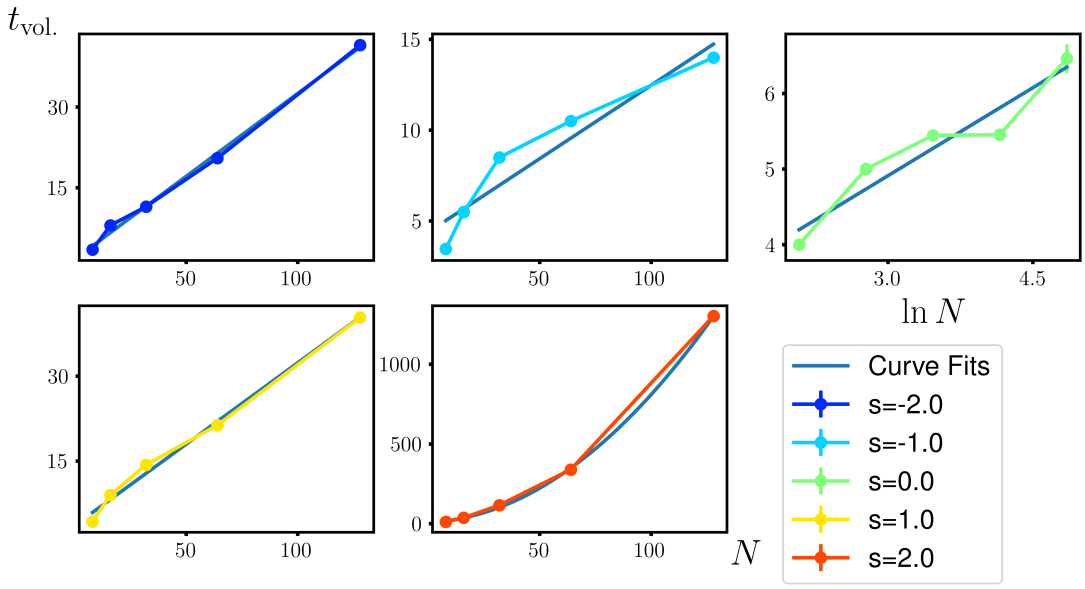

Figure 5.4: **Curve Fits for Timescale** $t_{\text{vol.}}$. We use linear fits on $t_{\text{vol.}}$ and N data for s 1, and $t_{\text{vol.}}$ and $\log N$ data for $s = 0$. In the treelike $s > 0$ limits, we use the sth degree polynomial to show that the timescale $t_{\text{vol.}}$ grows polynomially in the system size. Error bars are shown or are smaller than data points. This figure was reproduced from [42].

ometry (Fig. 5.3(b), right). The non-monotonic features appearing at early times in Fig. 5.3(b) are a direct result of the treelike geometric structure present in the circuit at large $s > 0$. For instance, a treelike region consisting of precisely half the qubits $|A| = N/2$ has especially low entropy at early times coming from the weakest long-range interactions in the deepest parts of the tree (blue couplings in Fig. 5.2(c). By contrast, smaller treelike regions $|A| < N/2$ will have additional entropy coming from couplings higher in the tree (purple, red, orange in Fig. 5.2(c). Together, these observations confirm that the entanglement entropy has a volume-law scaling for typical regions A and an area-law scaling S_A $O(1)$ when the regions are chosen to be either linearly- or treelike-contiguous depending on the value of s.

Finally, we estimate the timescale $t_{\text{vol.}}$ required for extensive contiguous regions $|A| = N/2$ to saturate to volume-law entanglement. In the linear regime $s < 0$, we find that this timescale grows linearly in the system size $t_{\text{vol.}}$ N for large system sizes. In the

treelike regime $s > 0$, on the other hand, we find that this timescale grows polynomially in the system size $t_{\text{vol.}}$ N^{jsj} for large system sizes. This is expected because the local geometry in each case inhibits the spreading of quantum information through the system, and an extensive subregion A cannot become volume-law entangled until the lightcone of a single qubit has spread to of order jAj qubits [96]. By contrast, near the crossover point $s = 0$ the circuit achieves volume-law entanglement on much shorter timescales consistent with logarithmic scaling $t_{\text{vol.}}$ $\log N$, which indicates fast scrambling dynamics [15, 20, 29–35]. Additionally, we fit the data according to theoretical predictions outlined in [30, 42, 96], as shown in Fig. 5.4. When s 1, we linear fit $t_{\text{vol.}}$ and N, in the treelike regime ($s > 0$), we fit the sth degree polynomial in N and at the crossover point $s = 0$, we linear fit $t_{\text{vol.}}$ and $\log N$. While these fits align with theoretical expectations, slight deviations are observed for smaller system sizes, particularly for $s =$ 1 and $s = 0$. These deviations are likely due to finite-size effects and are expected to diminish for larger systems, as demonstrated in [42].

5.5 Conclusions

In Ch. 5, we studied the tunable effective geometries that emerge in sparse circuits, using Clifford circuits as toy models. To characterise the effective geometries in these circuits we numerically computed Rényi entropies of contiguous regions of output qubits A as a function of time, where the term 'contiguous' is defined either according to the linear (Euclidean) metric ji jj or according to the treelike 2-adic metric ji jj_2. In Sec. 5.4, we found area-law entanglement at short times $t < N$ in both of the local regimes $jsj > 1$, indicating linear entanglement growth for negative $s < 0$ and treelike entanglement growth in a treelike geometry for positive $s > 0$. Near $s = 0$, the time taken to reach volume law entanglement scales logarithmically with system size N, i.e. t_{vol} $\log N$. This is the fast scrambling region. In Ch. 6, we explore the region around $s = 0$ at early times to study the onset of scrambling.

Chapter 6

Onset of Scrambling as a Dynamical Transition

> My methods are really methods of working and thinking; this is why they have crept in everywhere anonymously.
>
> Emmy Noether

6.1 Introduction

In Ch. 5, we explored the transition in the underlying geometry of the quantum system by systematically studying the scaling of the bipartite entanglement entropy of various subregions for different values of the tunable power law exponent s for the powers of two (PWR2) coupling graph. Notably, at $s = 0$, we observed a fast scrambling regime, where information spreads in a time logarithmically proportional to the system size N. This makes the region around $s = 0$ particularly interesting, as it allows for the generation of entangled states in such a way that the relevant system size can grow exponentially with the coherence time [15, 20, 29–35, 231]. In this chapter, we further investigate the region around $s = 0$, by studying the dynamics of information spreading using the tripartite mutual information introduced in Sec. 2.4. We identify the onset of

scrambling at *early times* as a dynamical transition in quantum circuits with different levels of long-range connectivity controlled by the same s. In particular, we show that, as a function of the interaction range for circuits of different structures, the tripartite mutual information exhibits a scaling collapse around a critical point between two clearly defined regimes of different dynamical behaviour. Importantly, we focus on a fixed timescale t $O(1)$ that does not grow with system size. At these early times, the signatures of the dynamical transition are particularly sharp, making them promising for experimental observation. Importantly, focusing on early times may allow for the generation of entangled states using shallow-depth quantum circuits, which could be more feasible to simulate and implement in experiments. This transition is reminiscent of the analysis done in [231]; however, in our study, we do not employ projective measurements.

We start this chapter by introducing all considered models used to study the transition in Sec. 6.2. This includes one experimentally realisable model (see Sec. 6.4), which maybe potentially implemented using neutral atom arrays equipped with optical tweezers. The transition is also studied analytically using an associated Brownian circuit model in Sec. 6.3, and we show that this transition can be mapped onto the statistical mechanics of a long-range Ising model for a particular region of parameter space defined by s and time t. Finally, we summarise our finding in Sec. 6.6.

6.2 Models Studied

The models used to explore the transition are again the quantum circuits in 1+1D where qubits $i, j = 0, 1, \ldots N$ 1 are arranged in a linear chain and interact via random two-qubit gates that depend on the linear distance $d = ji$ jj between them. In these circuits we apply two-qubit gates Q_{ij} between qubits i and j with probability

$$p(ji \quad jj, s) = J\, ji \quad jj^{s}, \tag{6.1}$$

where the normalisation factor J ensures that, on average, one gate is applied per site during each time step $t = 0, 1, 2, \ldots$ It follows that, regardless of s, the average number of gates applied per qubit is a constant at any given time step t.

6.2.1 Weighted Random All-To-All (WrAA) Model

The weighted random all-to-all (WrAA) model interpolates between the nearest neighbour model and random all-to-all regimes with a tunable parameter s. In this model, in each circuit layer, the qubits are randomly paired up, and a random two-site gate from the Clifford group is applied with probability $p(d, s)$ on each qubit pair, where

$$p(d, s) = J_{s,\mathrm{WrAA}} d^{s}. \tag{6.2}$$

Here $d = \min\{N - ji - jj, ji - jj\}$ is the inter-qubit distance with periodic boundary conditions.

Using the definition of the normalisation factor discussed after Eq. (6.1),

$$1/J_{s,\mathrm{WrAA}} = (N/2)^{s} + 2\sum_{d=1}^{N/2-1} d^{s} \tag{6.3}$$

ensures that each site, on average, has only one gate applied to it at each time step t. This is achieved after $N - 1$ circuit iterations, where each circuit iteration as shown in Fig. 6.1(a) is composed of applying two-qubit gates followed by randomly permuting the qubits. To characterise the onset of scrambling in this system, we calculate the tripartite mutual information I_3 of three contiguous regions A, B and C of size $N/4$ in the output state, across system sizes $N = 32, 64, \ldots, 1024$, for different values of s initialised in the z-polarized state. I_3 between three subregions A, B, C of the output qubits is expressed as

$$I_3 - I(A:B:C) = I(A;B) + I(A;C) - I(A;BC), \tag{6.4}$$

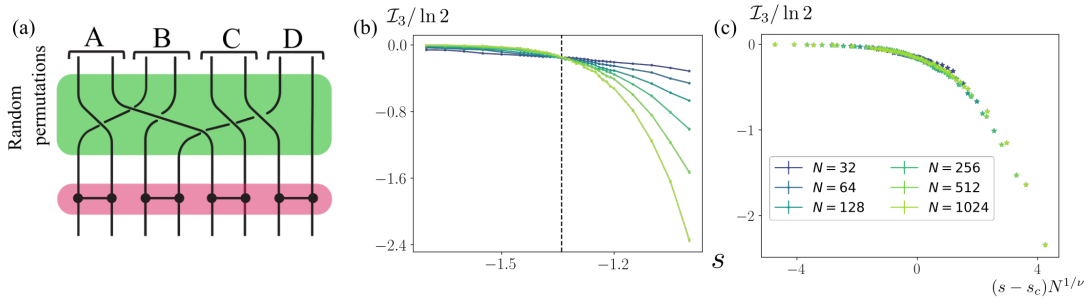

Figure 6.1: **Onset of Scrambling in Weighted Random All-to-All Model** (a). An illustration of a single circuit iteration of the weighted random all-to-all (WrAA) model that is composed of applying two-qubit gates Q_{ij} followed by shuffling of the qubits to generate random permutations. The gates between qubits i, j are applied with probability as given in Eq. (6.2). (b). Tripartite mutual information between three output regions A, B, and C as a function of the tunable parameter s for various systems sizes $N = 32, \ldots, 1024$ (see legend in (c) for colours and markers) at a fixed time step $t = 1$. (c). Scaling ansatz for I_3 gives $\nu = 2.72 \quad 0.52$ and $s_c = \quad 1.33$. The numerical results are obtained by averaging over 5000 random circuit realisations. Error bars are shown or are smaller than datapoints; lines are guides to the eye. This figure was reproduced from [44].

where $I(A;B) = S_A^{(2)} + S_B^{(2)} \quad S_{AB}^{(2)}$ is the mutual information between subregions A and B. Our circuit models are composed of Clifford gates, and the states created by these gates have $S_A = S_A^{(2)} = \quad \log \mathrm{Tr}[\rho_A^2]$ as discussed in Sec. 4.1.3. The second Rényi entropy is therefore sufficient to completely characterise the system's entanglement spectrum. As discussed in Sec. 2.4, the negativity of I_3 serves as an indicator of scrambling. Crucially, note that Bell pairs (bipartite entanglement) shared between qubits are not enough to generate negativity in I_3. To investigate this, we consider a scenario where every qubit in subregions A, B, C, and D in Fig. 6.1(a) forms a pair with a qubit outside the subregion (e.g. a qubit in A pairing with a qubit in subregion B, C or D but does not pair with other qubits in the subregion A). This is the scenario where the entanglement entropy of the given subregion is maximized, and hence the information in a subregion is completely delocalised just from the non-overlapping formation of bell pairs. Thus, the second-order Rényi entropy for region A, B, C, and D will be maximum at $S_A = S_B = S_C = N/4$. However, $S_{XY} = N/2 \quad 2N_{XY}$, where $X \in Y \subseteq \{A, B, C, D\}$ and N_{XY} are the number of bell pairs within the subregion. In

this case, I_3 defined in Eq. (6.4) becomes

$$I_3 = 2(N_{AB} + N_{AC}) \quad \frac{N}{2} + 2N_{BC}. \tag{6.5}$$

With the constraints $N_{AB} + N_{AC} = N/4 \quad N_{AD}$ and $N_{BC} = N_{AD}$, Eq. (6.5) goes to 0, i.e., $I_3 = 0$.

At fixed time step $t = 1$, we observe a transition marking the onset of scrambling at a critical value of $s = s_c$, as shown in Fig. 6.1(b). Each data point in these plots is obtained by averaging over a given number of circuit realisations (CR), with error bars representing the uncertainty in the mean. The error is calculated as the standard error SE $= \sigma / \sqrt{\text{CR}}$, where σ is the standard deviation of data. The critical point s_c is located by looking for a crossing as the system size varies between $64 \quad N \quad 1024$, indicated by a black dashed line in Fig. 6.1(b). Near this transition, the tripartite mutual information I_3 exhibits a scaling collapse, as shown in Fig. 6.1(c). We find empirically that the data collapse is well-described by the scaling theory [232–235]

$$I_3 = N^{\zeta/\nu} f(|s \quad s_c|N^{1/\nu}), \tag{6.6}$$

where f is a universal scaling function, ν is the critical exponent and $\zeta = 0$. The data collapses down to universal curves and the estimated values of $s_c = \quad 1.33$ and $\nu = 2.72 \quad 0.52$. These routines are carried out by using the scientific Python package pyfssa [235, 236].

We also check the robustness of this transition for different sub-region sizes, with A, B, C, and D each having a size of $N/8$. I_3 of three contiguous subregions of size $N/8$ in the output state is plotted as a function of the tunable parameter s for the weighted random all to all model across system sizes $N = 32, 64, .., 1024$ in Fig. 6.2(a). We observe a transition at $t = 1$ marking the onset of scrambling, indicating that the transition remains stable with respect to changes in sub-region sizes. This transition occurs at the same critical point $s_c = \quad 1.33$. We also observe scaling collapse in Fig. 6.2(b),

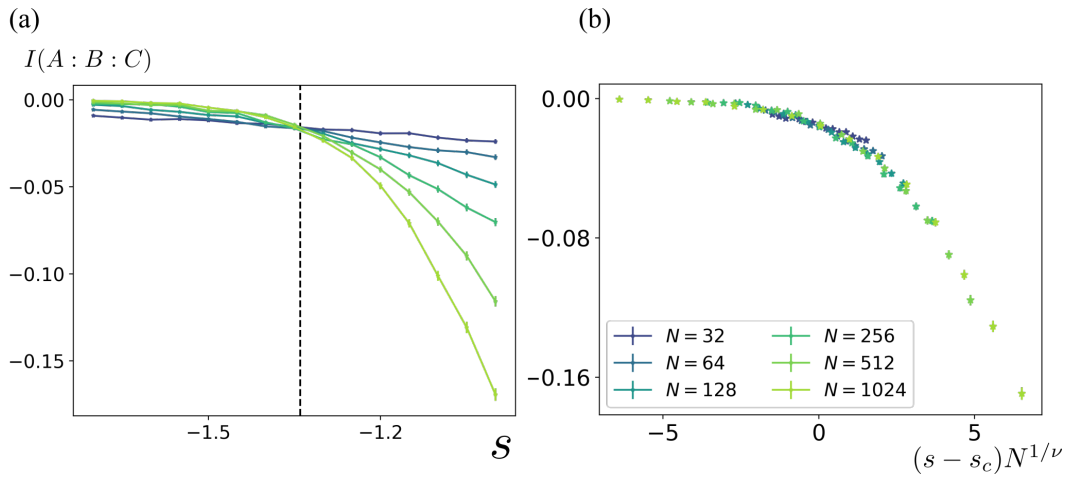

Figure 6.2: **Robustness of the Dynamical Transition.** (a) Tripartite mutual information between three output regions A, B, and C of size $N/8$ as a function of the tunable parameter s for various systems sizes $N = 32, .., 1024$ (see legend in (b) for colours and markers) for weighted random all to all model at a fixed time step $t = 1$. (b). Scaling ansatz for I_3 gives $\nu = 2.23 \quad 0.67$ and $s_c = \quad 1.33$. The numerical results are averaged over 12000 random circuit realisations. Error bars are shown or are smaller than datapoints. This figure was reproduced from [44].

with the same critical exponent $\nu = 2.23 \quad 0.67$. This provides an additional evidence that this is a bonafide critical point that emerges from the properties of the bulk and does not depend on the boundary conditions.

6.2.2 Powers of Two (PWR2) Model

In Sec. 6.2.1, we studied the transition in a densely connected all-to-all model. In this section, we extend our exploration to the sparsely coupled graphs introduced in Sec. 5.3. In this model, qubits are coupled if, and only if, they are separated by an integer power of 2: $ji \quad jj = 2^m \quad 1$ for $m = 1, \ldots, \log_2 N$ as shown in Fig. 5.2(a). As discussed in Ch. 1 and Ch. 5, the motivation to study these models stems from both theoretical interest, as they generate fast scrambling, and experimental relevance, with potential near-term implementation on platforms such as atoms in optical cavities [59] and neutral atom arrays equipped with optical tweezers [35, 53, 237]. Here, the two-qubit gates Q_{ij} are chosen randomly from the Clifford group and are applied in a brick-work pattern. As explained in Sec. 5.3, this consists of even and odd blocks, and one circuit layer will

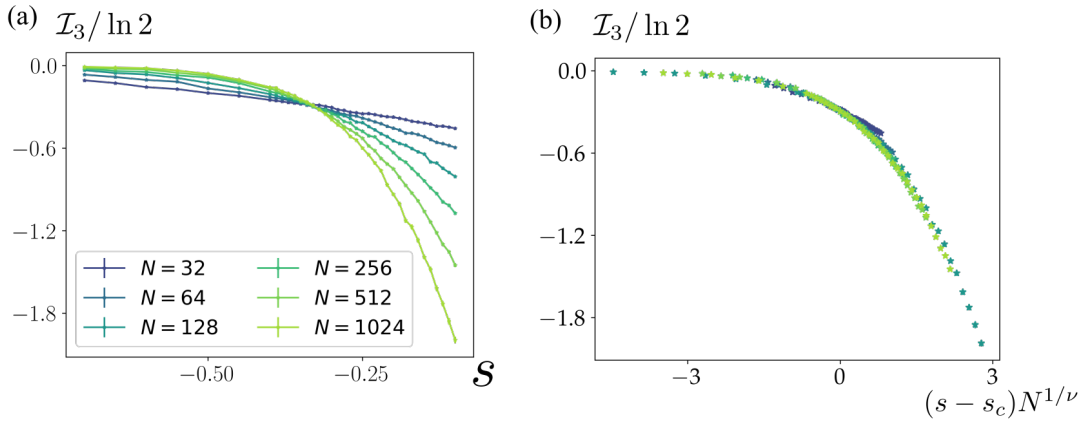

Figure 6.3: **Onset of Scrambling in PWR2 Model** (a). Tripartite mutual information I_3 between three regions A, B, and C as a function of the tunable parameter s for various systems sizes $N = 32, \ldots, 1024$ (see legend in (a) for colours and markers). (b). Scaling collapse of I_3 gives $\nu = 2.78 \quad 0.514$ and $s_c = \quad 0.33$. The numerical results are obtained by averaging over 5000 random circuit realisations. Error bars are shown or are smaller than datapoints. This figure was reproduced from [44].

consist of one even and odd block so that, on average, one gate is applied at each time step t. We observe the dynamical transition marking the onset of scrambling by plotting tripartite mutual information I_3 given in Eq. (6.4) as a function of the tunable parameter s for various system sizes $N = 32, 64, \ldots, 1024$ at $t = 1$, shown in Fig. 6.3(a). We also estimate the critical point $s_c = \quad 0.33$ and the corresponding critical exponent $\nu = 2.78 \quad 0.514$ by using the finite size scaling analysis given in Eq. (6.6), and this is shown in Fig. 6.3(b).

6.3 Analytical Study of Transition Dynamics

In Sec. 6.2.1, and Sec. 6.2.2, the onset of scrambling as a dynamical transition has been numerically investigated in both dense and sparse models. Due to the classical simulability of Clifford circuits as mentioned in Sec. 4.1.1, larger system sizes are accessible, thus allowing us to emulate the thermodynamic limit. To support our numerical analysis, it is crucial to obtain an analytical understanding of this transition, and to achieve this, we use a closely related Brownian circuit model, the entanglement properties of which can be calculated using path integral techniques [20, 132, 238–244]. These mod-

els have been extensively studied on the grounds of entanglement phase diagrams, and measurement-induced phase transitions [243, 244]. Here, we show that for a certain choice of parameters, the dynamics of this model can be mapped onto a long-range Ising model, the ordering transition of which is well understood [245–247].

6.3.1 Brownian Circuit Model

For any given WrAA model, we construct a related Brownian circuit that acts on N clusters of M spins arranged in 1 dimension as shown in Fig. 6.4(a), where $i, j = 0, \ldots, N - 1$ label the clusters and $u, v = 0, \ldots, M - 1$ label the spins $\vec{S}_{iu} = S^{\alpha}_{iu}$ within each cluster where $\alpha = x, y, z$. During each timestep dt, the system evolves under the unitary $U_t = e^{-iH_{\mathrm{BC}}(t)dt}$, generated by the Hamiltonian

$$H_{\mathrm{BC}} = J^{\alpha\beta}_{uv}(t) S^{\alpha}_{iu} S^{\beta}_{iv} + K^{\alpha\beta}_{iu,jv}(t) S^{\alpha}_{iu} S^{\beta}_{jv}, \tag{6.7}$$

where repeated indices are implicitly summed over. Here, the Brownian couplings $J^{\alpha\beta}_{uv}(t)$ generate intra-cluster interactions, while the couplings $K^{\alpha\beta}_{iu,jv}(t)$ generate inter-cluster interactions. These couplings are white-noise variables with zero mean and variance given by

$$\overline{J^{\alpha\beta}_{uv}(t) J^{\alpha'\beta'}_{u'v'}(t')} = \frac{J}{Mdt}(1 - b)\,\delta^{\alpha\alpha'}\delta^{\beta\beta'}\delta_{uu'}\delta_{vv'}\delta_{tt'}, \tag{6.8}$$

and

$$\overline{K^{\alpha\beta}_{iu,jv}(t) K^{\alpha'\beta'}_{i'u',j'v'}(t')} = \frac{J}{Mdt} b A_{ij}\,\delta^{\alpha\alpha'}\delta^{\beta\beta'}\delta_{ii'}\delta_{uu'}\delta_{tt'}. \tag{6.9}$$

Here, J controls the overall coupling strength, $0 \leq b \leq 1$ controls the ratio of the intra-cluster and inter-cluster couplings, $A_{ij} = A_{ji} = A_{|i-j|}$ is the normalised inter-cluster coupling matrix which falls off as a power law with exponent s, and the factor of M is necessary to ensure that the instantaneous Hamiltonian $H_{\mathrm{BC}}(t)$ is extensive. The full evolution over a total time t is given by the unitary matrix $U = \prod_0^t U_t$, and we work in the limit of $dt \to 0$ with Jt fixed. We also take the limit $M \to \infty$, with the model therefore completely controlled by the coupling matrix A_{ij}, the chain length N, and the parameter b.

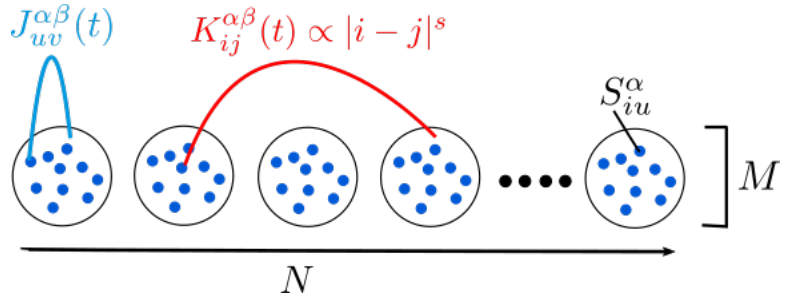

Figure 6.4: **Illustration Showing an Associated Brownian Circuit Model.** The Brownian circuit model consists of N clusters with M spins in each cluster. Here, $i, j = 0, \ldots, N - 1$ label the clusters and $u, v = 0, \ldots, M - 1$ label the spins $\vec{S}_{iu} = S_{iu}^{\alpha}$ within each cluster where $\alpha = x, y, z$. The Brownian couplings $J_{uv}^{\alpha\beta}(t)$ generate intra-cluster interactions while the couplings $K_{iu,jv}^{\alpha\beta}(t)$ generate inter-cluster interactions. These are white noise variables with zero mean and variance given in Eq. (6.8) and Eq. (6.9).

6.3.2 Calculating the Second-Order Rényi Entropy

Calculating the tripartite mutual information I_3, requires finding the bi-partite entanglement entropies S_A, S_B, S_{AB} etc. as given in Eq. (6.4). The second-order Rényi entropy of a subregion A can be written as

$$S_A^{n=2} = -\log \mathrm{Tr}\left[\rho_A^2\right], \tag{6.10}$$

and hence

$$e^{-S_A} = \mathrm{Tr}[\rho_A \rho_A] = \langle \rho_A \rangle. \tag{6.11}$$

This is equivalent to introducing two copies of the system and measuring the expectation value of the SWAP operator ('doing a SWAP test') on the region A [248, 249]. This is because of a simple proof shown in [248, 249], where

$$\begin{aligned}
\mathrm{Tr}[\mathrm{SWAP}\,\rho_1 \quad \rho_2] &= \mathrm{Tr}\left[\mathrm{SWAP} \sum_{aba'b'} \rho_{ab}^{(1)} \rho_{a'b'}^{(2)} |a\rangle\langle b| \quad |a'\rangle\langle b'|\right], \\
&= \mathrm{Tr}\left[\sum_{aba'b'} \rho_{ab}^{(1)} \rho_{a'b'}^{(2)} |a'\rangle\langle b| \quad |a\rangle\langle b'|\right], \\
&= \sum_{aba'b'} \rho_{ab}^{(1)} \rho_{a'b'}^{(2)} \delta_{a'b} \delta_{ab'} = \sum_{aa'} \rho_{aa'}^{(1)} \rho_{a'a}^{(2)} = \mathrm{Tr}[\rho_1 \rho_2],
\end{aligned} \tag{6.12}$$

and if $\rho_1 = \rho_2 = \rho_A$ then $e^{-S_A} = \mathrm{Tr}[\rho_A \rho_A]$, representing the expectation value of the SWAP operator. We rewrite Eq. (6.12) as

$$S_A^{(2)} = -\log \mathrm{Tr}\left[(\mathrm{SWAP}_{A_1 A_2})\, U\rho_0 U^\dagger \otimes U\rho_0 U^\dagger\right], \tag{6.13}$$

where ρ_0 is the initial state, and A_1 and A_2 represents the regions that will be swapped. Moving to the path-integral language, we first use the Choi-Jamiołkowski isomorphism [250, 251] to convert the mixed-state dynamics on two copies of the system into pure-state dynamics on four copies. This isomorphism maps the two-copy density matrix $|\psi\rangle\langle\psi| \otimes |\psi'\rangle\langle\psi'|$ to the four-replica pure state $|\psi\rangle|\psi\rangle|\psi'\rangle|\psi'\rangle = |\rho\rangle\rangle$. Hence, Eq. (6.13) may then be expressed as

$$S_A^{(2)} = -\log\langle\langle \mathrm{SWAP}_{A_1 A_2} | U \otimes U^* \otimes U \otimes U^* | \rho_0 \rangle\rangle, \tag{6.14}$$

where

$$U^* = (i\sigma_y) U (-i\sigma_y) = \sigma_y U \sigma_y \tag{6.15}$$

is the time reversal of U. Complex conjugation alone is not enough for a given spin to transform correctly under time reversal ($\vec{S} \to -\vec{S}$)[1]. This is because it only reverses the y-component of spin, that is $(\sigma^x, \sigma^y, \sigma^z) \to (-\sigma^x, \sigma^y, -\sigma^z)$. Hence, to properly time-reverse a spin $1/2$ qubit, one must include conjugation by $i\sigma^y$. In particular, $(U_t)^* = e^{+iH(t)dt}$ because the Hamiltonian is quadratic in the spins. In this way, the Rényi entropy can be understood as a bulk propagator $U \otimes U^* \otimes U \otimes U^*$ connecting the initial state $|\rho_0\rangle\rangle = |\psi_0\rangle\rangle$ to the final state $|\mathrm{SWAP}_{A_1 A_2}\rangle\rangle = |\psi_T\rangle\rangle$ at a final time T. We label the four copies (or 'replicas') of the system by the indices $r, s = 1, 2, 3, 4$.

6.3.3 Disorder Averaging

We focus first on the dynamics of the bulk propagator and later consider the effects of the initial and final states. For simplicity, the disorder average is represented as $\langle . \rangle = \mathbb{E}$. Because the Brownian coefficients are uncorrelated in time, we may perform

[1] Spin is an intrinsic form of angular momentum

the disorder average independently at each timestep:

$$\mathsf{E}[U_t \quad U_t^\tau \quad U_t \quad U_t^\tau] = \mathsf{E}\left[e^{\ iH(t)dt} \quad e^{+iH(t)dt} \quad e^{\ iH(t)dt} \quad e^{+iH(t)dt}\right]. \tag{6.16}$$

Applying Eq. (6.8) and Eq. (6.9), this can be further simplified as

$$\begin{aligned}\mathsf{E}[\star] \quad 1 \quad & \frac{J}{Mdt}(1 \quad b)\sum_{r<s}(\ \ 1)^{r+s}\sum_i\left(\sum_u \vec{S}_{iu} \quad \vec{S}_{iu}\right)^2 dt^2 \\ & \frac{J}{Mdt}b\sum_{r<s}(\ \ 1)^{r+s}\sum_{ij}A_{ij}\left(\sum_u \vec{S}_{iu} \quad \vec{S}_{iu}\right)\left(\sum_v \vec{S}_{jv} \quad \vec{S}_{jv}\right)dt^2,\end{aligned} \tag{6.17}$$

where $\star = U_t \quad U_t^\tau \quad U_t \quad U_t^\tau$ is used to make the equation compact. We stack the timesteps together and find that the bulk propagator is governed by a quantum statistical mechanics model that has a Gibbs weight of $\exp(\ \ tH_{\text{eff}})$, and an effective Hamiltonian

$$H_{\text{eff}} = MJ\sum_{r<s}(\ \ 1)^{r+s}\left[(1 \quad b)\sum_i (G_i^{rs})^2 + b\sum_{ij}A_{ij}G_i^{rs}G_j^{rs}\right], \tag{6.18}$$

where

$$G_i^{rs} = \frac{1}{M}\sum_u \vec{S}_{iu}^r \quad \vec{S}_{iu}^s \tag{6.19}$$

are the mean fields on each cluster, and the total time t plays the role of inverse temperature. This can be understood as considering the expression $\exp(\ \ tH_{\text{eff}})$ as $\exp(\ \ \beta H_{\text{eff}})$, where β is the inverse of temperature.

6.3.3.1 Derivation of Bulk Propagator via Disorder Averaging

From here it is convenient to take up the path-integral representation

$$\langle\langle\psi_T|\exp(\ \ tH_{\text{eff}})|\psi_0\rangle\rangle = \int DF_i^{rs}DG_i^{rs}DS_{iu}^{r\alpha}\exp(\ \ MS), \tag{6.20}$$

with action

$$S = \int_0^t dt \left[J(1-b) \sum_{r<s} (-1)^{r+s} \sum_i (G_i^{rs})^2 + J b \sum_{r<s} (-1)^{r+s} \sum_{ij} A_{ij} G_i^{rs} G_j^{rs} \right. \\ \left. \sum_{r<s} \sum_i i F_i^{rs} \left(G_i^{rs} - \frac{1}{M} \sum_u \vec{S}_{iu}^r \cdot \vec{S}_{iu}^s \right) \right], \tag{6.21}$$

where we have introduced Lagrange multipliers iF_i^{rs} to enforce the mean-field constraint [44, 243, 244]. Here, the mean fields G_i^{rs}, Lagrange multipliers F_i^{rs}, and spin variables $S_{iu}^{\alpha,r}$ are all functions of Euclidean time t, and the spin variables satisfy the boundary conditions imposed by $|\psi_0\rangle\langle\langle$ and $|\psi_T\rangle\rangle$. From here, the main idea will be to isolate the spin terms in the action so that we can create a propagator term for spin clusters that connects the initial state $|\psi_0\rangle\langle\langle$ to the final state $|\psi_T\rangle\rangle$. In Eq. (6.20), and Eq. (6.21), we have incorporated the kinetic term for the spin variables in the integration factor $\int DS^\alpha$. Now that the spins have been isolated to a single term it is convenient to separate them from the rest of the action, so we write

$$S = \int_0^t dt \left[J \sum_{r<s} (-1)^{r+s} \sum_{ij} \chi_{ij} G_i^{rs} G_j^{rs} - \sum_{r<s} \sum_i i F_i^{rs} G_i^{rs} \right] - \sum_i \log K_i, \tag{6.22}$$

where

$$K_i := \int DS^{\alpha,r} \exp\left(- \int_0^t dt \sum_{r<s} i F_i^{rs} \vec{S}^r \cdot \vec{S}^s \right) \\ = \langle\langle \psi_T | \prod_t \exp\left(- \sum_{r<s} i F_i^{rs}(t) \vec{S}^r \cdot \vec{S}^s \right) | \psi_0 \rangle\rangle \tag{6.23}$$

is the propagator for a single spin cluster under the mean field Lagrange multiplier iF_i^{rs}, and

$$\chi_{ij} := (1-b)\delta_{ij} + b A_{ij}, \tag{6.24}$$

where we have assumed that A_{ij} is translation invariant, symmetric, and normalised.

6.3.4 Mapping to Long-Range Ising Model

We now consider the limit $Jt \gg 1 \gg b$ and show that the dynamics of the effective Hamiltonian in this regime is equivalent to a long-range Ising model. The propagator K_i is simply the quantum mechanics of 4 spins $r, s = 1, 2, 3, 4$ in the external fields $F_i^{rs}(t)$. The factors $-i\sigma_y$ introduced in U^τ creates the singlet state:

$$\frac{1}{\sqrt{2}}(I \otimes i\sigma_y)(|00\rangle + |11\rangle)_{rs} = \frac{1}{\sqrt{2}}(|01\rangle - |10\rangle) = |(rs)\rangle . \tag{6.25}$$

Here, $|(rs)\rangle$ denotes a spin-singlet state between replicas r, s. The spin-singlet is antisymmetric under replica exchange $|(rs)\rangle = -|(sr)\rangle$, and the final state is $|(14)(32)\rangle$ due to the SWAP operator as shown in Fig. 6.5(a).

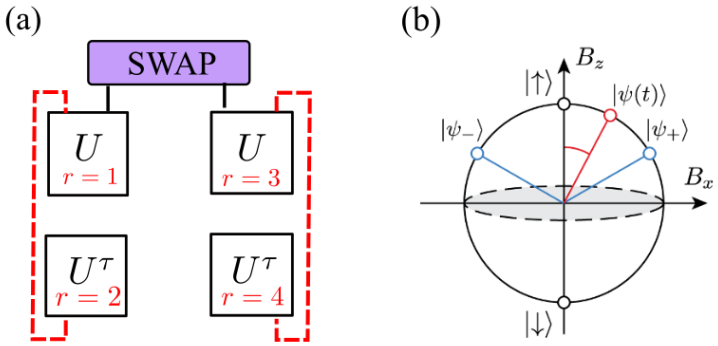

Figure 6.5: **Mapping the Brownian Circuit Model to a Long Range Ising Model** (a). The calculation of the second-order Rényi entropy can be mapped to the pure-state dynamics of a 4-replica system due to Choi-Jamiołkowski isomorphism. Red dashed lines represent the initial boundary conditions, and at the final time, we have the swapped boundary conditions. (b). The effective spin-1/2 particle governing the propagator K_i can be visualized as a time-dependent state $|\psi(t)\rangle$ (red) on a Bloch sphere spanned by the basis vectors $|"\rangle, |\#\rangle$. The saddle-point solutions (blue) are the vectors $\psi = \frac{\sqrt{3}}{2}|"\rangle - \frac{1}{2}|\#\rangle$

The single spin cluster propagator between different replicas as shown in Eq. (6.23) has coupling of the form $\vec{S}^r \cdot \vec{S}^s$, thereby conserving the total spin $\vec{S}_{\text{Tot}} = \sum_r \vec{S}^r$. The entire dynamics are therefore restricted to the singlet $S^2_{\text{Tot}} = 0$ subspace. Furthermore, we apply the method introduced in [243, 244] to create the basis vector that spans the

subspace (see Appendix A for further details)

$$
\begin{aligned}
|''i &= \frac{1}{2\sqrt{3}}\left(2|1010i + 2|0101i \quad |0011i \quad |1100i \quad |1001i \quad |0110i\right), \\
|\#i &= \frac{1}{2}\left(|0011i + |1100i \quad |1001i \quad |0110i\right).
\end{aligned} \tag{6.26}
$$

Thus, each propagator can be written as the dynamics of a spin-1/2 particle in a time-dependent magnetic field:

$$
K_i = \langle\psi_T| \exp\left\{\left[\frac{1}{2}\int_0^t dt\ \vec{B}_i(t) \quad \vec{\sigma}\right]\right\} |\psi_0\rangle\, e^{B_i^0 t/2}. \tag{6.27}
$$

The presence of the $.\vec{\sigma}$ in Eq. (6.27) reflects that we are in the subspace generated by two basis vectors, with any matrix $A \ 2 \ M_2$ (any $2 \quad 2$ matrix) decomposable to normalised Pauli matrices as they form an orthogonal basis. It follows that the magnetic field variables are effectively responsible for guiding the non-trivial dynamics taking place in the bulk to satisfy the non-equal boundary conditions $|\psi_0\rangle$, $|\psi_T\rangle$. Therefore, for $\left|\vec{B}\right| t \quad 1$, the boundary conditions do not control what happens in bulk, and the magnetic field variables will be strongly time-independent in bulk and strongly time-dependent near $t = 0, T$. Using block diagonalization, the values of different components of the time-dependent magnetic field are

$$
\begin{aligned}
B_i^x &= \frac{\sqrt{3}}{2}\left(iF_i^{12} + iF_i^{34} \quad iF_i^{14} \quad iF_i^{23}\right), \\
B_i^y &= 0, \\
B_i^z &= \frac{1}{2}\sum_{r<s} iF_i^{rs} \quad \frac{3}{2}\left(iF_i^{13} + iF_i^{24}\right), \\
B_i^0 &= \frac{1}{2}\sum_{r<s} iF_i^{rs}.
\end{aligned} \tag{6.28}
$$

Since the bulk dynamics are time-independent, so

$$
K_i \quad ce^{\left|\vec{B}_i\right| t/2} e^{B_i^0 t/2}, \tag{6.29}
$$

where the constant factor c comes from the overlap of the initial state with the spin singlet subspace basis vectors $|"\rangle, |\#\rangle$. Therefore, our action simplifies to:

$$S = Jt\sum_{r<s}(-1)^{r+s}\sum_{ij}\chi_{ij}G_i^{rs}G_j^{rs} - \sum_{r<s}\sum_i iF_i^{rs}G_i^{rs}t - \sum_i\left(\left|\vec{B}_i\right| + B_i^0\right)t/2. \quad (6.30)$$

The final step is to find the saddle points of this action by taking derivatives $\partial S/\partial G = \partial S/\partial F = 0$ with respect to the fields F, G, yielding the following conditions

$$iF_i^{rs} = 2J(-1)^{r+s}\sum_j \chi_{ij}G_j^{rs}, \quad (6.31)$$

and

$$G_i^{rs} = \frac{1}{2}\frac{\partial}{\partial iF_i^{rs}}\left(\left|\vec{B}_i\right| + B_i^0\right). \quad (6.32)$$

The antisymmetric combinations $iF_i^{12} - iF_i^{34}, iF_i^{14} - iF_i^{23}, iF_i^{13} - iF_i^{24} = 0$ vanish [2], and we introduce the symmetric combinations

$$\phi_i^a = iF_i^{12} + iF_i^{34}, \quad (6.33)$$

$$\phi_i^b = iF_i^{14} + iF_i^{23}, \quad (6.34)$$

$$\phi_i^c = iF_i^{13} + iF_i^{24}. \quad (6.35)$$

[2] One may check this by putting in the values for r, s in Eq. (6.31) and applying $G_i^{12} = G_i^{34}, G_i^{14} = G_i^{23}, G_i^{13} = G_i^{24}$

This simplifies the equations of motion to

$$\phi_i^a = 2J \sum_j \chi_{ij} \left(\frac{\partial \left| \vec{B}_j \right|}{\partial \phi_j^a} + \frac{1}{2} \right) = J \sum_j \chi_{ij} \left(\frac{1}{\left| \vec{B}_j \right|} \left(2\phi_j^a \quad \phi_j^b \quad \phi_j^c \right) + 1 \right), \tag{6.36}$$

$$\phi_i^b = 2J \sum_j \chi_{ij} \left(\frac{\partial \left| \vec{B}_j \right|}{\partial \phi_j^b} + \frac{1}{2} \right) = J \sum_j \chi_{ij} \left(\frac{1}{\left| \vec{B}_j \right|} \left(\phi_j^a + 2\phi_j^b \quad \phi_j^c \right) + 1 \right), \tag{6.37}$$

$$\phi_i^c = 2J \sum_j \chi_{ij} \left(\frac{\partial \left| \vec{B}_j \right|}{\partial \phi_j^c} + \frac{1}{2} \right) = J \sum_j \chi_{ij} \left(\frac{1}{\left| \vec{B}_j \right|} \left(\phi_j^a \quad \phi_j^b + 2\phi_j^c \right) + 1 \right). \tag{6.38}$$

Eq. (6.36), Eq. (6.37), and Eq. (6.38) are solved for a small value of b focusing on the lowest-order approximation. We evaluate the quantities $\left| \vec{B}_i \right| = 3J + O(b)$ and the linear combination

$$\phi_i^a + \phi_i^b \quad \phi_i^c = 3J \sum_j \chi_{ij} = 3J \quad 3bJ \sum_j (\delta_{ij} \quad A_{ij}). \tag{6.39}$$

Substituting this into Eq. (6.38), we conclude that ϕ_i^c vanishes at lowest order $\phi_i^c = 0 + O(b)$. Finally, we substitute $\phi_i^a + \phi_i^b = 3J + O(b)$ into $\left| \vec{B}_i \right| = 3J + O(b)$ to solve for

$$\phi_i^a \quad \phi_i^b = 3J + O(b). \tag{6.40}$$

Thus, we find exactly two saddle points $j\psi \quad i$ (See Fig. 6.5 (c)) for each cluster i, which we label with an Ising spin $\sigma_i = 1$. In the spin-1/2 replica subspace, these states are written as

$$j\psi \quad i = \frac{p\overline{3}}{2} j''i \quad \frac{1}{2} j\#i. \tag{6.41}$$

When $\sigma_i = +1$ we find that $G_i^{12} = G_i^{34} = 3/4 + O(b)$ with all other fields vanishing, while for $\sigma_i = 1$ we find that $G_i^{14} = G_i^{23} = 3/4 + O(b)$ with all other fields vanishing (see Appendix A). Applying these saddle-point solutions back into Eq. (6.18), we find

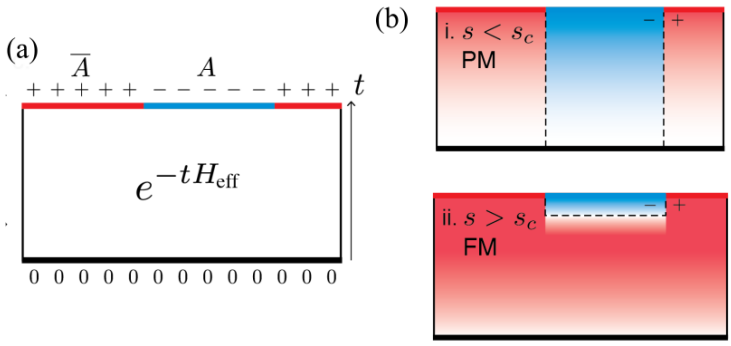

Figure 6.6: **Onset of Scrambling as a Domain-Wall Depinning Transition in a Brownian Quantum Circuit** (a). Averaging over the Brownian couplings $J_{uv}^{\alpha\beta}(t), K_{iu,jv}^{\alpha\beta}(t)$ and taking the large cluster size limit $M \; ! \; 1$ maps the calculation of the Rényi entropy $S_A^{(2)}$ of a subregion A onto a quantum statistical mechanics problem with effective Hamiltonian H_{eff} and exactly two saddle point solutions $j\psi \;\; i$ (red, blue). For short-range interactions $s < s_c$ ((b).i.), the system is in a paramagnetic (PM) phase where it is energetically favorable to form vertical domain walls ((b).i., dotted black) that are pinned to the bottom of the circuit. For $s > s_c$ ((b).ii.), the system is in the ferromagnetic (FM) phase where vertical domain walls are energetically expensive and it is, therefore, favorable to form a horizontal domain wall ((b).ii., dotted black) that is 'depinned' from the bottom boundary. This figure was reproduced from [44].

that the bulk dynamics are

$$\exp(\;\; tH_{\text{eff}}) \quad \sum_{f\sigma_i = \;\; 1g} e^{\;\; tH[\sigma]}, \tag{6.42}$$

where

$$H[\sigma] = J \sum_{ij} \chi_{ij} (3/4)^2 \, (\sigma_i \sigma_j + 1) \, . \tag{6.43}$$

χ_{ij} may be expressed in terms of A_{ij} by using Eq. (6.24). Apart from additive constants, this is simply a long-range Ising model with coupling matrix χ_{ij}. To get the true action, in principle, we ought to expand to higher powers of b, but doing so will not change the number of saddle-point solutions, it will only modify the energy of the effective Ising model.

6.3.5 Transition in Tripartite Mutual Information

In this framework, the transition in the tripartite mutual information I_3 can be viewed as an ordering transition in the statistical mechanics model H_{eff} as illustrated in Fig. 6.6 (a). When $s < s_c$, the interactions are short-range and are not strong enough to stabilise a ferromagnetic phase (FM). Consequently, the bulk remains in a paramagnetic (PM) phase, and the free energy is dominated by vertical domain walls that extend directly downward from region A and are pinned to the bottom edge of the circuit, as shown in dotted black in Fig. 6.6(b).i. As a result, we find that $S_A^{(2)} = 2g(t,s)$, a function dependent only on time t and exponent s, and independent of the subregion size $|A|$, such that $I_3 = 0$.

Conversely, for sufficiently large $s > s_c$, long-range couplings increase the cost of vertical domain walls and, in this regime, the bulk quickly settles into $|\psi_+\rangle$ favored by the majority boundary region $\overline{A}$, while the boundary condition $|\psi\rangle$ on region A induces a horizontal domain wall (dotted black) that is depinned from the bottom edge. In this case, the entanglement entropy follows a volume law $S_A^{(2)} = k|A|$ for some constant k, and correspondingly negative tripartite mutual information $I_3 < 0$. The transition between these two regimes occurs when the bulk undergoes a transition between the paramagnetic and ferromagnetic phases.

Therefore, I_3 reveals a domain-wall depinning transition in the Brownian circuit driven by an ordering transition in H_{eff}. I_3 is effective at diagnosing this transition because the contributions from vertical domain walls separating neighbouring regions cancel out (Fig. 6.6(b)i., dotted black), while contributions from horizontal domain walls do not cancel [105]. Hence, $I_3 = 0$ unless a horizontal domain wall (Fig. 6.6(b)ii., dotted black) has depinned from the bottom edge. For sufficiently long-range interactions $s > s_c$, the tripartite mutual information becomes negative precisely because a depinned domain wall separates the input and output of the circuit. The critical exponents of the long-range Ising model are known to be mean-field and numerically agree with the critical exponents we find in our Clifford simulations, suggesting that the transition in question

is itself mean field. Specifically, the mean-field critical exponent for the long-range Ising model predicted in [246] is, in terms of our parameters, $\nu = 1/(1 + s_c) \quad 3$, which agrees with our Clifford results with a difference of about 7%.

6.4 Towards Experimental Observation

Having explored the onset of scrambling numerically in both dense and sparse models, along with an analytical Brownian circuit model, it is interesting to ask whether this transition can be observed in experiments. Tunable power-law interactions are naturally accessible in trapped ion experiments, and the tripartite mutual information may be measured in principle by interfering many-body twins [248, 249] or by performing randomized measurements [252, 253]. Here, we pursue a slightly different approach and ask whether the same phenomena appears in systems with sparse interactions that can be engineered in ensembles of Rydberg atoms with optical tweezers.

Building on ideas proposed in [35], we demonstrate that the transition studied in Sec. 6.2 may be observed in near-term experiments using optically trapped Rydberg atoms [72, 73, 254, 255]. Nonlocal couplings in the system are generated by a quasi-1D shuffling process employing optical tweezers that rearrange atomic positions [53, 237, 256–258]. Each rearrangement executes a "Faro Shuffle", moving the atom originally located at lattice site i to lattice site i' according to the map [259, 260]

$$i' = R(i = b_m ... b_2 b_1) = b_1 b_m ... b_2. \tag{6.44}$$

This nonlocal mapping permutes the bit order of the atomic index $i = b_m ... b_2 b_1$, written in binary such that the least significant bit b_1 of i becomes the most significant bit of $i' = R(i)$. This operation creates a sparse coupling geometry that resembles a $m = \log_2(N)$ hypercube which has been studied recently extensively in neutral atom array platforms [35, 53].

A proposal to perform a "Faro Shuffle" begins with N atoms (represented by blue and

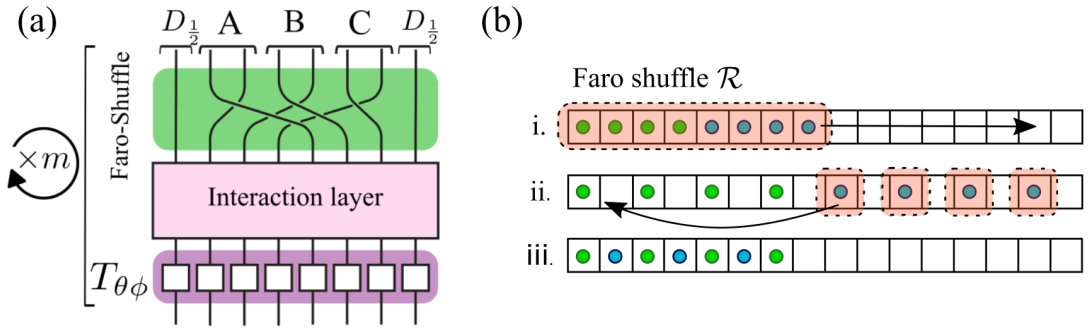

Figure 6.7: **Illustrations Showing Proposed Experimental Implementation of the Dynamical Transition** (a). Our circuit implementation is composed of inverse Faro-shuffles (green), global rotations (purple), and an interaction layer (pink). Based on the iteration, the interaction layer will be composed of weighted CZ^{w}_{even} or CZ^{w}_{odd} gates. Each time step t is composed of $m = \log_2 N$ even and $m = \log_2 N$ odd iterations. (b) A schematic diagram to illustrate Faro-shuffling operations (green layer in Fig. 6.7(a)) in neutral atom arrays using optical tweezers. It starts with N atoms labeled $i = 0, 1, ...N - 1$ on a 1D lattice with spacing a. Using an auxiliary 1D tweezer array, atoms are adiabatically relocated, with the left half recaptured by the lattice and the right half shifted leftwards and back into the trap, resulting in permutation $i' = R(i)$. The inverse process reverses these steps.

green dots in Fig. 6.7(b)) labeled $i = 0, 1, \ldots, N - 1$ initially trapped at sites $x(i) = ia$ of a fixed 1D lattice (black boxes in Fig. 6.7(b)) with spacing a. An additional N empty sites $x = Na, \ldots, (2N - 1)a$ are reserved. Using an auxiliary 1D tweezer array superimposed on the fixed lattice to capture all N atoms, an adiabatic row-stretch operation is conducted that relocates atoms at site x to site $2x$ (Fig. 6.7(b)(i)). The first $N/2$ tweezers are then switched off, causing the atoms in the left half of the cloud (Fig. 6.7(b)(ii), green dots) to be recaptured by the fixed 1D lattice. The remaining $N/2$ tweezers then adiabatically transport the atoms in the right half of the cloud (Fig. 6.7(b)(ii), blue dots) below the trap array, shifting them leftward by a distance $x = (N - 1)a$, and back into the trap. When the tweezer array is switched off, the atoms i are rearranged in the linear trap according to the permutation $i' = R(i)$ (Fig. 6.7(b)(iii)).

Repeated shuffling operations lead to a dramatic rearrangement of the atomic positions, and the resulting nonlocal couplings can rapidly generate many-body entanglement. The coupling operations in the circuit occur in the interaction layer, shown

in Fig. 6.7(a), and are achieved using stochastically applied alternating even and odd layers of Controlled-Z (CZ) gates. Combining this, along with global rotations, we implement a strong scrambling circuit (sc)

$$D_{\mathrm{sc}} = E_{\mathrm{sc}}^{m} O_{\mathrm{sc}}^{m}, \tag{6.45}$$

where
$$E_{\mathrm{sc}} = [R \;{}^{1}\mathrm{CZ}_{\mathrm{even}}^{w} \mathrm{T}_{\theta\phi}], \tag{6.46}$$

and
$$O_{\mathrm{sc}} = [R \;{}^{1}\mathrm{CZ}_{\mathrm{odd}}^{w} \mathrm{T}_{\theta\phi}] \tag{6.47}$$

are the even and odd circuit iterations respectively, with $\mathrm{T}_{\theta\phi} = \mathrm{HP}$, a combination of global Hadamard H and phase gates P. Please refer to Sec. 5.3 for definitions of the even and odd circuit iterations. The weighted CZ_{even}^{w} and CZ_{odd}^{w} gates couple qubits $i < j$ with probability $p(d, s)$ given by

$$p(d, s) = J_{D_s} d^{s}. \tag{6.48}$$

The normalisation factor J_{D_s} ensures that one gate, on average, is applied per site during each timestep t. In our sparse coupling circuit, this is achieved after $m = \log_2 N$ even (Eq. (6.46)) and $m = \log_2 N$ odd circuit iterations (Eq. (6.47)) . One even circuit iteration E_{sc} is composed of globally applied $\mathrm{T}_{\theta\phi}$, followed by a stochastic random application of CZ_{even}^{w} gates and a "Faro Shuffle" as illustrated in Fig. 6.7(a). The same procedure applies to one odd circuit iteration O_{sc}. To experimentally realise this circuit, we propose using the long-lived ground states $|0\rangle$ and $|1\rangle$ of neutral atoms as qubit states. In each of the constituting even E_{sc} and odd O_{sc} circuit iteration, the implementation of Hadamard and Phase gates may be achieved by single-qubit rotations. For the entangling operations, pairs of qubits i and j are randomly sampled according to the probability distribution in Eq. (6.48). The chosen qubits, of corresponding atomic indices $i^{0} = R_{l}^{\;1}(i)$ and $j^{0} = R_{l}^{\;1}(j)$ where l represents the number of inverse shuffle operations, are then entangled using CZ gates. These CZ gates are realised by exciting the state $|1\rangle$ to a Rydberg state, and utilizing the strong van der Waals interactions [54, 55, 261–266]. Further, we observe the dynamical transition in Fig. 6.8(a) characterised by the negativity of the tripartite mutual information I_3 of three contiguous

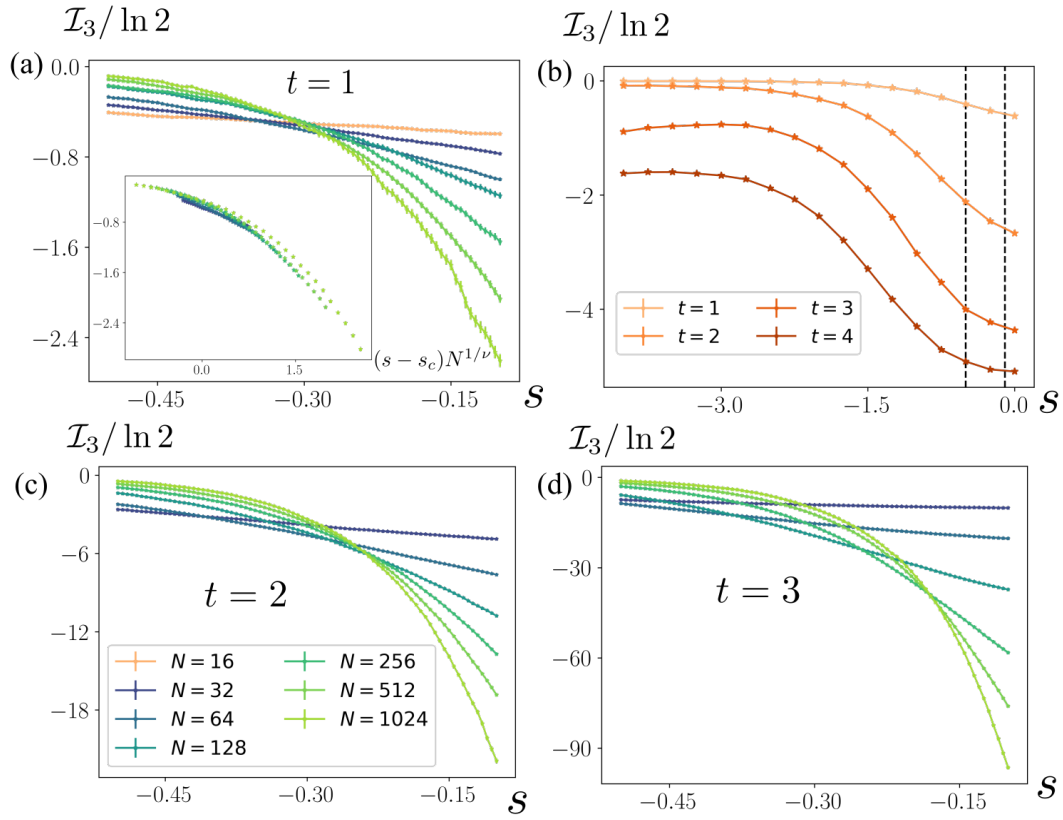

Figure 6.8: **Onset of Scrambling in a Deterministic Circuit with a Random Initial State** (a). Tripartite mutual information (I_3) between three regions A, B, and C in the bulk as a function of the tunable parameter s for various systems sizes $N = 32, 64, \ldots, 1024$. This transition is observed for system sizes as small as $N = 16$ (orange) at $t = 1$. (inset) Scaling collapse of I_3 gives $\nu = 2.79 \quad 0.39$ and $s_c = \quad 0.29$. (b) I_3 between three regions A, B, and C as a function of the tunable parameter s for $N = 16$ for different values of time steps t (light to dark orange). Black dotted vertical lines highlight the window over which I_3 is plotted as a function of s in (a). I_3 is further plotted as a function of s for various system sizes $N = 32, ..512$ for (c) $t = 2$ and (d) $t = 3$. The numerical results are averaged over 3000 random circuit realisations. Error bars are shown or are smaller than datapoints. This figure was reproduced from [44].

regions A, B, and C across system sizes $N = 16, 32, 64, \ldots, 1024$, at a fixed time step $t = 1$ initialised in a completely random state. The three contiguous regions A, B, and C of the output set of qubits are chosen in the bulk as shown in Fig. 6.7(a) to avoid any boundary effects on the calculations. A random initial state is characterised by an arbitrary polarization (x, y or z) qubit state at each site. In an experimental setting, this may be prepared using classical random sampling and by rotating individual spins

that constitute the qubit state. We also perform finite-size scaling analysis for this model, with the scaling ansatz for I_3 giving $\nu = 2.79 \quad 0.39$ and $s_c = \quad 0.29$, shown in the inset of Fig. 6.8(a). Considering near-term experimental realisation, this transition is observable in system sizes as small as $N = 16$ and $N = 32$ for a deterministic initial state (say a single polarisation on all qubits), thereby avoiding individual addressing of the qubit states. We observe that larger system sizes exhibit noticeable error bars, as shown in Fig. 6.8(a). However, at $t = 1$, focusing on the experimental realizations for system sizes $N = 16$ and $N = 32$, the error bars appear relatively smaller. Additionally, calculating the standard deviation reveals that it remains small for $N = 16$ and $N = 32$. For $N = 16$, the value of I_3 is already negative for the range of s in Fig. 6.8(a). However, if we extend the range of s, we observe that for $N = 16$ the value of the I_3 transitions from positive to negative as shown in Fig. 6.8(b). This figure also demonstrates the variation in I_3 as a function of the tunable parameter s across different time steps t for $N = 16$. Furthermore, with increasing time step, the many-body entanglement generated in the system increases and is characterised by an appreciable negative value of I_3 as shown in Fig. 6.8(c) and Fig. 6.8(d) for $t = 2$ and $t = 3$, respectively. As t increases, the onset of scrambling as a transition is more evident only in larger system sizes. We also observe that as t increases, the error in larger system sizes tends to decrease, accompanied by a reduction in the standard deviation. This suggests that, with future advancements in experimental techniques and technology, increasing t could help ensure that a smaller number of samples is more likely to be representative of the mean behaviour. However, in the context of near-term experiments, our focus remains on system sizes $N = 16$ and $N = 32$, for which $t = 1$ is sufficient to achieve efficient generation of entangled states, using shallow depth circuits.

6.5 Continuous Time Models

In Sec. 6.2 and Sec. 6.4, we studied the onset of scrambling as a dynamical transition in gate-based models. However, in most experimental setups, the evolution occurs continuously, which motivates the exploration of this transition in continuous time models. To access this transition in larger system sizes, matrix product states (MPS)

and matrix product operator (MPO) techniques will be essential. The spin system that we investigate is inspired by [267, 268]. In discrete time models, we observed this transition through the tripartite mutual information I_3, leading to the natural question of whether the transition in continuous time models can also be characterised by this quantity. Therefore, we attempt to calculate I_3 using the method described in Sec. 4.2.4.2.

The model of interest is the one-dimensional chain of N spin 1/2 system described by the long-range transverse field Ising (LRTI) model

$$H_{\mathrm{LRTI}} = \sum_{ab}^{N} \chi_{ab} S_a^x S_b^x + B \sum_{i}^{N} S_a^z, \tag{6.49}$$

where χ_{ab} is the coupling strength between spins a, b, which resides on the vertices of a given coupling graph, B is the transverse field, and the spin operators in terms of Pauli operators are given by $S_i^\alpha = \sigma_i^\alpha/2$ ($\hbar = 1$), and $\alpha \in \{x, y, z\}$. In this section, we study the dynamics in the powers of two (PWR2) model with tunable range interactions controlled by s and periodic boundary conditions (see Sec. 5.3 and Sec. 6.2.2). The coupling strength χ_{ab} thereby follows

$$\chi_{ab,s} = \begin{cases} \chi_0 |a - b|^s & |a - b| = 2^m - 1 \\ 0 & \text{Otherwise,} \end{cases} \tag{6.50}$$

for $m = 1, \ldots, \log_2 N$. Our primary motivation for studying the quench dynamics in these spin models is their feasibility for experimental implementation in setups such as trapped ions [269] and neutral atom arrays [72, 255, 270, 271]. To study the dynamics, we start in an initial state that is z-polarized, specifically $|\#i^N$, and evolve using the Hamiltonian in Eq. (6.49). This corresponds to a global quench from $B = \infty$ to some finite value of the field $B = 1.0\chi_0$.

Here, we present results on the calculation of the tripartite mutual information I_3 for system sizes $N = 8, 16, 32$ for three different values of the tunable parameter

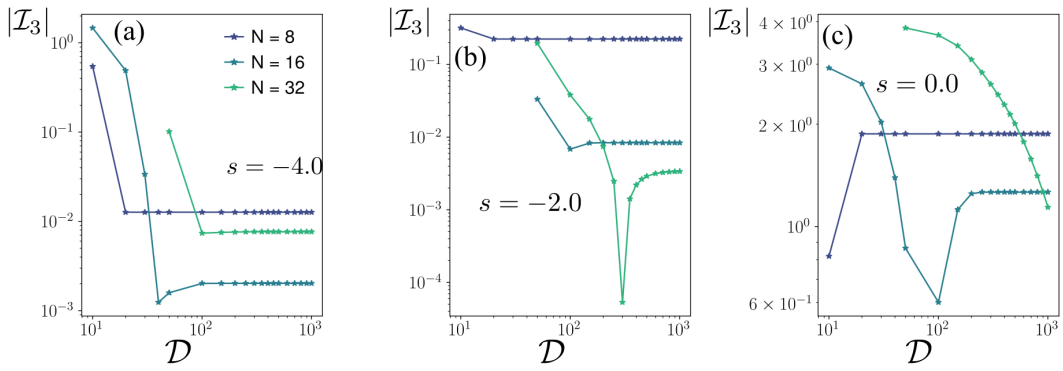

Figure 6.9: **Tripartite Mutual Information Using SWAP Operation.** Spins initially in an z-polarized state evolve under the Hamiltonian given in Eq. (6.49) up to a time $t = 1$. The absolute value of the tripartite mutual information $|I_3|$ is plotted as a function of the maximal bond dimension D for system sizes $N = 8, 16, 32$ (see legend in (a) for colours and markers). The technique used to calculate $|I_3|$ is by using the SWAP operation introduced in Sec. 4.2.4.2. In the case of (a) $s = -4.0$, $|I_3|$ appears to converge well with increasing bond dimension D. However, as s approaches 0 (b) and (c), I_3 struggles to converge even at higher D, particularly for larger system sizes, such as $N = 32$.

$s = -4.0, -2.0, 0.0$. In these preliminary results, we don't normalise the Hamiltonian, i.e., $\chi_0 = 1$, instead, we evolve the initial state up to a time $t = 1/\chi_0$. The analysis presented here demonstrates the difficulty in computing I_3 for larger system sizes using the SWAP operator introduced in Sec. 4.2.4.2. We calculate I_3 of the state at $t = 1/\chi_0$ as a function of the maximal bond dimension D, where, during time evolution and the SWAP operations, the bond dimensions of our MPS can never exceed D. This is illustrated in Fig. 6.9. When s is large and negative, the model is approximately the nearest neighbour model (NN) with short-range interactions. Thus, a lower D may be sufficient to calculate I_3 as demonstrated in Fig. 6.9(a). However, as $s \to 0$, the interactions become increasingly non-local. Even with a $D \sim O(10^3)$, the values of I_3 do not converge for $N = 32$, as shown in Fig. 6.9(b) and Fig. 6.9(c). One possible solution for this would be to use the principle of classical shadows, proposed in [272] to calculate the properties of the quantum state. We leave these more involved calculations for future work.

6.6 Conclusions

In Ch. 6, we studied a dynamical transition marking the onset of scrambling in both dense and sparse quantum circuit models as shown in Sec. 6.2. In circuits where short-range couplings dominate ($s < s_c$), scrambling is constrained by local Lieb-Robinson bounds, leading to slow scrambling behaviour. Beyond a critical interaction exponent $s > s_c$, these bounds were shown to break down such that information could be scrambled on a much faster timescale of $t \quad \log N$. In both cases, we diagnosed the presence of scrambling through the negativity of the tripartite information $I_3 < 0$. We also studied this transition analytically in Sec. 6.3 by showing that the dynamics of a related long-range Brownian model were mappable to the long-range Ising model in a particular regime. In particular, we also estimated the mean-field critical exponent and found it to agree with our Clifford-simulation results. Additionally, we also explored this transition in a model that may be realised in an ensemble of neutral atoms equipped with optical tweezers in Sec. 6.4. After analysing this transition using both an analytically tractable model and a numerically accessible digital circuit model, we attempted to apply MPS-MPO techniques to observe the same transition in a continuous-time model, as discussed in Sec. 6.5. However, we encountered computational challenges in this approach, and we leave the detailed calculations involved for future work.

Chapter 7

Sparse Coupling Graphs for Quantum Metrology

> What is much more likely is that the new way of seeing things will involve an imaginative leap that will astonish us.
>
> John Bell

7.1 Introduction

In Ch. 5 and Ch. 6, we analysed the efficient generation of entanglement in sparse coupling models. Entanglement, as established in Sec. 3.2.2, enhances the sensitivity of states for phase estimation, allowing us to surpass the standard quantum limit. Building on these insights, a natural next step is to investigate how the entanglement generated by these sparse coupling graphs can be utilised to create states relevant to quantum metrology. In this chapter, we address this question by demonstrating that the PWR2 coupling graph introduced in Sec. 5.3 and the hypercube coupling graph introduced in Sec. 6.4 can generate states exhibiting Heisenberg scaling in quantum Fisher information. These are the states that offer super classical limits in the estimation of an unknown parameter due to the presence of entanglement. We have already

discussed the versatility offered by the neutral atom platform equipped with optical tweezers in Sec. 1.4 and Sec. 6.4. This advantage has also been noted in recent tweezer-based clock platforms [162, 273–278]. Hence, we aim to leverage this platform to create entangled states that can be used as resource states for quantum-enhanced metrology.

The rest of the chapter is organised as follows: we begin by showing how the spin-exchange Hamiltonian in a sparse coupling graph may generate optimal states for quantum metrology in Sec. 7.2. We numerically demonstrate that specific sparse graphs featuring long-range interactions approximate the dynamics of all-to-all spin models like the one axis twisting model introduced in Sec. 3.4.1. We explain these results by analysing the spectral gap of the Hamiltonian of the sparse coupling graphs in Sec. 7.3. Finally, we show how the metrologically relevant states may be prepared in near-term experimental platforms in Sec. 7.4. We end this chapter by summarizing our findings in Sec. 7.5.

7.2 Dynamical Preparation of Metrologically Useful States

One axis twisting Hamiltonian (OAT) as mentioned in Sec. 3.4 is a well-studied model known for its relevance in metrology and spin squeezing which features uniform, infinite-range Ising interactions [8, 157, 279]. While this model may be engineered by collisional interactions between delocalized atoms [280, 281] and interactions mediated by coupling to phonons [82, 159] or cavity modes [60–62], this degree of connectivity is challenging to realise with direct interactions in most physical setups. This is where sparse coupling graphs with limited connectivity become useful. The specific Hamiltonian we study is the spin-exchange Hamiltonian given by:

$$H_{XY} = \sum_{a,b}^{N} \chi_{ab}(S_a^x S_b^x + S_a^y S_b^y), \tag{7.1}$$

where χ_{ab} is the coupling strength between spins a, b, which reside on the vertices of a given coupling graph, and the spin operators in terms of Pauli operators are given by $S_i^\alpha = \sigma_i^\alpha/2$ ($\hbar = 1$), and $\alpha \in \{x, y, z\}$. The reason for opting for the spin-exchange

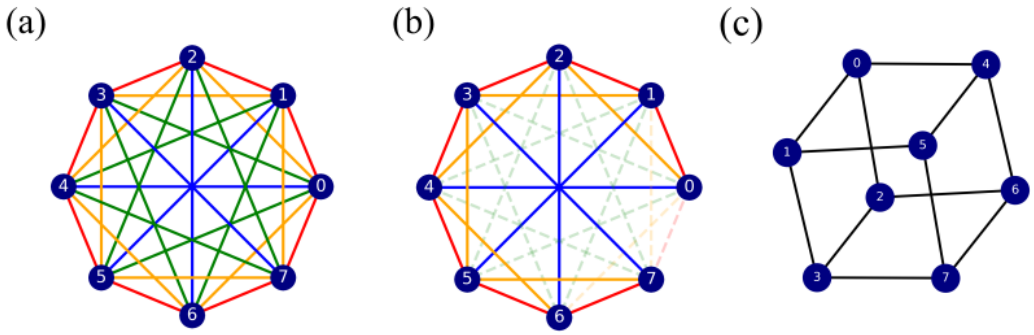

Figure 7.1: **Coupling Graphs** (a) An all-to-all coupling graph for $N = 8$ spins. (b). Removing certain edges (dashed) results in the sparse long-range PWR2 graph with open boundary conditions. (c). This is an illustration of a $m = 3$ dimensional hypercube.

Hamiltonian instead of the Ising Hamiltonian is that the non-uniform couplings in the Ising Hamiltonian, which arise due to sparse interactions, break the permutational symmetry discussed in Sec. 3.3.2. However, the spin-exchange Hamiltonian, as given in Eq. (7.1), preserves the collective spin behaviour. This will be explained further in Sec. 7.3, where we analyse the spectral gap of this Hamiltonian. For the case of a 1D chain (e.g., a nearest-neighbour coupling graph), this model has been extensively studied due to its integrability. However, integrability breaks down when considering sparse graphs like the *Powers of Two (PWR2)* coupling graph introduced in Sec. 5.3 and the *hypercube* coupling graph introduced in Sec. 6.4.

We compare and contrast these two sparse coupling models, with a dense all-to-all (A2A), see Fig. 7.1(a), and the nearest neighbour (NN) coupling geometry. In the PWR2, as mentioned in Sec. 5.3, the spins interact iff separated by a distance equivalent to a power of 2, and we consider open boundary conditions. The model's coupling graph has $E_G = N\log_2(N) - N + 1$ edges (see Fig. 7.1(b), where solid lines represent the edges of this graph) for N vertices. In contrast, for the hypercube coupling graph spins reside on the vertices of a $m = \log_2(N)$ dimensional hypercube, resulting in $E_G = \frac{N}{2}\log_2(N)$ edges for N vertices, as shown in Fig. 7.1(c), which illustrates a 3-dimensional hypercube.

We consider spins initially prepared in an x polarised state $|+\rangle^{N}$ and allow it to evolve under the XY Hamiltonian in Eq. (7.1). We normalise the time in such a way that we take into account the deficit of bonds in the sparse coupling graphs compared to the A2A coupling graph. The normalised time is written as

$$\bar{t} = t\frac{E_G}{E_{G,A2A}} , \tag{7.2}$$

where E_G is the number of edges in the sparse graph, and t is the physical time. For the A2A graph, $\chi_{ab} = \chi_0$ for $a \neq b$, thus recovering back the OAT Hamiltonian. This can be inferred by using the collective spin operators $\hat{J}_\alpha$, $\alpha = x, y, z$ discussed in Sec. 3.3, and by applying the following identity

$$\hat{J}_x^2 + \hat{J}_y^2 + \hat{J}_z^2 = \hat{J}^2 = J(J+1). \tag{7.3}$$

For the A2A graph, H_{XY} Hamiltonian in Eq. (7.1) hence can be expressed as:

$$H_{XY} = \chi_0 \left(\hat{J}_x^2 + \hat{J}_y^2\right) \quad \frac{\chi_0 N}{2}, \tag{7.4}$$

$$= \chi_0 \left(J(J+1) \quad \hat{J}_z^2\right) \quad \frac{\chi_0 N}{2}. \tag{7.5}$$

Thus, the OAT Hamiltonian is effectively recovered, up to a constant term. As mentioned in Sec. 3.2.2, the quantum Fisher information (QFI) describes the sensitivity of a given state $|\psi\rangle$ to a parameter θ. For spin systems, θ is encoded into the probe state through a small rotation around a given axis. The QFI for a pure state in such a scenario is

$$F_Q[\theta, J_\alpha] = 4(\quad \hat{J}_\alpha)^2 , \tag{7.6}$$

where $\hat{J}_\alpha$ is the generator of a rotation around axis α with $\alpha = x, y, z$, and $(\quad \hat{J}_\alpha)^2 = \langle \hat{J}_\alpha^2 \rangle \quad \langle \hat{J}_\alpha \rangle^2$ is its variance. The initial x polarised state $|+\rangle^{N}$ evolves under the XY Hamiltonian Eq. (7.1) and we calculate the QFI as a function of time for the coupling graphs shown in Fig. 7.1, along with the NN coupling graph. As illustrated in Fig. 7.2,

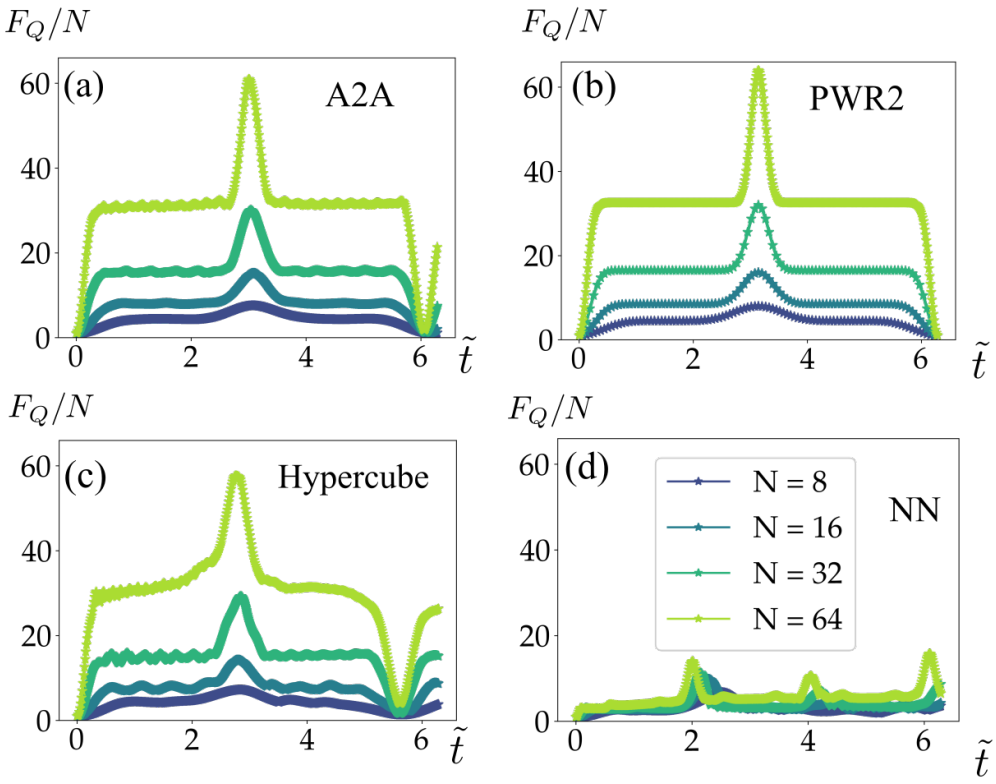

Figure 7.2: **Dynamics of the Quantum Fisher Information (QFI):** Spins initially in an x-polarised state evolve under the XY Hamiltonian given in Eq. (7.1). We plot the QFI F_Q/N as a function of normalised time $\tilde{t}$ according to Eq. (7.2) for (a) A2A, (b) PWR2, (c) hypercube, and (d) nearest neighbour (NN) geometry for system sizes $N = 8, 16, 32, 64$ (see legend in (d) for colours). The dynamics of the sparse coupling graphs PWR2 and hypercube closely resemble those of the A2A coupling graph, while the NN coupling graph exhibits a significantly lower QFI.

the dynamics of the QFI for the PWR2 (Fig. 7.2(b)), and hypercube coupling graph (Fig. 7.2(c)) are reminiscent of the dynamics of the A2A coupling graph, shown in Fig. 7.2(a). For all three coupling graphs, at $t \sim 1/\sqrt{N}$ there is an initial spin-squeezed region where the QFI rises steadily, followed by a plateau region, and a final rise to reach a state with maximum QFI, at $\tilde{t} \approx \pi$. We determine the Wineland squeezing parameter [9] given in Eq. (3.30) as a function of normalised time $\tilde{t}$, evolving the system up to $\tilde{t} = 1/\sqrt{N}$ for $N = 16$. Both the PWR2 and hypercube coupling graphs exhibit similar behaviour in terms of the squeezing parameter $\xi_R^2 < 1$, whereas the NN coupling graph shows significantly less squeezing as shown in Fig. 7.3(a). This implies that the states

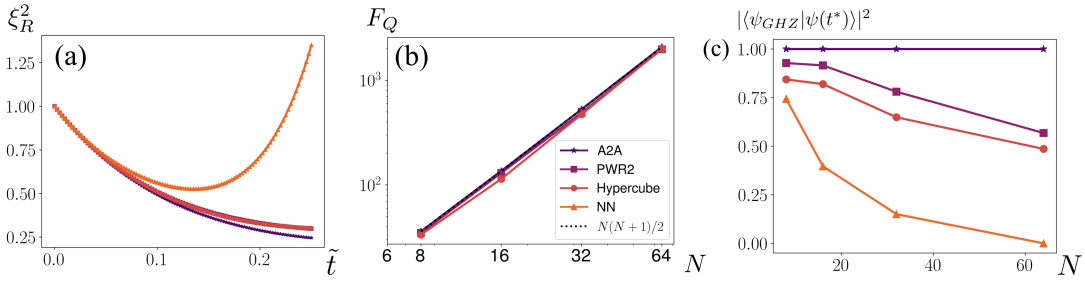

Figure 7.3: **Mimicking the All-to-All Dynamics.** (a). The Wineland squeezing parameter given in Eq. (3.30) is plotted as a function of the normalised time $\tilde{t}$ given in Eq. (7.2) for different coupling graphs for $N = 16$. Here, the system of spins initialised in an x-polarised state is evolved up to a final time $\tilde{t} = 1/\sqrt{N}$ under the XY Hamiltonian given in Eq. (7.1). We observe that the A2A, PWR2, and hypercube coupling graphs exhibit significant spin squeezing, with $\xi_R^2 < 1$. In contrast, the NN geometry exhibits spin squeezing initially, but quickly $\xi_R^2 > 1$ compared to other graphs. (b). The QFI of compass states is plotted as a function of different system sizes $N = 8, 16, 32, 64$. The A2A coupling graph creates states that have $F_Q = N(N+1)/2$. Both the PWR2 and hypercube also have similar scaling. The slopes for A2A, PWR2, and hypercube are 1.95, 1.93, and 1.97 respectively. The black dashed line indicates the value of $N(N+1)/2$ for different values of N. We exclude NN geometry in this analysis, due to the lack of distinct plateau as shown in Fig. 7.2(d). (c). The overlap of the state with maximum QFI $|\psi(t)\rangle$ with the GHZ state is plotted as a function of system sizes $N = 8, 16, 32, 64$ for different coupling graphs G. See legend in (b) for colours and markers.

generated by the sparse coupling graphs at $\chi_0 t \sim 1/\sqrt{N}$ are spin-squeezed similar to the OAT Hamiltonian as discussed in Sec. 3.4.1. Additionally, we also analyse the states on the plateau which are called as compass states. In Sec. 3.4.1, we discussed the dynamics of the OAT Hamiltonian, and we mentioned that these states have $F_Q = N(N+1)/2$. In Fig. 7.3(b), we compare F_Q of the compass states for different coupling graphs as a function of the system size. Since the dynamics of the NN geometry do not exhibit a distinct plateau, as shown in Fig. 7.2(d), we exclude it from the following analysis. The sparse graphs (PWR2 and hypercube) demonstrate the same scaling of F_Q with system size as the A2A coupling graph, indicating Heisenberg scaling. We also calculate the overlap of the states with maximum QFI $|\psi(t)\rangle$ created by different coupling graphs with the GHZ state. Here t is the physical time required to reach the state with maximum QFI. The choice of the GHZ state is due to the discussion in Sec. 3.4.1,

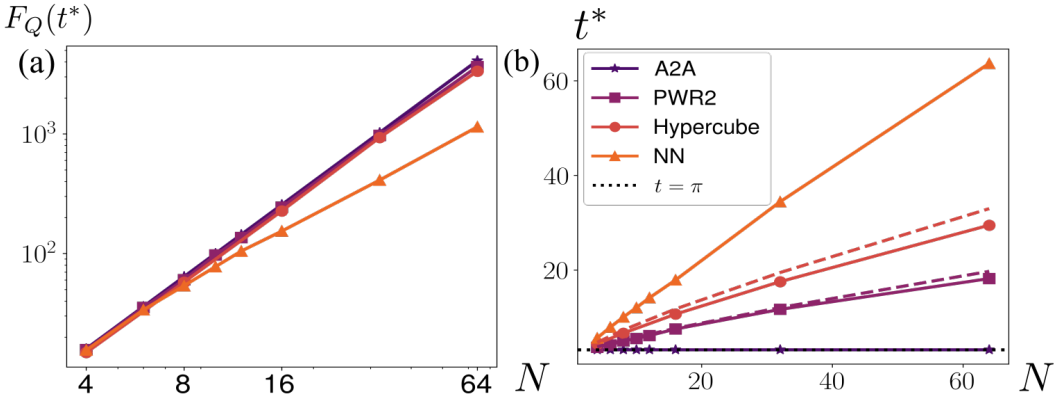

Figure 7.4: **Heisenberg Scaling and Emulating All-To-All Dynamics Using Sparse Graphs** (a) The maximum value of the QFI under the dynamics generated by the XY Hamiltonian in Eq. (7.1) on an initially x polarized state is shown as a function of the number of spins for different coupling graphs, see legend in (b). We extract the scaling coefficients for different coupling graphs and it is $\beta = 2.00$ for A2A coupling, $\beta = 1.96$ for the hypercube, and $\beta = 1.97$ for the PWR2 graph. The NN coupling shows a much weaker scaling of $\beta = 1.51$. (b) This plot illustrates how the physical time t taken to reach the maximum QFI scales with system size for the considered coupling graphs. For the A2A coupling case, $t = \pi$, and it is observed that the value for t aligns with the dashed line, provided as a guide for the eye, drawn at $t = \pi$.

which shows that the state with maximum QFI (Heisenberg limit) generated in the OAT dynamics is the GHZ state. In Fig. 7.3(c), $|\langle\psi_{GHZ}|\psi(t)\rangle|^2$ is plotted as a function of system size for different coupling graphs. As expected, we see a perfect overlap for the A2A coupling graph. The PWR2 and hypercube coupling graphs have a good overlap with the GHZ state, with $N = 64$ having more than 50% overlap. In contrast, the NN coupling graph exhibits a decreasing overlap, becoming negligible for larger system sizes. While we employ exact diagonalisation for smaller system sizes, all results for $N > 16$ are obtained using the time-dependent variational principle (TDVP) approach with matrix product states (MPS) [203, 204, 208, 216, 221, 222] introduced in Sec. 4.2.3.1. These results are for bond dimension $D = 256$ for $N = 32$ and $D = 512$ for $N = 64$, truncation error $\epsilon = 10^{-13}$, and the time step $\chi_0 dt = 10^{-2}$. To ensure convergence of our results, we vary truncation error and bond dimension for $N = 32$ and $N = 64$. In doing this, we find that the maximum error in the value of QFI for all graphs at t is at 2% level and this maximum error occurs for the hypercube geometry.

To understand the gain we get from using sparse interactions, it is instructive to compare the dynamics to the nearest neighbour model, Fig. 7.2(d), which shows much lower QFI throughout the dynamical evolution. It is thus evident that the sparse models create states with significantly higher QFI and emulate the OAT dynamics. In Fig. 7.4(a), we analyse how the maximum QFI scales with system size, specifically $F_Q(t) / N^{\beta}$, where t is physical time at which the QFI reaches its maximum. We extract β numerically and find that the PWR2 and hypercube-like geometry creates states that follow $F_Q(t) / N^{1.97}$ and $F_Q(t) / N^{1.96}$ respectively. The physical time t taken to reach the maximum F_Q is shown as a function of the system size N in Fig. 7.4(b). For the A2A coupling graph, this time is known to be constant at $t = \pi$ [8, 13, 14]. For the NN model, as expected, it increases linearly with the system size, whereas we observe that $t \quad N/\log_2 N$ in the sparse models. The analytical values of this time for the sparse coupling graphs can be extracted using Eq. (7.2) and are depicted as dashed lines in Fig. 7.4(b), corresponding to the colours of the respective coupling graphs.

7.3 Spectral Gap Analysis

To gain a deeper analytical understanding of why sparse coupling graphs mimic the dynamics of an A2A coupling graph, similar to the OAT dynamics, we conduct a spectral gap analysis. The OAT Hamiltonian given in Eq. (3.32) is highly degenerate, as all states with the same total magnetisation along the z-axis have equal energies. However, introducing perturbations in the form of non-uniform couplings, such as power-law interactions with coefficients $ji \quad jj^{s}$ breaks the permutational symmetry of the model, as shown in [282]. This lack of robustnes against perturbations leads to a loss of collective spin behaviour, which is crucial for generating metrologically useful states, as discussed in Sec. 3.3. Robustness in this context refers to the ability of the system to maintain its properties like collective spin behaviour and permutational symmetry under the influence of external perturbations. It has been shown that addition of spin aligning terms like $S_i.S_j$ would make the OAT Hamiltonian robust against these non-uniform power law perturbations [282]. Building on this idea, we show that in-

corporating spin-exchange interactions allows certain sparse coupling Hamiltonians to preserve the collective spin behaviour. To achieve this, it is instructive to rewrite the XY Hamiltonian in Eq. (7.1) for a given coupling graph $f\chi_{ij}g$ as

$$H_{XY} = \sum_{i,j} \chi_{ij}(S_i^x S_j^x + S_i^y S_j^y) = H_{gOAT} \quad \sum_{i,j}(\chi_0 \quad \chi_{ij}) S_i^z S_j^z, \tag{7.7}$$

where

$$H_{gOAT} = \chi J_z^2 \quad \sum_{i,j} \chi_{ij} \vec{S}_i \quad \vec{S}_j \tag{7.8}$$

is a generalized OAT model (introduced in [282]) composed of the usual OAT twisting term and the Heisenberg Hamiltonian. H_{gOAT} shares a basis of eigenvectors with $\hat{J}$ and J_z as $[H_{gOAT}, \hat{J}^2] = [H_{gOAT}, J_z] = 0$. This restricts the dynamics of the initial spin coherent states to the subspace of permutationally symmetric states discussed in Sec. 3.3.2. The term $V_{pert} = \sum_{i,j}(\chi_0 \quad \chi_{ij}) S_i^z S_j^z$ will then be responsible for the deviation from this collective spin behaviour, and how much deviation may occur depends on the spectral gap of the gOAT Hamiltonian. Moreover, both terms of H_{gOAT} commute, and so to analyse the energy gap between subspaces of defined J we focus our analysis on the Heisenberg Hamiltonian,

$$H_H = \sum_{i,j} \chi_{ij} \vec{S}_i \quad \vec{S}_j = \frac{1}{4} \sum_{ij} \chi_{ij} \vec{\sigma}_i . \vec{\sigma}_j = \sum_{ij} \chi_{ij} h_{(i,j)}, \tag{7.9}$$

where $$h_{(i,j)} = \frac{1}{4} \vec{\sigma}_i . \vec{\sigma}_j = \frac{1}{2} \left(\sigma_i^+ \sigma_j \quad + \sigma_i \quad \sigma_j^+ \right) + \frac{1}{4} \sigma_i^z \sigma_j^z . \tag{7.10}$$

The Hamiltonian in Eq. (7.9) has SU(2) symmetry, meaning it is invariant under global rotations of the spins. Due to the SU(2) symmetry, the ground state is not unique but forms a degenerate manifold. In particular, all the Dicke states $\left| J = \frac{N}{2}, M \right\rangle$ introduced in Sec. 3.3.2 can be ground states. For instance, if we consider one of the Dicke states

$$j \quad _0 i = j 0 i \quad ^N, \tag{7.11}$$

its corresponding energy $E_0 = \frac{1}{4}\sum_{ij}\chi_{ij}$. We can construct excitations from this base state by flipping a single spin, which leads to the family of states

$$|\phi_k\rangle = |00\ldots01_k0\ldots\rangle\,,\ k = 1,\ldots,N. \tag{7.12}$$

The Heisenberg interaction acts on this state as

$$h_{(i,j)}|\phi_k\rangle = \frac{1}{2}\left(\delta_{jk}|\phi_i\rangle + \delta_{ik}|\phi_j\rangle\right) + \frac{1}{4}\left(1 \quad 2(\delta_{ik}+\delta_{jk})\right)|\phi_k\rangle\,. \tag{7.13}$$

Using that $\chi_{ij} = \chi_{ji}$ we can prove that (see Appendix B)

$$H_H|\phi_k\rangle = \left(E_0 + \sum_j \chi_{kj}\right)|\phi_k\rangle \quad \sum_i \chi_{ik}|\phi_i\rangle\,. \tag{7.14}$$

7.3.1 One-Dimensional Graphs

The eigenstates of H_H can be obtained exactly when the coupling graph shows translational invariance. For a system in one dimension and periodic boundary conditions, this means that the coupling strengths can expressed as a function of

$$\chi_{ij} \quad \chi(|i \quad j|) \tag{7.15}$$

which obeys $\chi(d) = \chi(d \quad N)$, $\chi(0) = 0$, where $d = |i \quad j|$. One can use spin-wave theory to describe the eigenstates of this Hamiltonian [283–285]. This is because the ground state has long-range order, and the excited states can be represented as collective oscillations of the spins around this ordered state. These excitations are known as spin waves or magnons, where the eigenstates correspond to wave-like disturbances

propagating through the lattice i.e.

$$|\psi_q\rangle = \frac{1}{\sqrt{N}} \sum_{k=1}^{N} e^{ik\frac{2\pi}{N}q} |\phi_k\rangle\,, \text{ with } q = 1, \ldots, N-1, \tag{7.16}$$

$$\text{and} \quad H_H |\psi_q\rangle = E_0 |\psi_q\rangle + \frac{1}{\sqrt{N}} \sum_k e^{ik\frac{2\pi}{N}q} \left(\sum_j \chi(k-j) \left(1 - e^{i(j-k)\frac{2\pi}{N}q}\right) \right) |\phi_k\rangle\,. \tag{7.17}$$

Due to the SU(2) symmetry of the Hamiltonian in Eq. (7.9), $|\psi_{q=0}\rangle$ is also the ground state of the Hamiltonian. Using translational invariance and periodic boundary conditions, we can derive an expression for the gaps $\Delta(q) = E_q - E_0$ (see Appendix B for more details), which is given by:

$$N \text{ even}: \quad \Delta(q) = 2\sum_{d=1}^{\frac{N}{2}} \chi(d) \left(1 - \cos\left(\frac{2\pi}{N} dq\right)\right) - \chi\left(\frac{N}{2}\right)(1 - e^{i\pi q}), \tag{7.18}$$

$$N \text{ odd}: \quad \Delta(q) = 2\sum_{d=1}^{\frac{N-1}{2}} \chi(d) \left(1 - \cos\left(\frac{2\pi}{N} dq\right)\right), \tag{7.19}$$

where $d = k - j$ sets the distance between the spins. In many cases, the lowest-energy excitation corresponds to $q = 1$; however, this is not always the case, as it depends on the coupling graph. To better understand this, we plot the energy gap as a function q for a system size $N = 64$, identifying where the minima occur, as shown in Fig. 7.5(a). For the PWR2 coupling graph, we observe that the smallest gap occurs at $q = N/2$, while for the A2A and NN coupling graphs, the smallest gap is found at $q = 1$ (see Fig. 7.5(a) inset).

PWR2 Graph

For the PWR2 graph with periodic boundary conditions, we have

$$\chi(d) = \chi_0, \text{ if } d = 2^r \text{ or } N - d = 2^r,\ r = 0, 1, \ldots \tag{7.20}$$

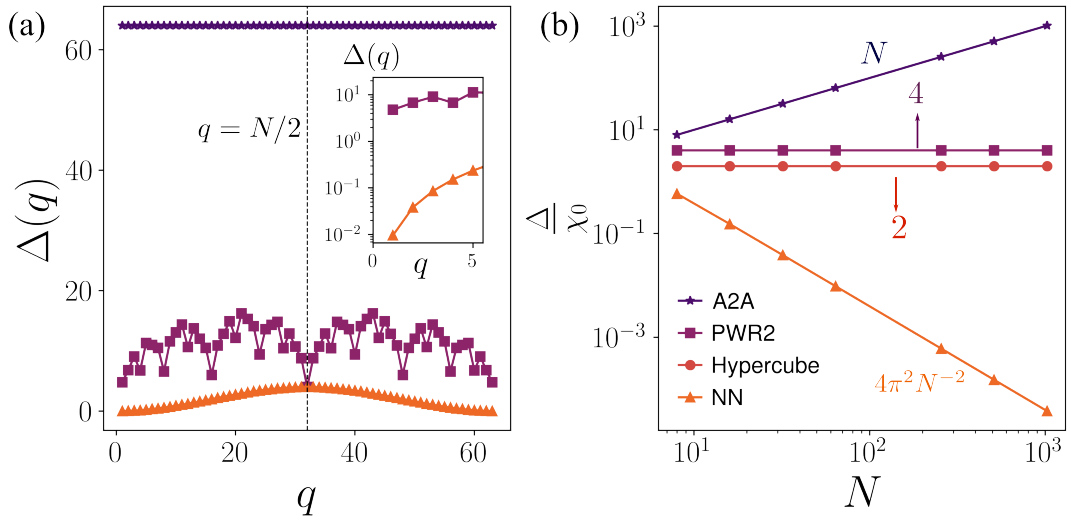

Figure 7.5: **Spectral Gap of the Heisenberg Hamiltonian** (a). The energy gap of the Hamiltonian in Eq. (7.8), $(q) = E_q \quad E_0$, given in Eq. (7.18) is plotted as a function of q for $N = 64$ for A2A, PWR2 and NN coupling graphs. We observe that the lowest-energy excitation occurs at $q = 1$ for the A2A and NN coupling graphs (see inset for a zoomed-in view of the spectral gap near $q = 1$). By contrast, for the PWR2 coupling graph, it occurs at $q = N/2$ (see legend in (b) for colours and markers). The dashed black at $q = N/2$ is included as a visual reference. (b). The spectral gap of the isotropic Heisenberg Hamiltonian in Eq. (7.8) as a function of system size N for different coupling graphs with various levels of connectivity. Systems with asymptotically vanishing gaps deviate from the collective OAT dynamics, while systems with non-vanishing gaps in the large-N limit display robust collective dynamics capable of generating metrologically useful states. Examples of the former are the nearest-neighbour graph (NN) coupling graph, whereas the latter category includes the all-to-all (A2A) coupling and the sparse PWR2 and hypercube coupling graphs studied here, both of which maintain a constant gap as a function of system size.

Restricting to even N, and $q = N/2$ we obtain,

$$\text{PWR2} = \sum_{r=0}^{\log_2(N)\ 1} 2\chi_0 (1 \quad \cos(\pi 2^r)) \quad 2\chi \left(\frac{N}{2}\right) (1 \quad e^{i\pi\frac{N}{2}}) = 4\chi_0. \tag{7.21}$$

The result then indicates that the energy gap separating the collective states from the rest of the spectrum is finite for all N, and independent of system size.

All-to-All Graph

The gap can be worked out exactly from Eq. (7.18) with $q = 1$. We calculate the gap as

$$_{\text{A2A}} = 2\chi_0 \sum_{d=1}^{\frac{N}{2}} \left(1 \quad \cos\left(\frac{2\pi}{N} dq\right)\right) \quad 2\chi_0 = N\chi_0, \tag{7.22}$$

which shows the expected N scaling.

Nearest-Neighbour Graph

For nearest neighbour coupling with periodic boundary conditions,

$$\chi(m) = \chi_0(\delta_{d,1} + \delta_{d,N \ 1}), \tag{7.23}$$

and assuming even N, and $q = 1$, the gap corresponds to

$$_{\text{NN}} = 2\chi_0 \left(1 \quad \cos\left(\frac{2\pi}{N}\right)\right) \quad 4\pi^2 N^{\ 2}, \tag{7.24}$$

which decays as N increases.

7.3.2 Hypercube Coupling Graph

To calculate the spectral gap of the hypercube coupling graph, it is important to note that, while this graph lacks translational invariance in one dimension, it is inherently "translationally invariant" in $D = \log_2(N)$ dimensions. This means that, when shifting from one vertex to another (corresponding to movement in a particular direction), the local neighbourhood remains invariant. Also, there are only two sites in each direction, and all these suggest that excited states form D-dimensional spin-wave states. For a given site $k = 1, 2, \ldots, N$, a D dimensional vector can be constructed from the binary representation of k, i.e.

$$\vec{B}_k = (b_0, b_1, \ldots, b_{D \ 1}), \tag{7.25}$$

where b_i are the binary digits of k. The Hamming distance $d_H(i, j) = j\vec{B}_i \quad \vec{B}_j j$ between two sites i and j represents the number of differing bit positions in the binary

representations of i and j. In the context of the hypercube graph, the condition $\chi_{ij} = \chi_0$ holds when $d_H(i,j) = 1$; otherwise $\chi_{ij} = 0$. Given this framework, the spin-wave states can be explicitly constructed as

$$\left| \vec{q} \right\rangle = \sum_{k=1}^{N} e^{i\frac{2\pi}{L}\vec{B}_k\cdot\vec{q}} |\phi_k\rangle , \tag{7.26}$$

where $\vec{q}$ is a now a D-dimensional spin-wave vector and L represents the number of lattice points along one dimension. Since each direction has only two sites, the wavenumber can only take the values $q_i = 0, 1$ and $L = 2$. The action of H_H on this state is analogous to Eq. (7.17). The expression in the brackets in Eq. (7.17), which corresponds to the gap will change accordingly. For a given site k in the hypercube graph, there are D other sites connected to it, and hence D possible choices of j such that $\vec{B}_j - \vec{B}_k = 1$. The corresponding gap $_{\text{HYP}}$ can be calculated as

$$_{\text{HYP}} = \chi_0 \sum_{l=1}^{D} \left(1 - e^{iq_l}\right) , \text{ where } q_l = 0, 1. \tag{7.27}$$

Setting all $q_l = 0$ corresponds to the ground state, while the first excited state occurs when one of the $q_l = 1$ and the others remain zero. In this case, the gap simplifies to

$$_{\text{HYP}} = \chi_0(D - (D - 2)) = 2\chi_0. \tag{7.28}$$

This result shows that the spectral gap is independent of N, similar to the case of the PWR2 coupling graph. These calculations show how the collective dynamics generated by the hypercube and PWR2 coupling graphs, under the spin-exchange Hamiltonian in Eq. (7.1), are robust against non-collective perturbations. This explains why these models are capable of producing metrologically useful states. To visually see this gain, we plot the spectral gap of the Heisenberg Hamiltonian Eq. (7.8) as a function of the system size N in Fig. 7.5(b).

7.4 Towards Experimental Observation

In Sec. 7.3, we studied the spectral gap of the spin-exchange Hamiltonian for different coupling graphs and obtained an analytical understanding of why the sparsely coupled graphs particularly PWR2 and hypercube maintain the collective spin behaviour. We now shift our focus to proposing possible experimental implementations of these models. The platform that we wish to focus on is the neutral atom arrays with the aid of tweezer-assisted shuffling operations. This choice, as mentioned in Sec. 1.4, comes from the flexibility offered for atom manipulation, good scalability, and the ability to control each atom coherently. In Sec. 6.4, we introduced the "Faro Shuffle" operation, that moves the atom according to the algorithm given in Eq. (6.44). The hypercube geometry is native to this Faro shuffle, and here, we propose an algorithm to implement the spin-exchange Hamiltonian given in Eq. (7.1) in near-term neutral atom platforms.

Recently, a dipolar XY model has been experimentally realised in a Rydberg simulator up to $N = 100$ atoms, where scalable spin squeezing was demonstrated [160]. This was achieved in a square array of Rb atoms by encoding the effective spin $1/2$ degree of freedom in the Rydberg states of opposite parity. By contrast, the quantum Ising model is realised by encoding the spin $1/2$ degree of freedom in the ground and the excited state [271, 286]. Excited Rydberg states are short-lived and this places the implementation of XY Hamiltonian at a slight disadvantage as both the spin-$1/2$ degrees of freedom are in the Rydberg state. However, the XY Hamiltonian can be simulated using global rotations, and Ising ZZ interactions. This forms the basis for our approach to implementing the spin-exchange Hamiltonian in the hypercube geometry. We propose to use global $\pi/2$ rotations

$$R_\alpha = e^{\,i\pi/4\sum_a \sigma_a^\alpha} \quad \alpha \in \{x, y\}, \tag{7.29}$$

and

$$H_{zz} = 2\chi_0 \sum_\nu S_{2\nu}^z \; {}_1S_{2\nu}^z \tag{7.30}$$

ZZ interactions, where ν indicates the atomic position, rather than the spin index. During each time step $dt = t/M$, we apply $m \in \{1, .. \log_2(N)\}$ Faro shuffles R to

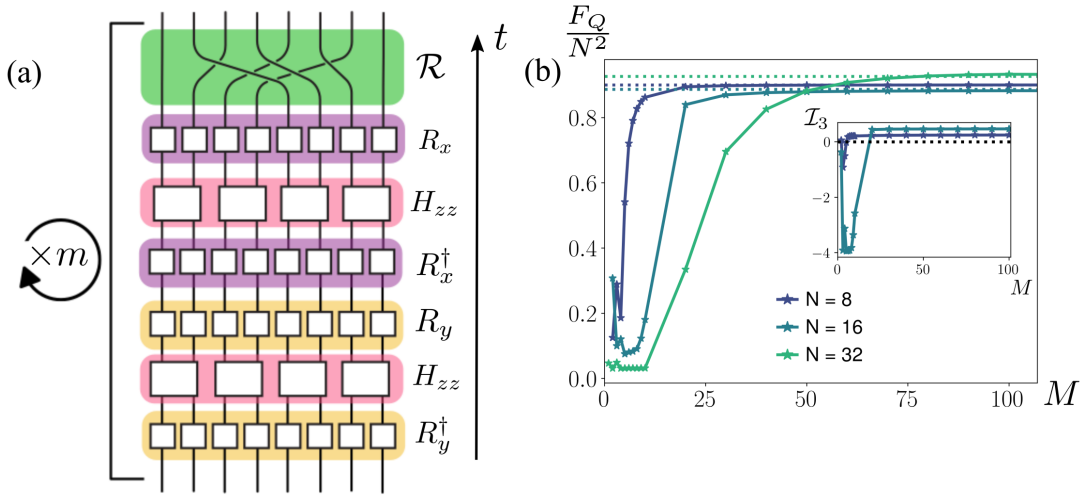

Figure 7.6: **Proposed Experimental Implementation to Create Metrologically Relevant States** (a). Our circuit implementation consists of single qubit rotations Eq. (7.29) (purple for R_x and yellow for R_y) followed by ZZ interactions between nearest neighbour spins according to Hamiltonian in Eq. (7.30) (pink for H_{zz}) and Faro shuffles R (green). The application of the ZZ interaction Hamiltonian and global rotations are done in $m = \log_2(N)$ steps where N is the number of spins involved. (b). The QFI F_Q normalized to its maximum value N^2 is plotted as a function of the number of iterations M, where we evolve the initial x-polarized state up to $t = t$ according to Eq. (7.32). The dashed lines of corresponding colours represent the values of $\frac{F_Q}{N^2}$ for $N = 8, 16, 32$ respectively at $t = t$ extracted from the continuous time analysis shown in Fig. 7.4(a). (inset) The tripartite mutual information I_3 is plotted as a function of the number of iterations M to show a sharp deviation from the permutationally symmetric subspace to a scrambled region characterized by negative I_3. The horizontal black dashed line represents $I_3 = 0$.

build up the hypercube coupling graph. Before each shuffling operation, we evolve the system according to

$$U_m(dt) = \left[R_x e^{\ iH_{zz}dt/2} R_x^y\right]\left[R_y e^{\ iH_{zz}dt/2} R_y^y\right], \tag{7.31}$$

where the subscript m indicates the step of the Faro shuffle when the ZZ Hamiltonian and the global rotations are applied. One of these steps is illustrated in Fig. 7.6(a). This effectively realises a first-order Trotter decomposition, such that the full evolution

during one-time step takes the following form

$$U(t, t + dt) = \prod_m R U_m(dt) \ . \tag{7.32}$$

We simulate this stroboscopic evolution and compare it to the continuous-time model discussed in Sec. 7.2. In this way, we dynamically generate an effective hypercube geometry for the spins, and observe that F_Q indeed acquires its maximum value for experimentally attainable iterations of $M < 100$, where we evolved the initially x-polarized state up to maximum physical time t . This is shown in Fig. 7.6(b) where the QFI is plotted as a function of the number of iterations M for $N = 8, 16, 32$. The horizontal lines of the corresponding colours indicate the maximum QFI, $F_Q(t)$, extracted from the continuous time evolution as shown in Fig. 7.4(a). In addition, we also calculate the tripartite mutual information I_3 introduced in Sec. 2.4. As discussed in the same section I_3 can be positive for permutationally symmetric states as shown in Eq. (2.10). A simple example is the Greenberger-Horne-Zeilinger GHZ state, that has $I_3 = \log 2$. In Fig. 7.6(b) (inset), we plot the I_3 as a function of the number of iterations M for system sizes $N = 8, 16$. We observe that for $M > 10$ in these two system sizes, the tripartite mutual information is positive, supporting our previous analyses of collective spin behaviour. Calculating I_3 for larger system sizes using MPS-MPO techniques is challenging, as discussed in Sec. 6.5, and is left for future work. These plots are present to show that the collective nature is preserved for larger M and is also reflected in I_3. The PWR2 coupling graph can also be generated through these dynamical shuffling operations, and we detail this scheme in Appendix C.

7.5 Conclusions

In Ch. 7, we demonstrated the effectiveness of sparse coupling graphs with a logarithmic number of couplings in generating highly entangled states. Specifically, in Sec. 7.2, we examined how the PWR2 and hypercube coupling graphs can mimic the dynamics of the A2A coupling graph under the XY Hamiltonian. To gain a deeper understanding, we analytically computed the spectral gap of the generalised OAT Hamiltonian for

various coupling graphs in Sec. 7.3. Notably, we found that both the PWR2 and hypercube graphs exhibit a constant gap as a function of system size N, ensuring the robustness of collective spin behaviour against perturbations. This is akin to the A2A model, where the gap increases with N, and in stark contrast to the NN model, where the gap diminishes with system size. Moreover, these models can be realised in near-term experimental platforms and in Sec. 7.4, we presented a stroboscopic method that may be experimentally realised on current neutral atom arrays, that leverages only nearest-neighbour Ising interactions, local rotations, and tweezer-assisted shuffling. Importantly, through these coupling graphs and protocols, we generated states with Heisenberg scaling in QFI, a hallmark of highly entangled states.

Chapter 8

Conclusions and Future Directions

This thesis, while addressing multiple concepts and seemingly diverse topics, revolves around a central goal: understanding the dynamics of entanglement buildup in systems with tunable range interactions and leveraging their potential to create states useful for quantum-enhanced metrology. To achieve this, we investigated a range of sparsely coupled models and demonstrated that, near the crossover between two geometries with differing notions of locality, *a transition occurs between regions of distinct dynamical behaviour, marking the onset of scrambling.* Additionally, we utilised these *sparse coupling graphs to generate states with metrological relevance*, illustrating potential experimental realisations on near-term neutral atom array platforms using optical tweezers. In this chapter, we provide a summary of the results and an outlook for future directions opened by this work.

8.1 Summary

We first established the theoretical framework necessary for understanding quantum information scrambling and quantum-enhanced metrology. In Ch. 1, we discussed how the fast scrambling conjecture imposes a fundamental limit on the growth rate of entanglement entropy, $t \not\propto \log N$, where N is the system size. Recognizing the importance

of non-local interactions as a key factor for fast scrambling, we then introduced the motivation for studying scrambling dynamics in sparse coupling graphs. Then in Ch. 2, we discussed various measures of quantum information scrambling. We introduced the concepts of lightcones, entanglement entropy, and tripartite mutual information. In Ch. 3 we reviewed the fundamental concepts revolving around phase estimation, including quantum Fisher information, collective spin behaviour, and spin squeezing. We discussed that the fundamental bound on the quantum Fisher information for separable states is governed by the standard quantum limit, $F_Q = N$, while for entangled states, it is determined by the Heisenberg limit, $F_Q = N^2$. These three chapters provided the foundation and framework for the analyses in the later chapters.

In Ch. 5, we explored how the notion of geometry, entanglement build-up, and lightcones are closely related. To achieve this, we studied sparse Clifford circuits featuring powers of two interactions, where the interactions are tuned using a parameter s to either decay or grow with distance. Based on the scaling of the entanglement entropy with system size, we were able to distinguish between 'contiguous' subregions in the linear (Euclidean) and treelike (ultrametric) geometry. By tuning the interactions, we showed that we can smoothly interpolate between these two geometries with a fast scrambling regime near $s = 0$.

Having established the presence of a fast scrambling regime, we continued our investigation around the $s = 0$ region of these sparse models. In Ch. 6, we identified a dynamical transition marking the onset of scrambling characterised by tripartite mutual information. Particularly, we showed that as a function of the tunable power law exponent s and at a time of $O(1)$, the tripartite mutual information vanishes when $s < s_c$ and becomes large and negative for $s > s_c$, where s_c is the critical value of the tunable parameter. We observed this transition in both sparse and densely coupled models; and deterministic and random models. We also studied this transition analytically using an associated Brownian circuit model, which can be mapped to the long-range Ising model in a particular parameter regime. Additionally, we also estimated the mean-field critical

exponent and found it to agree with our Clifford simulation results thus supporting the presence of a critical point and hence a phase transition. This transition connects to practical applications in noisy devices, especially in identifying regimes where resource states can be generated on timescales that grow only logarithmically with the size of the system so that the relevant system size can grow exponentially with the coherence time.

As established in Ch. 5 and Ch. 6, sparse coupling models are efficient entanglement generators. In Ch. 7, we further explored the potential of these sparse coupling graphs by investigating their utility in quantum-enhanced metrology. Through both numerical and analytical methods, we showed that powers of two and hypercube coupling graphs can replicate the dynamics of all-to-all spin models, such as the one-axis twisting model, even for large system sizes. This enables the generation of metrologically relevant states with only a logarithmic number of couplings, eliminating the need for all-to-all Ising interactions. Additionally, we proposed a stroboscopic protocol, which can be implemented on current neutral atom arrays using only tweezer shuffling, nearest-neighbour Ising interactions, and local rotations to prepare states that exhibit Heisenberg scaling.

8.2 Outlook

While significant progress has been made, the journey ahead is filled with excitement, as there remains much more to uncover and achieve. A number of compelling theoretical and computational questions emerge from the analysis in Ch. 6. Drawing from Steve Gubser's field theory work [45], we observe that a smooth interpolation between linear and treelike geometries is indeed feasible. Our results show a transition near $s = 0$ in these sparse models. This raises an important question: Can such a transition also be detected in a continuous-time model? If so, could this transition be effectively characterized by tripartite mutual information? Our initial investigations began by focusing on the tripartite mutual information in the transverse field Ising model, but we encountered significant challenges in calculating this quantity for larger system sizes using MPS-MPO simulations. This leads us to the following question: How can we bypass these computational problems? One potential approach involves leveraging the classi-

cal shadows protocol to estimate state properties [272]. However, are there alternative observables that could characterise this transition and be more efficiently computed for larger system sizes? Additionally, extending this study to Fermionic models, alongside the Brownian circuit model explored in Ch. 6, where analytical solutions are accessible, could offer further insights.

Towards an experimental point of view, we proposed a model in Ch. 6 involving tweezer-assisted shuffling operations, and nearest neighbour controlled Z gates for realising this transition. Measuring the tripartite mutual information involves measuring entanglement entropies of different subregions. In practice, the second-order Rényi entropy can be measured in the cold atom setup by quantum interference of many-body twins [248, 249] or by performing randomized measurements [252, 253]. For $N = 16$, we would be required to measure the entanglement entropy of a maximum of 8 qubits. For randomized measurements [252, 253], it is known that the number of measurements required for estimating the second-order Rényi entropy $S_A^{(2)}$ scales exponentially with the size of the subregion A. Hence, by preparing a single copy of the qubit state of interest at each time step, the estimation of entanglement entropy can be done using average 10^3 to 10^4 measurements. However, these measurements tend to be quite challenging in practice, and it is important to think carefully about how a given protocol would perform given the realities of dissipation and repetition rates in specific platforms [287]. One potential approach to this problem is to treat the system as an open quantum system and analyse its dynamics using the master equation. This could involve studying continuous-time analogues of the models, which we have begun to explore using the transverse field Ising model. We leave further investigation of this for future work.

In Ch. 7, we proposed a stroboscopic protocol to generate states with Heisenberg scaling. The same protocol can be used to create spin-squeezed states using these sparse graphs. One major theoretical outlook for this work that will benefit the implementation in near-term experimental platform will be to check the robustness of these protocols to dissipation and decoherence. The stroboscopic protocol proposed for the

generation of metrologically useful states relies on three key components:

(1) dynamical optical tweezer reconfiguration which allows to shuffle the position of the atoms,

(2) local rotations R_α around the $\alpha = x, y$ axis by a fixed angle $\pi/2$ as given in Eq. (7.29),

(3) implementation of zz or Ising interactions, described by the Hamiltonian H_{zz} given in Eq. (7.30) for a time interval of $dt/2 = t/(2M)$.

The local rotations are readily achieved by using microwave or Raman pulses, while entangling operations utilize controlled phase gates, successfully demonstrated in recent Rydberg atom experiments [58, 288]. An important next step would be to theoretically calculate the standard error rates that might arise when employing these state-of-the-art processes. Understanding these errors will provide information about the reliability and practicality of the protocol in experiments and help identify ways to improve it. Additionally, while we have simulated spin models on a graph in this work, extending these techniques to digital circuit models could open new avenues for fault-tolerant preparation of metrologically relevant states.

From Einstein's description of entanglement as "spooky action at a distance" to today's efforts in engineering complex forms of entanglement in atomic, molecular, and optical systems, we've come a long way. These are exciting times, with analogue quantum simulators revealing insights into complex phenomena [27] and significant work being dedicated to creating fault-tolerant gates for digital simulators [289–291]. Over time, these advancements will undoubtedly deepen our understanding of how entanglement builds up, and help us observe exotic physics in new ways.

Appendix A

Additional calculations for the Brownian circuit model

In Ch. 6, we introduced the Brownian circuit model to study analytically the dynamical transition marking the onset of scrambling. Here, we provide some additional calculations to support the analysis in the main text of Sec. 6.3.

A.1 Formulation of the Basis Vectors

To construct the basis vectors for the singlet subspace introduced in Sec. 6.3.4, we follow the approach outlined in [243, 244]. The basis states, as presented in the main text, are given by

$$\begin{aligned} |''\rangle &= \frac{1}{2\sqrt{3}}\left(2|1010\rangle + 2|0101\rangle - |0011\rangle - |1100\rangle - |1001\rangle - |0110\rangle\right), \\ |\#\rangle &= \frac{1}{2}\left(|0011\rangle + |1100\rangle - |1001\rangle - |0110\rangle\right). \end{aligned} \tag{A.1}$$

To derive this, we use the pictorial representation given in Fig. A.1. For the $|\#\rangle$ state, we consider a spin singlet state formed between replicas $r = 1$ and $r = 3$, and $r = 2$

and $r = 4$, yielding

$$|\#\rangle = \frac{1}{\sqrt{2}}(|01\rangle - |10\rangle)_{1,3} \frac{1}{\sqrt{2}}(|01\rangle - |10\rangle)_{2,4}, \tag{A.2}$$

$$|\#\rangle = \frac{1}{2}(|0011\rangle + |1100\rangle - |1001\rangle - |0110\rangle), \tag{A.3}$$

where the subscript r, s identifies the replicas between which the singlet state is created.

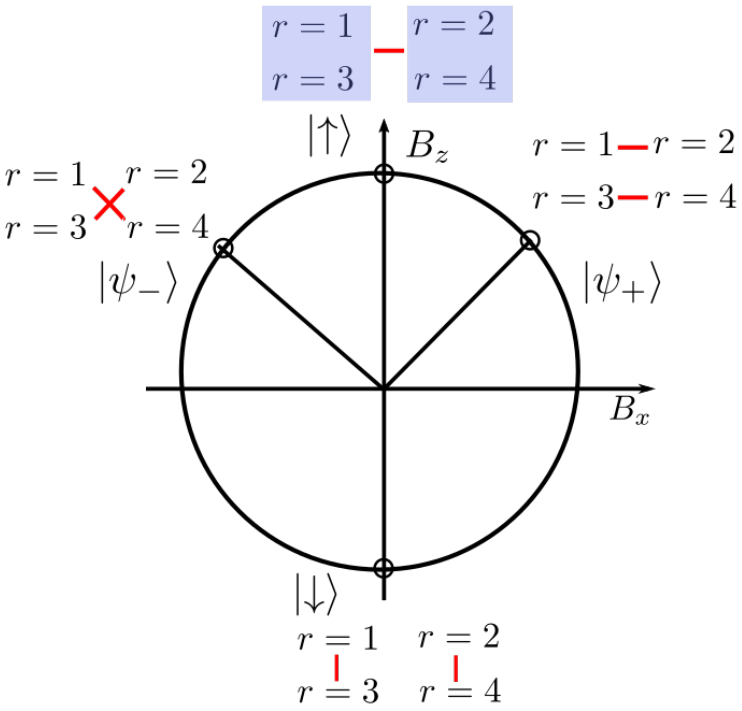

Figure A.1: **Illustration of Basis Vector Construction in the Singlet Subspace.** The basis vector $|"\rangle$ is formed by considering singlet pairs between the combined replicas $r = 1$ and $r = 3$, and $r = 2$ and $r = 4$. The combined replicas are highlighted with blue shading, and the singlet pairings are represented by red lines. In contrast, the basis vector $|\#\rangle$ is constructed by considering singlet pairs between replicas $r = 1$ and $r = 3$, and $r = 2$ and $r = 4$. Additionally, we also show the saddle point solutions $|\psi_- \rangle$ as singlet pairs between corresponding replicas.

For the $|"\rangle$ state, we first combine replicas $r = 1$ and $r = 3$ into a spin 1 system and similarly combine replicas $r = 2$ and $r = 4$. These two spin-1 systems are then

combined to form a singlet state, resulting in (see Fig. A.1)

$$|\psi''\rangle = \frac{1}{\sqrt{3}}(|1\quad 1\rangle \quad |00\rangle + |\quad 11\rangle), \tag{A.4}$$

$$|\psi''\rangle = \frac{1}{\sqrt{3}}\Big(|1010\rangle + |0101\rangle \quad \frac{1}{2}(|01\rangle + |10\rangle)_{1,3}(|01\rangle + |10\rangle)_{2,4}\Big), \tag{A.5}$$

$$|\psi''\rangle = \frac{1}{2\sqrt{3}}\,(2|1010\rangle + 2|0101\rangle \quad |0011\rangle \quad |1100\rangle \quad |1001\rangle \quad |0110\rangle)\,. \tag{A.6}$$

A.2 Derivation of the saddle points

In Sec. 6.3.4 of Ch. 6, we calculated the saddle point solutions of the action in Eq. (6.30). Here, we provide a detailed derivation. The two key equations are

$$\phi_i^a + \phi_i^b = 3J\,, \tag{A.7}$$

$$\phi_i^a \quad \phi_i^b = \quad 3J\,, \tag{A.8}$$

for the lowest order in b. These equations present us with two cases, which we will examine individually.

Case 1

For case 1, we take $\phi_i^a \quad \phi_i^b = 3J$ and subtract Eq. (A.8) from Eq. (A.7). This gives $\phi_i^a = 3J$ and $\phi^b = \phi_i^c = 0$. Consequently, from Eq. (6.33), Eq. (6.34), and Eq. (6.35), we obtain $iF_i^{12} = iF_i^{34} = 3J/2$. We then apply these constraints back in Eq. (6.28), and we find

$$\begin{aligned} B_i^x &= \frac{\sqrt{3}}{2}(3J)\,, \\ B_i^y &= 0, \\ B_i^z &= \frac{1}{2}(3J)\,. \end{aligned} \tag{A.9}$$

This positions one of the saddle points $|\psi_+\rangle$ as shown in Fig. 6.5.

Appendix A. Additional calculations for the Brownian circuit model

Case 2

Similarly, for Case 2, we consider $\phi_i^a \quad \phi_i^b = \quad 3J$. Performing the same analysis, we find $iF_i^{14} = iF_i^{23} = 3J/2$. The corresponding fields are:

$$\begin{aligned} B_i^x &= \quad \frac{p\overline{3}}{2}(3J), \\ B_i^y &= 0, \\ B_i^z &= \frac{1}{2}(3J). \end{aligned} \tag{A.10}$$

This positions $j\psi \quad i$ as shown in Fig. 6.5. We also show that when $\sigma_i = +1$ we find that $G_i^{12} = G_i^{34} = \quad 3/4 + O(b)$ with all other fields vanishing, while for $\sigma_i = \quad 1$ we find that $G_i^{14} = G_i^{23} = \quad 3/4 + O(b)$. This result can be easily seen in the lowest order of b by using Eq. (6.31)

$$\begin{aligned} iF_i^{rs} &= 2J(\quad 1)^{r+s}\sum_j \chi_{ij}G_j^{rs}, \\ iF_i^{rs} &= 2J(\quad 1)^{r+s}\sum_j [(1 \quad b)\delta_{ij} + bA_{ij}]G_j^{rs}, \\ iF_i^{12} &= 2J(\quad 1)^3\sum_j [bA_{ij}G_j^{12}] + 2J(\quad 1)^3(1 \quad b)G_i^{12}. \end{aligned} \tag{A.11}$$

Given that $iF_i^{12} = iF_i^{34}$, and $iF_i^{12} = \frac{\phi_i^a}{2}$, where $\phi_i^a = 3J$, we have:

$$\begin{aligned} \frac{3J}{2} &= \quad 2J\sum_j [bA_{ij}G_j^{12}] \quad 2J(1 \quad b)G_i^{12}, \\ G_i^{12} &\quad \frac{3}{4}. \end{aligned} \tag{A.12}$$

A similar analysis may be done to calculate $G_i^{14} = G_i^{23} = \quad 3/4$.

Appendix B

Spectral gap calculations

In Sec. 7.3 of Ch. 7, we calculated the spectral gap of Hamiltonian to support our study of how the sparse coupling graph emulates the all-to-all coupling graph. Here, we derive the results stated in the main text. The isotropic Heisenberg Hamiltonian

$$H_H = \frac{1}{4}\sum_{ij}\chi_{ij}\vec{\sigma_i}.\vec{\sigma_j} = \sum_{ij}\chi_{ij}h_{(i,j)}, \tag{B.1}$$

where $$h_{(i,j)} = \frac{1}{4}\vec{\sigma_i}.\vec{\sigma_j} = \frac{1}{2}\left(\sigma_i^+\sigma_j + \sigma_i\,\sigma_j^+\right) + \frac{1}{4}\sigma_i^z\sigma_j^z \tag{B.2}$$

has a ground state corresponding to all spins pointing along the same direction, for instance $|j\;{}_0i = |0i\;{}^N$. As mentioned in the main text, the excitations can be constructed by flipping a single spin, leading to a family of states given by $|j\phi_k i = |00\ldots01_k0\ldots i$, where $k = 1,\ldots,N$. To derive Eq. (7.13) of how Heisenberg interaction acts on this state, we consider the interaction Hamiltonian term-wise,

$$\sigma_i^+\sigma_j\;|j\phi_k i = \delta_{jk}|j\phi_i i\,, \tag{B.3}$$

$$\sigma_i\;\sigma_j^+\,|j\phi_k i = \delta_{ik}|j\phi_j i\,, \tag{B.4}$$

$$\text{and}\quad \sigma_i^z\sigma_j^z\,|j\phi_k i = (1 \quad 2(\delta_{ik}+\delta_{jk}))\,|j\phi_k i\,. \tag{B.5}$$

Combining Eq. (B.3), Eq. (B.4), and Eq. (B.5), we obtain Eq. (7.13),

$$h_{(i,j)}|j\phi_k i = \frac{1}{2}\left(\delta_{jk}|j\phi_i i + \delta_{ik}|j\phi_j i\right) + \frac{1}{4}(1 \quad 2(\delta_{ik}+\delta_{jk}))\,|j\phi_k i\,. \tag{B.6}$$

Appendix B. Spectral gap calculations

Since $\chi_{ij} = \chi_{ji}$, we obtain

$$H_H|\phi_k\rangle = \sum_{ij}\chi_{ij}\left(\frac{1}{2}\delta_{jk}|\phi_i\rangle + \frac{1}{2}\delta_{ik}|\phi_j\rangle\right) + \left(\frac{1}{4} \quad \frac{1}{2}(\delta_{ik}+\delta_{jk})\right)|\phi_k\rangle\,, \tag{B.7}$$

$$H_H|\phi_k\rangle = (E_0 + \sum_j \chi_{kj})|\phi_k\rangle \quad \frac{1}{2}\left(\sum_i \chi_{ik}|\phi_i\rangle + \sum_i \chi_{kj}|\phi_j\rangle\right), \tag{B.8}$$

$$H_H|\phi_k\rangle = \left(E_0 + \sum_j \chi_{kj}\right)|\phi_k\rangle \quad \sum_i \chi_{ik}|\phi_i\rangle\,. \tag{B.9}$$

As mentioned in the main text, in Sec. 7.3, we use the spin-wave theory to describe the excitations around the ground state in this model. The spin waves are

$$|\quad_q\rangle = \cancel{p}\frac{1}{\overline{N}}\sum_{k=1}^{N} e^{ik\frac{2\pi}{N}q}|\phi_k\rangle\,, \text{ with } q = 1,\ldots,N \quad 1. \tag{B.10}$$

Next, we calculate $H_H|\quad_q\rangle$, and for that, it is instructive to write

$$H_H|\quad_q\rangle = \cancel{p}\frac{1}{\overline{N}}\sum_{k=1}^{N} e^{ik\frac{2\pi}{N}q}H_H|\phi_k\rangle\,, \tag{B.11}$$

and using Eq. (B.9), $H_H|\quad_q\rangle = \cancel{p}\frac{1}{\overline{N}}\sum_{k=1}^{N} e^{ik\frac{2\pi}{N}q}\left(E_0 + \sum_j \chi_{kj}\right)|\phi_k\rangle \quad \sum_i \chi_{ik}|\phi_i\rangle\,.$ (B.12)

This yields

$$H_H|\quad_q\rangle \quad E_0|\quad_q\rangle = \cancel{p}\frac{1}{\overline{N}}\sum_{k=1}^{N} e^{ik\frac{2\pi}{N}q}\left(\sum_j \chi_{kj}\left(1 \quad e^{i(j\quad k)\frac{2\pi}{N}q}\right)\right)|\phi_k\rangle\,. \tag{B.13}$$

Now, we calculate the gap, and for that we take an inner product with $|\quad_q\rangle$, and this yields

$$(q) = \frac{1}{N}\sum_k\sum_j\left(\chi_{kj}\left(1 \quad e^{i\frac{2\pi q}{N}(j\quad k)}\right)\right). \tag{B.14}$$

Let $d = k \quad j$, and using this ansatz in Eq. (B.14), we get

$$(q) = \frac{1}{N}\sum_{k=1}^{N}\left(\sum_{d=1}^{N}\chi(d)\left(1 \quad e^{\,i\frac{2\pi qd}{N}}\right)\right), \tag{B.15}$$

$$(q) = \sum_{d=1}^{N}\chi(d)\left(1 \quad e^{\,i\frac{2\pi qd}{N}}\right). \tag{B.16}$$

Let us consider N to be even and hence,

$$(q) = \sum_{d=1}^{N/2}\chi(d)\left(1 \quad e^{\,i\frac{2\pi qd}{N}}\right) + \sum_{d=N/2+1}^{N}\chi(d)\left(1 \quad e^{\,i\frac{2\pi qd}{N}}\right). \tag{B.17}$$

Due to the imposed periodic boundary condition and translational invariance in one dimension, we have $\chi(d) = \chi(N \quad d)$. Hence Eq. (B.17) is written as

$$(q) = \sum_{d=1}^{N/2}\chi(d)\left(1 \quad e^{\,i\frac{2\pi qd}{N}}\right) + \sum_{d=1}^{N/2}\chi(N \quad d)\left(1 \quad e^{\,i\frac{2\pi q(N \quad d)}{N}}\right), \tag{B.18}$$

$$(q) = \sum_{d=1}^{N/2}\chi(d)\left(1 \quad e^{\,i\frac{2\pi qd}{N}}\right) + \sum_{d=1}^{N/2}\chi(N \quad d)\left(1 \quad e^{i\frac{2\pi qd}{N}}\right), \tag{B.19}$$

$$(q) = \sum_{d=1}^{N/2}\chi(d)\left(2 \quad 2\cos\left(\frac{2\pi}{N}dq\right)\right), \tag{B.20}$$

$$(q) = 2\sum_{d=1}^{N/2}\chi(d)\left(1 \quad \cos\left(\frac{2\pi}{N}dq\right)\right). \tag{B.21}$$

However, when $d = N/2$, it is counted twice. To correct for this double counting, we subtract it once, resulting in:

$$N \text{ even}: \quad {}_1(q) = 2\sum_{m=1}^{\frac{N}{2}}\chi(d)\left(1 \quad \cos\left(\frac{2\pi}{N}dq\right)\right) \quad \chi\left(\frac{N}{2}\right)(1 \quad e^{i\pi q}), \tag{B.22}$$

which is exactly Eq. (7.18). A similar analysis for odd N gives Eq. (7.19). These are the results appearing in Sec. 7.3.

Appendix C

Dynamical realisation of a Powers of Two (PWR2) graph

In this section, we briefly outline how to dynamically generate a PWR2 sparse coupling graph as introduced in Sec. 5.3 and Sec. 7.2, following a method similar to that described in Sec. 7.4 for the hypercube. The general setup is shown schematically in Fig. 7.6(a).

We propose an iterative reshuffling of the atomic qubits, followed by global rotations, and stroboscopic nearest-neighbour interactions according to Eq. (7.31). For the shuffling procedure, we envisage a one-dimensional arrangement of the atoms (although other geometries are also possible) with nearest-neighbour interactions [1]. Fig. C.1 illustrates the entire protocol for a system of $N = 16$ atoms, with $\log_2(N) = 4$ shuffling stages. After nearest-neighbour Ising interactions (and local rotations) are applied according to Eq. (7.30) at stage m, each chain is split into two subchains comprising the odd and even sites, respectively. These subchains are then spatially separated to avoid any interactions with each other, and form the new chain layout for stage $m + 1$. In this way, at each iteration step $m = 0, 1, \ldots, \log_2(N) \quad 1$, couplings between atoms separated by a distance $d = 2^m$ are implemented (mathematically given by the Hamiltonian H_m).

[1] If periodic boundary conditions are applied, the atoms would need to be arranged in a circular configuration.

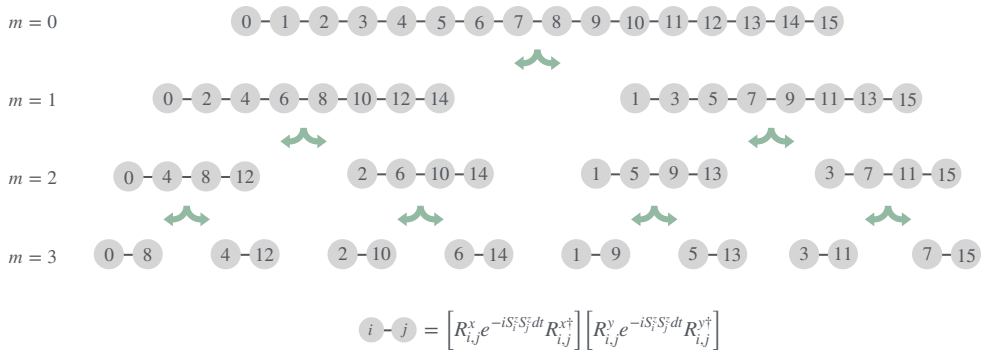

Figure C.1: **PWR2 Graph Using Dynamical Shuffling Operations.** Shuffling proposal to dynamically realise a PWR2 coupling graph using neutral atoms (grey circles) in tweezer arrays, shown schematically here for $N = 16$ atoms. At each stage m, the atoms are excited to the Rydberg state and interact strongly (black lines connecting neighboring atoms) if they are within each other's blockade radius (in this case, only nearest neighbors). Each chain is then split into two subchains (even and odd sites, respectively), as indicated by the green arrows, yielding the new chain layout for stage $m+1$. The interaction Hamiltonian is applied in $\log_2(N)$ steps, effectively implementing a first-order Trotter decomposition of the spin-interaction Hamiltonian as given in Eq. (7.31).

After the final shuffling stage, the atoms are brought back into the original layout from stage $m = 0$, completing one full time step in the evolution under the PWR2 coupling geometry.

Bibliography

[1] A. P. Luca D'Alessio, Yariv Kafri and M. Rigol, *From quantum chaos and eigenstate thermalization to statistical mechanics and thermodynamics,* Advances in Physics **65**, 239 (2016).

[2] J. M. Deutsch, *Eigenstate thermalization hypothesis,* Reports on Progress in Physics **81**, 082001 (2018).

[3] R. Nandkishore and D. A. Huse, *Many-Body Localization and Thermalization in Quantum Statistical Mechanics,* Annual Review of Condensed Matter Physics **6**, 15–38 (2015).

[4] R. P. Feynman, *Simulating physics with computers,* International Journal of Theoretical Physics **21**, 467 (1982).

[5] P. Shor, in *Proceedings 35th Annual Symposium on Foundations of Computer Science* (1994) pp. 124–134.

[6] R. Jozsa and N. Linden, *On the role of entanglement in quantum-computational speed-up,* Proceedings of the Royal Society of London. Series A: Mathematical, Physical and Engineering Sciences **459**, 2011–2032 (2003).

[7] M. A. Nielsen and I. L. Chuang, *Quantum Computation and Quantum Information* (Cambridge University Press, 2001).

[8] M. Kitagawa and M. Ueda, *Squeezed spin states,* Physical Review A **47**, 5138 (1993).

[9] D. J. Wineland, J. J. Bollinger, W. M. Itano, and D. J. Heinzen, *Squeezed atomic states and projection noise in spectroscopy,* Physical Review A **50**, 67 (1994).

[10] C. W. Helstrom, *Quantum Detection and Estimation Theory,* Journal of Statistical Physics **1**, 231 (1969).

[11] M. J. Holland and K. Burnett, *Interferometric detection of optical phase shifts at the Heisenberg limit,* Physical Review Letters **71**, 1355 (1993).

[12] L. Maccone, *Intuitive reason for the usefulness of entanglement in quantum metrology,* Physical Review A **88**, 042109 (2013).

[13] L. Pezzè, A. Smerzi, M. K. Oberthaler, R. Schmied, and P. Treutlein, *Quantum metrology with nonclassical states of atomic ensembles,* Reviews of Modern Physics **90**, 035005 (2018).

[14] L. Pezze and A. Smerzi, *Entanglement, nonlinear dynamics, and the Heisenberg limit,* Physical Review Letters **102**, 100401 (2009).

[15] Y. Sekino and L. Susskind, *Fast Scramblers,* J. High Energy Phys. **2008**, 065 (2008).

[16] P. Hayden and J. Preskill, *Black holes as mirrors: quantum information in random subsystems,* J. High Energy Phys. **2007**, 120 (2007).

[17] D. N. Page, *Average Entropy of a Subsystem,* Physical Review Letters **71**, 1291 (1993).

[18] D. N. Page, *Information in black hole radiation,* Physical Review Letters **71**, 3743–3746 (1993).

[19] J. Preskill, Quantum computing and the entanglement frontier, (2012), arXiv:1203.5813 [quant-ph] .

[20] N. Lashkari, D. Stanford, M. Hastings, T. Osborne, and P. Hayden, *Towards the fast scrambling conjecture,* J. High Energ. Phys. **2013**, 22 (2013).

[21] P. Hosur, X. L. Qi, D. A. Roberts, and B. Yoshida, *Chaos in Quantum Channels,* Journal of High Energy Physics **2016**, 1 (2016).

[22] C. E. Shannon, *A mathematical theory of communication,* Bell System Technical Journal **27**, 379 (1948).

[23] E. Knill, *Quantum Computing with Very Noisy Devices,* Nature **434**, 39 (2005).

[24] J. I. Cirac and P. Zoller, *Goals and Opportunities in Quantum Simulation,* Nature Physics **8**, 264 (2012).

[25] E. Altman, K. R. Brown, G. Carleo, L. D. Carr, E. Demler, C. Chin, B. DeMarco, S. E. Economou, M. A. Eriksson, K.-M. C. Fu, M. Greiner, K. R. Hazzard, R. G. Hulet, A. J. Kollár, B. L. Lev, *et al.*, *Quantum Simulators: Architectures and Opportunities,* PRX Quantum **2**, 017003 (2021).

[26] S. Flannigan, N. Pearson, G. H. Low, A. Buyskikh, I. Bloch, P. Zoller, M. Troyer, and A. J. Daley, *Propagation of Errors and Quantitative Quantum Simulation with Quantum Advantage,* Quantum Science and Technology **7**, 045025 (2022).

[27] A. J. Daley, I. Bloch, C. Kokail, S. Flannigan, N. Pearson, M. Troyer, and P. Zoller, *Practical Quantum Advantage in Quantum Simulation,* Nature **607**, 667 (2022).

[28] E. H. Lieb and D. W. Robinson, *The finite group velocity of quantum spin systems,* Communications in Mathematical Physics **28**, 251 (1972).

[29] N. Y. Yao, F. Grusdt, B. Swingle, M. D. Lukin, D. M. Stamper-Kurn, J. E. Moore, and E. A. Demler, *Interferometric Approach to Probing Fast Scrambling,* arXiv-quant-ph (2016).

[30] G. Bentsen, T. Hashizume, A. S. Buyskikh, E. J. Davis, A. J. Daley, S. S. Gubser, and M. Schleier-Smith, *Treelike Interactions and Fast Scrambling with Cold Atoms,* Physical Review Letters **123**, 130601 (2019).

[31] J. Marino and A. M. Rey, *Cavity-QED simulator of slow and fast scrambling,* Physical Review A **99**, 051803 (2019).

[32] G. Bentsen, Y. Gu, and A. Lucas, *Fast Scrambling on Sparse Graphs,* Proceedings of the National Academy of Sciences **116**, 6689 (2019).

[33] Z. Li, S. Choudhury, and W. V. Liu, *Fast scrambling without appealing to holographic duality,* Physical Review Research **2**, 043399 (2020).

[34] R. Belyansky, P. Bienias, Y. A. Kharkov, A. V. Gorshkov, and B. Swingle, *Minimal Model for Fast Scrambling,* Physical Review Letters **125**, 130601 (2020).

[35] T. Hashizume, G. S. Bentsen, S. Weber, and A. J. Daley, *Deterministic Fast Scrambling with Neutral Atom Arrays,* Physical Review Letters **126**, 200603 (2021).

[36] L. Susskind, L. Thorlacius, and J. Uglum, *The stretched horizon and black hole complementarity,* Physical Review D **48**, 3743–3761 (1993).

[37] S. Sachdev and J. Ye, *Gapless spin-fluid ground state in a random quantum Heisenberg magnet,* Physical Review Letters **70**, 3339 (1993).

[38] A. Kitaev, A Simple Model of Quantum Holography: KITP Program- Entanglement in Strongly-Correlated Quantum Matter, (2015).

[39] J. Maldacena and D. Stanford, *Remarks on the Sachdev-Ye-Kitaev model,* Physical Review D **94**, 106002 (2016).

[40] J. Kim, E. Altman, and X. Cao, *Dirac fast scramblers,* Physical Review B **103**, L081113 (2021).

[41] S. Sachdev, *Bekenstein-Hawking entropy and strange metals,* Physical Review X **5**, 041025 (2015).

[42] T. Hashizume, S. Kuriyattil, A. J. Daley, and G. Bentsen, *Tunable Geometries in Sparse Clifford Circuits,* Symmetry **14**, 666 (2022).

[43] G. S. Bentsen, T. Hashizume, E. J. Davis, A. S. Buyskikh, M. H. Schleier-Smith, and A. J. Daley, in *Optical, Opto-Atomic, and Entanglement-Enhanced Precision*

Metrology II, Vol. 11296, International Society for Optics and Photonics (SPIE, 2020) p. 112963W.

[44] S. Kuriyattil, T. Hashizume, G. Bentsen, and A. J. Daley, *Onset of Scrambling as a Dynamical Transition in Tunable-Range Quantum Circuits,* PRX Quantum **4**, 030325 (2023).

[45] S. S. Gubser, C. Jepsen, Z. Ji, and B. Trundy, *Continuum Limits of Sparse Coupling Patterns,* Physical Review D **98**, 045009 (2018).

[46] J. Cirac and P. Zoller, *A scalable quantum computer with ions in an array of microtraps,* Nature **404**, 579 (2000).

[47] J. I. Cirac and P. Zoller, *Quantum Computations with Cold Trapped Ions,* Physical Review Letters **74**, 4091 (1995).

[48] T. Manovitz, Y. Shapira, N. Akerman, A. Stern, and R. Ozeri, *Quantum Simulations with Complex Geometries and Synthetic Gauge Fields in a Trapped Ion Chain,* PRX Quantum **1**, 020303 (2020).

[49] C.-L. Hung, A. González-Tudela, J. I. Cirac, and H. J. Kimble, *Quantum spin dynamics with pairwise-tunable, long-range interactions,* Proceedings of the National Academy of Sciences **113**, E4946 (2016).

[50] M. K. Joshi, A. Elben, B. Vermersch, T. Brydges, C. Maier, P. Zoller, R. Blatt, and C. F. Roos, *Quantum Information Scrambling in a Trapped-Ion Quantum Simulator with Tunable Range Interactions,* Physical Review Letters **124**, 240505 (2020).

[51] M. Gärttner, J. G. Bohnet, A. Safavi-Naini, M. L. Wall, J. J. Bollinger, and A. M. Rey, *Measuring out-of-time-order correlations and multiple quantum spectra in a trapped-ion quantum magnet,* Nature Physics **13**, 781 (2017).

[52] J. I. Cirac and P. Zoller, *Goals and opportunities in quantum simulation with trapped ions,* Nature **404**, 579 (2000).

[53] D. Bluvstein, H. Levine, G. Semeghini, T. T. Wang, S. Ebadi, M. Kalinowski, A. Keesling, N. Maskara, H. Pichler, M. Greiner, V. Vuletić, and M. D. Lukin, *A quantum processor based on coherent transport of entangled atom arrays,* Nature **604**, 451 (2022).

[54] H. Bernien, S. Schwartz, A. Keesling, H. Levine, A. Omran, H. Pichler, S. Choi, A. S. Zibrov, M. Endres, M. Greiner, *et al.*, *Probing many-body dynamics on a 51-atom quantum simulator,* Nature **551**, 579 (2017).

[55] D. Jaksch, J. I. Cirac, P. Zoller, S. L. Rolston, R. Côté, and M. D. Lukin, *Fast Quantum Gates for Neutral Atoms,* Physical Review Letters **85**, 2208 (2000).

[56] A. Browaeys and T. Lahaye, *Many-body physics with individually controlled Rydberg atoms,* Nature Physics **16**, 132 (2020).

[57] G. Semeghini, H. Levine, A. Keesling, S. Ebadi, T. T. Wang, D. Bluvstein, R. Verresen, H. Pichler, M. Kalinowski, R. Samajdar, A. Omran, S. Sachdev, A. Vishwanath, M. Greiner, V. Vuletić, and M. D. Lukin, *Probing topological spin liquids on a programmable quantum simulator,* Science **374**, 1242 (2021).

[58] H. Levine, A. Keesling, G. Semeghini, A. Omran, T. T. Wang, S. Ebadi, H. Bernien, M. Greiner, V. Vuletić, H. Pichler, and M. D. Lukin, *Parallel Implementation of High-Fidelity Multiqubit Gates with Neutral Atoms,* Physical Review Letters **123**, 170503 (2019).

[59] A. Periwal, E. S. Cooper, P. Kunkel, J. F. Wienand, E. J. Davis, and M. Schleier-Smith, *Programmable interactions and emergent geometry in an array of atom clouds,* Nature **600**, 630 (2021).

[60] E. J. Davis, G. Bentsen, L. Homeier, T. Li, and M. H. Schleier-Smith, *Photon-Mediated Spin-Exchange Dynamics of Spin-1 Atoms,* Physical Review Letters **122**, 010405 (2019).

[61] H. Ritsch, P. Domokos, F. Brennecke, and T. Esslinger, *Cold atoms in cavity-generated dynamical optical potentials,* Rev. Mod. Phys. **85**, 553 (2013).

[62] K. Baumann, C. Guerlin, F. Brennecke, and T. Esslinger, *Dicke quantum phase transition with a superfluid gas in an optical cavity,* Nature **464**, 1301–1306 (2010).

[63] B. E. Kane, *A silicon-based nuclear spin quantum computer,* Nature **393**, 133 (1998).

[64] D. D. Awschalom, L. C. Bassett, A. S. Dzurak, E. L. Hu, and J. R. Petta, *Quantum Spintronics: Engineering and Manipulating Atom-Like Spins in Semiconductors,* Science **339**, 1174 (2013).

[65] M. G. Dutt, L. Childress, L. Jiang, E. Togan, J. Maze, F. Jelezko, A. Zibrov, P. R. Hemmer, and M. Lukin, *Quantum register based on individual electronic and nuclear spin qubits in diamond,* Science **316**, 1312 (2007).

[66] D. Loss and D. P. DiVincenzo, *Quantum computation with quantum dots,* Physical Review A **57**, 120 (1998).

[67] G. K. Brennen, C. M. Caves, P. S. Jessen, and I. H. Deutsch, *Quantum Logic Gates in Optical Lattices,* Physical Review Letters **82**, 1060 (1999).

[68] D. Jaksch, J. I. Cirac, P. Zoller, S. L. Rolston, R. Côté, and M. D. Lukin, *Fast Quantum Gates for Neutral Atoms,* Physical Review Letters **85**, 2208 (2000).

[69] E. Brion, K. Mølmer, and M. Saffman, *Quantum Computing with Collective Ensembles of Multilevel Systems,* Physical Review Letters **99**, 260501 (2007).

[70] K. Mølmer, L. Isenhower, and M. Saffman, *Efficient grover search with Rydberg blockade,* Journal of Physics B: Atomic, Molecular and Optical Physics **44**, 184016 (2011).

[71] M. Saffman, *Quantum computing with atomic qubits and Rydberg interactions: progress and challenges,* Journal of Physics B: Atomic, Molecular and Optical Physics **49**, 202001 (2016).

[72] L. Henriet, L. Beguin, A. Signoles, T. Lahaye, A. Browaeys, G.-O. Reymond, and C. Jurczak, *Quantum computing with neutral atoms,* Quantum **4**, 327 (2020).

[73] C. S. Adams, J. D. Pritchard, and J. P. Shaffer, *Rydberg atom quantum technologies,* Journal of Physics B: Atomic, Molecular and Optical Physics **53**, 012002 (2019).

[74] I. Cong, H. Levine, A. Keesling, D. Bluvstein, S.-T. Wang, and M. D. Lukin, *Hardware-efficient, fault-tolerant quantum computation with Rydberg atoms,* Physical Review X **12**, 021049 (2022).

[75] A. Omran, H. Levine, A. Keesling, G. Semeghini, T. T. Wang, S. Ebadi, H. Bernien, A. S. Zibrov, H. Pichler, S. Choi, J. Cui, M. Rossignolo, P. Rembold, S. Montangero, T. Calarco, M. Endres, M. Greiner, V. Vuletić, and M. D. Lukin, *Generation and manipulation of schrödinger cat states in Rydberg atom arrays,* Science **365**, 570 (2019).

[76] R. Verresen, M. D. Lukin, and A. Vishwanath, *Prediction of toric code topological order from Rydberg blockade,* Physical Review X **11**, 031005 (2021).

[77] E. Schrödinger and A. Einstein, *The Collected Papers of Albert Einstein, Volume 5: The Swiss Years: Correspondence, 1902-1914*, edited by J. Stachel, D. C. Cassidy, and R. Schulmann (Princeton University Press, Princeton, 1995) pp. 152–154, letter from Schrödinger to Einstein, dated 19 August 1935.

[78] A. Einstein, B. Podolsky, and N. Rosen, *Can Quantum-Mechanical Description of Physical Reality Be Considered Complete?* Phys. Rev. **47**, 777 (1935).

[79] R. Clausius, *Ueber die bewegende Kraft der Wärme und die Gesetze, welche sich daraus für die Wärmelehre selbst ableiten lassen,* Annalen der Physik **155**, 368 (1850).

[80] L. Boltzmann, *Vorlesungen über die Gastheorie*, Vol. 1 (Johann Ambrosius Barth, Leipzig, 1896).

[81] J. von Neumann, *Mathematical Foundations of Quantum Mechanics* (Princeton University Press, 1955).

[82] J. W. Britton, B. C. Sawyer, A. C. Keith, C.-C. J. Wang, J. K. Freericks, H. Uys, M. J. Biercuk, and J. J. Bollinger, *Engineered two-dimensional Ising interactions in a trapped-ion quantum simulator with hundreds of spins,* Nature **484**, 489–492 (2012).

[83] I. M. Georgescu, S. Ashhab, and F. Nori, *Quantum simulation,* Rev. Mod. Phys. **86**, 153 (2014).

[84] C. H. Bennett, G. Brassard, C. Crépeau, R. Jozsa, A. Peres, and W. K. Wootters, *Teleporting an unknown quantum state via dual classical and Einstein-Podolsky-Rosen channels,* Physical Review Letters **70**, 1895 (1993).

[85] D. Deutsch, *Quantum theory, the Church–Turing principle and the universal quantum computer,* Proceedings of the Royal Society of London. Series A, Mathematical and Physical Sciences **400**, 97 (1985).

[86] A. Kitaev, *Fault-tolerant quantum computation by anyons,* Annals of Physics **303**, 2–30 (2003).

[87] D. Gioev and I. Klich, *Entanglement Entropy of Fermions in Any Dimension and the Widom Conjecture,* Physical Review Letters **96**, 100503 (2006).

[88] M. M. Wolf, *Violation of the Entropic Area Law for Fermions,* Physical Review Letters **96**, 010404 (2006).

[89] M. B. Hastings and T. Koma, *Spectral Gap and Exponential Decay of Correlations,* Commun. Math. Phys. **265**, 781 (2006).

[90] G. Vidal, *Entanglement Renormalization,* Physical Review Letters **99**, 220405 (2007).

[91] M. B. Hastings, *An area law for one-dimensional quantum systems,* Journal of Statistical Mechanics: Theory and Experiment **2007**, P08024 (2007).

[92] J. Eisert, M. Cramer, and M. B. Plenio, *Colloquium: Area laws for the entanglement entropy,* Rev. Mod. Phys. **82**, 277 (2010).

[93] E. Bianchi, L. Hackl, M. Kieburg, M. Rigol, and L. Vidmar, *Volume-Law Entanglement Entropy of Typical Pure Quantum States,* PRX Quantum **3**, 030201 (2022).

[94] S. Sachdev, *Quantum Phase Transitions* (Wiley Online Library, Hoboken, NJ, 2007).

[95] D. V. Else, F. Machado, C. Nayak, and N. Y. Yao, *Improved Lieb-Robinson bound for many-body Hamiltonians with power-law interactions,* Physical Review A **101**, 022333 (2020).

[96] M. C. Tran, A. Y. Guo, C. L. Baldwin, A. Ehrenberg, A. V. Gorshkov, and A. Lucas, *Lieb-Robinson Light Cone for Power-Law Interactions,* Physical Review Letters **127**, 160401 (2021).

[97] B. Nachtergaele and R. Sims, *Lieb-Robinson Bounds and the Exponential Clustering Theorem,* Communications in Mathematical Physics **265**, 119 (2006).

[98] B. Nachtergaele and R. Sims, Lieb-Robinson bounds in quantum many-body physics, (2010).

[99] M. J. Gullans and D. A. Huse, *Dynamical purification phase transitions induced by quantum measurements,* Physical Review X **10**, 041020 (2020).

[100] A. Kitaev and J. Preskill, *Topological Entanglement Entropy,* Physical Review Letters **96**, 110404 (2006).

[101] P. Hayden, M. Headrick, and A. Maloney, *Holographic mutual information is monogamous,* Physical Review D **87**, 046003 (2013).

[102] A. Seshadri, V. Madhok, and A. Lakshminarayan, *Tripartite mutual information, entanglement, and scrambling in permutation symmetric systems with an application to quantum chaos,* Physical Review E **98**, 052205 (2018).

[103] M. Rota, *Tripartite information of highly entangled states,* Journal of High Energy Physics **2016**, 75 (2016).

[104] M. Rangamani and M. Rota, *Entanglement structures in qubit systems,* Journal of Physics A: Mathematical and Theoretical **48**, 385301 (2015).

[105] A. Zabalo, M. J. Gullans, J. H. Wilson, S. Gopalakrishnan, D. A. Huse, and J. H. Pixley, *Critical properties of the measurement-induced transition in random quantum circuits,* Physical Review B **101**, 060301 (2020).

[106] S. Ryu and T. Takayanagi, *Holographic Derivation of Entanglement Entropy from the anti–de Sitter Space/Conformal Field Theory Correspondence,* Physical Review Letters **96**, 181602 (2006).

[107] J. Maldacena, *The Large-N Limit of Superconformal Field Theories and Supergravity,* International Journal of Theoretical Physics **38**, 1113 (1999).

[108] E. Iyoda and T. Sagawa, *Scrambling of Quantum Information in Quantum Many-Body Systems,* Physical Review A **97**, 042330 (2018).

[109] S. Strogatz, *Nonlinear Dynamics and Chaos: With Applications to Physics, Biology, Chemistry, and Engineering*, 2nd ed. (Westview Press, a member of the Perseus Books Group, 2015).

[110] E. P. Wigner, *Characteristic Vectors of Bordered Matrices With Infinite Dimensions,* Annals of Mathematics **62**, 548 (1955).

[111] T. Guhr, A. Müller–Groeling, and H. A. Weidenmüller, *Random-matrix theories in quantum physics: common concepts,* Physics Reports **299**, 189 (1998).

[112] S. Wimberger, *Nonlinear Dynamics and Quantum Chaos: An Introduction*, 1st ed., Graduate Texts in Physics (Springer Cham, 2014).

[113] D. Poilblanc, T. Ziman, J. Bellissard, F. Mila, and G. Montambaux, *Poisson vs. GOE statistics in integrable and non-integrable quantum hamiltonians,* Europhysics Letters **22**, 537 (1993).

[114] O. Bohigas, M. J. Giannoni, and C. Schmit, *Characterization of Chaotic Quantum Spectra and Universality of Level Fluctuation Laws,* Physical Review Letters **52**, 1 (1984).

[115] M. V. Berry and M. Tabor, *Level clustering in the regular spectrum,* Proceedings of the Royal Society of London. Series A. Mathematical and Physical Sciences **356**, 375 (1977).

[116] M. V. Berry, *Regular and irregular semiclassical wavefunctions,* Journal of Physics A: Mathematical and General **10**, 2083 (1977).

[117] J. M. Deutsch, *Quantum statistical mechanics in a closed system,* Physical Review A **43**, 2046 (1991).

[118] M. Srednicki, *Chaos and quantum thermalization,* Physical Review E **50**, 888 (1994).

[119] M. Srednicki, *The approach to thermal equilibrium in quantized chaotic systems,* Journal of Physics A: Mathematical and General **32**, 1163 (1999).

[120] M. Srednicki, *Thermal fluctuations in quantized chaotic systems,* Journal of Physics A: Mathematical and General **29**, L75 (1996).

[121] M. Haque, P. A. McClarty, and I. M. Khaymovich, *Entanglement of midspectrum eigenstates of chaotic many-body systems: Reasons for deviation from random ensembles,* Physical Review E **105**, 014109 (2022).

[122] M. Rigol, V. Dunjko, V. Yurovsky, and M. Olshanii, *Relaxation in a Completely Integrable Many-Body Quantum System: An Ab Initio Study of the Dynamics of the Highly Excited States of 1D Lattice Hard-Core Bosons,* Physical Review Letters **98**, 050405 (2007).

[123] A. S. L. Malabarba, L. P. García-Pintos, N. Linden, T. C. Farrelly, and A. J. Short, *Quantum systems equilibrate rapidly for most observables,* Physical Review E **90**, 012121 (2014).

[124] N. Linden, S. Popescu, A. J. Short, and A. Winter, *Quantum mechanical evolution towards thermal equilibrium,* Physical Review E **79**, 061103 (2009).

[125] P. Reimann, *Canonical thermalization,* New Journal of Physics **12**, 055027 (2010).

[126] S. H. Shenker and D. Stanford, *Black holes and the butterfly effect,* Journal of High Energy Physics **2014**, 67 (2014).

[127] J. Maldacena, S. H. Shenker, and D. Stanford, *A Bound on Chaos,* Journal of High Energy Physics **2016**, 106 (2016).

[128] B. Swingle, G. Bentsen, M. Schleier-Smith, and P. Hayden, *Measuring the Scrambling of Quantum Information,* Physical Review A **94**, 040302 (2016).

[129] D. A. Roberts and B. Swingle, *Lieb-Robinson Bound and the Butterfly Effect in Quantum Field Theories,* Physical Review Letters **117**, 091602 (2016).

[130] B. Swingle, *Unscrambling the physics of out-of-time-order correlators,* Nature Physics **14**, 988 (2018).

[131] L. Foini and J. Kurchan, *Eigenstate thermalization hypothesis and out of time order correlators,* Physical Review E **99**, 042139 (2019).

[132] C. Sünderhauf, L. Piroli, X.-L. Qi, N. Schuch, and J. I. Cirac, *Quantum chaos in the Brownian SYK model with large finite N : OTOCs and tripartite information,* Journal of High Energy Physics **2019**, 38 (2019).

[133] S. Xu and B. Swingle, *Accessing Scrambling Using Matrix Product Operators,* Nature Physics **16**, 199 (2020).

[134] S. Pappalardi, A. Russomanno, B. Žunkovič, F. Iemini, A. Silva, and R. Fazio, *Scrambling and entanglement spreading in long-range spin chains,* Physical Review B **98**, 134303 (2018).

[135] S. Pilatowsky-Cameo, J. Chávez-Carlos, M. A. Bastarrachea-Magnani, P. Stránský, S. Lerma-Hernández, L. F. Santos, and J. G. Hirsch, *Positive quantum Lyapunov exponents in experimental systems with a regular classical limit,* Physical Review E **101**, 010202 (2020).

[136] K. Hashimoto, K.-B. Huh, K. K. Kim, and P. Yi, *Exponential growth of out-of-time-order correlator without chaos: inverted harmonic oscillator,* Journal of High Energy Physics **2020**, 68 (2020).

[137] T. Xu, T. Scaffidi, and X. Cao, *Does Scrambling Equal Chaos?* Physical Review Letters **124**, 140602 (2020).

[138] N. Dowling, P. Kos, and K. Modi, *Scrambling Is Necessary but Not Sufficient for Chaos,* Physical Review Letters **131**, 180403 (2023).

[139] A. Nahum, J. Ruhman, S. Vijay, and J. Haah, *Quantum Entanglement Growth under Random Unitary Dynamics,* Physical Review X **7**, 031016 (2017).

[140] A. Nahum, S. Vijay, and J. Haah, *Operator Spreading in Random Unitary Circuits,* Physical Review X **8**, 021014 (2018).

[141] B. P. Abbott, R. Abbott, T. Abbott, M. Abernathy, F. Acernese, K. Ackley, C. Adams, T. Adams, P. Addesso, R. Adhikari, and et al., *Observation of Gravitational Waves from a Binary Black Hole Merger,* Physical Review Letters **116**, 061102 (2016).

[142] A. A. Oglat, M. Z. Matjafri, N. Suardi, M. A. Oqlat, M. A. Abdelrahman, and A. A. Oqlat, *A Review of Medical Doppler Ultrasonography of Blood Flow in General and Especially in Common Carotid Artery,* Journal of Medical Ultrasound **26**, 3 (2018).

[143] S. M. Kay, *Fundamentals of statistical signal processing: estimation theory* (Prentice-Hall, Inc., USA, 1993).

[144] D. J. Sheskin, *Handbook of Parametric and Nonparametric Statistical Procedures* (Chapman and Hall/CRC, Boca Raton, 2003).

[145] A. Holevo, *Probabilistic and Statistical Aspects of Quantum Theory*, Publications of the Scuola Normale Superiore No. 1 (Edizioni della Normale Pisa, Pisa, 2011).

[146] J. M. Taylor, P. Cappellaro, L. Childress, L. Jiang, D. Budker, P. R. Hemmer, A. Yacoby, R. Walsworth, and M. D. Lukin, *High-sensitivity diamond magnetometer with nanoscale resolution,* Nature Physics **4**, 810–816 (2008).

[147] W. Wasilewski, K. Jensen, H. Krauter, J. J. Renema, M. V. Balabas, and E. S. Polzik, *Quantum Noise Limited and Entanglement-Assisted Magnetometry,* Physical Review Letters **104**, 133601 (2010).

[148] R. J. Sewell, M. Koschorreck, M. Napolitano, B. Dubost, N. Behbood, and M. W. Mitchell, *Magnetic Sensitivity Beyond the Projection Noise Limit by Spin Squeezing,* Physical Review Letters **109**, 253605 (2012).

[149] L. Razzoli, L. Ghirardi, I. Siloi, P. Bordone, and M. G. A. Paris, *Lattice quantum magnetometry,* Physical Review A **99**, 062330 (2019).

[150] P. Neumann, I. Jakobi, F. Dolde, C. Burk, R. Reuter, G. Waldherr, J. Honert, T. Wolf, A. Brunner, J. H. Shim, D. Suter, H. Sumiya, J. Isoya, and J. Wrachtrup, *High-Precision Nanoscale Temperature Sensing Using Single Defects in Diamond,* Nano Letters **13**, 2738–2742 (2013).

[151] D. M. Toyli, C. F. de las Casas, D. J. Christle, V. V. Dobrovitski, and D. D. Awschalom, *Fluorescence thermometry enhanced by the quantum coherence of single spins in diamond,* Proceedings of the National Academy of Sciences of the United States of America **110**, 8417 (2013).

[152] L. A. Correa, M. Mehboudi, G. Adesso, and A. Sanpera, *Individual Quantum Probes for Optimal Thermometry,* Physical Review Letters **114**, 220405 (2015).

[153] V. Giovannetti, S. Lloyd, and L. Maccone, *Quantum-enhanced positioning and clock synchronization,* Nature **412**, 417–419 (2001).

[154] J. Appel, P. J. Windpassinger, D. Oblak, U. B. Hoff, N. Kjærgaard, and E. S. Polzik, *Mesoscopic atomic entanglement for precision measurements beyond the standard quantum limit,* Proceedings of the National Academy of Sciences **106**, 10960–10965 (2009).

[155] A. D. Ludlow, M. M. Boyd, J. Ye, E. Peik, and P. O. Schmidt, *Optical atomic clocks,* Rev. Mod. Phys. **87**, 637 (2015).

[156] M. Schioppo, R. C. Brown, W. F. McGrew, N. Hinkley, R. J. Fasano, K. Beloy, T. H. Yoon, G. Milani, D. Nicolodi, J. A. Sherman, N. B. Phillips, C. W. Oates, and A. D. Ludlow, *Ultrastable optical clock with two cold-atom ensembles,* Nature Photonics **11**, 48–52 (2016).

[157] J. Ma, X. Wang, C. P. Sun, and F. Nori, *Quantum spin squeezing,* Physics Reports **509**, 89 (2011).

[158] V. Meyer, M. A. Rowe, D. Kielpinski, C. A. Sackett, W. M. Itano, C. Monroe, and D. J. Wineland, *Experimental Demonstration of Entanglement-Enhanced Rotation Angle Estimation Using Trapped Ions,* Physical Review Letters **86**, 5870 (2001).

[159] J. G. Bohnet, B. C. Sawyer, J. W. Britton, M. L. Wall, A. M. Rey, M. Foss-Feig, and J. J. Bollinger, *Quantum spin dynamics and entanglement generation with hundreds of trapped ions,* Science **352**, 1297 (2016).

[160] G. Bornet, G. Emperauger, C. Chen, B. Ye, M. Block, M. Bintz, J. A. Boyd, D. Barredo, T. Comparin, F. Mezzacapo, T. Roscilde, T. Lahaye, N. Y. Yao, and A. Browaeys, *Scalable spin squeezing in a dipolar Rydberg atom array,* Nature **621**, 728–733 (2023).

[161] J. A. Hines, S. V. Rajagopal, G. L. Moreau, M. D. Wahrman, N. A. Lewis, O. Marković, and M. Schleier-Smith, *Spin squeezing by Rydberg dressing in an array of atomic ensembles,* Physical Review Letters **131**, 063401 (2023).

[162] W. J. Eckner, N. Darkwah Oppong, A. Cao, A. W. Young, W. R. Milner, J. M. Robinson, J. Ye, and A. M. Kaufman, *Realizing spin squeezing with Rydberg interactions in an optical clock,* Nature **621**, 734–739 (2023).

[163] R. Kaubruegger, P. Silvi, C. Kokail, R. van Bijnen, A. M. Rey, J. Ye, A. M. Kaufman, and P. Zoller, *Variational Spin-Squeezing Algorithms on Programmable Quantum Sensors,* Physical Review Letters **123**, 260505 (2019).

[164] R. Kaubruegger, D. V. Vasilyev, M. Schulte, K. Hammerer, and P. Zoller, *Quantum Variational Optimization of Ramsey Interferometry and Atomic Clocks,* Physical Review X **11**, 041045 (2021).

[165] C. D. Marciniak, T. Feldker, I. Pogorelov, R. Kaubruegger, D. V. Vasilyev, R. van Bijnen, P. Schindler, P. Zoller, R. Blatt, and T. Monz, *Optimal metrology with programmable quantum sensors,* Nature **603**, 604 (2022).

[166] T.-X. Zheng, A. Li, J. Rosen, S. Zhou, M. Koppenhöfer, Z. Ma, F. T. Chong, A. A. Clerk, L. Jiang, and P. C. Maurer, *Preparation of metrological states in dipolar-interacting spin systems,* npj Quantum Information **8**, 150 (2022).

[167] N. Shettell, E. Kashefi, and D. Markham, *Cryptographic approach to quantum metrology,* Phys. Rev. A **105**, L010401 (2022).

[168] H. Cramér, *Mathematical Methods of Statistics* (Princeton University Press, Princeton, 1946).

[169] R. A. Fisher, *Theory of Statistical Estimation,* Mathematical Proceedings of the Cambridge Philosophical Society **22**, 700 (1925).

[170] S. L. Braunstein and C. M. Caves, *Statistical Distance and the Geometry of Quantum States,* Physical Review Letters **72**, 3439 (1994).

[171] J. Huang, S. Wu, H. Zhong, and C. Lee, QUANTUM METROLOGY WITH COLD ATOMS, in *Annual Review of Cold Atoms and Molecules* (WORLD SCIENTIFIC, 2014) Chap. CHAPTER 7, pp. 365–415.

[172] L. Pezze' and A. Smerzi, Quantum theory of phase estimation, (2014).

[173] R. H. Dicke, *Coherence in Spontaneous Radiation Processes,* Phys. Rev. **93**, 99 (1954).

[174] K. Hepp and E. H. Lieb, *On the Superradiant Phase Transition for Molecules in a Radiation Field,* Physical Review A **8**, 2517 (1973).

[175] J. G. Bohnet, H. Schempp, J. I. Zhang, *et al.*, *Quantum Spin Dynamics with Real-Time Feedback,* Physical Review Letters **116**, 123601 (2016).

[176] P. Kirton, M. M. Roses, J. Keeling, and E. G. Dalla Torre, *Introduction to the Dicke Model: From Equilibrium to Nonequilibrium, and Vice Versa,* Advanced Quantum Technologies **2**, 1800043 (2018).

[177] W.-M. Zhang, D. H. Feng, and R. Gilmore, *Coherent states: Theory and some applications,* Rev. Mod. Phys. **62**, 867 (1990).

[178] F. T. Arecchi, E. Courtens, R. Gilmore, and H. Thomas, *Atomic Coherent States in Quantum Optics,* Physical Review A **6**, 2211 (1972).

[179] J. M. Radcliffe, *Some Properties of Coherent Spin States,* Journal of Physics A: General Physics **4**, 313 (1971).

[180] National Institute of Informatics, Quantum Information Science Summer Lecture Notes, (2012), accessed: 2024-08-26.

[181] R. Schmied and P. Treutlein, *Tomographic reconstruction of the Wigner function on the bloch sphere,* New Journal of Physics **13**, 065019 (2011).

[182] R. McConnell, H. Zhang, J. Hu, S. Ćuk, and V. Vuletić, *Entanglement with negative Wigner function of almost 3,000 atoms heralded by one photon,* Nature **519**, 439–442 (2015).

[183] B. Koczor, R. Zeier, and S. J. Glaser, *Continuous phase-space representations for finite-dimensional quantum states and their tomography,* Physical Review A **101**, 022318 (2020).

[184] C. T. Lee, *Q representation of the atomic coherent states and the origin of fluctuations in superfluorescence,* Physical Review A **30**, 3308 (1984).

[185] C. Gross and I. Bloch, *Spin Squeezing in a Quantum Gas,* Science **336**, 1111 (2012).

[186] O. Gühne and G. Tóth, *Entanglement detection,* Physics Reports **474**, 1–75 (2009).

[187] L. Amico, R. Fazio, A. Osterloh, and V. Vedral, *Entanglement in many-body systems,* Rev. Mod. Phys. **80**, 517 (2008).

[188] R. Horodecki, P. Horodecki, M. Horodecki, and K. Horodecki, *Quantum entanglement,* Reviews of Modern Physics **81**, 865–942 (2009).

[189] G. Tóth, C. Knapp, O. Gühne, and H. J. Briegel, *Optimal Spin Squeezing Inequalities Detect Bound Entanglement in Spin Models,* Physical Review Letters **99**, 250405 (2007).

[190] L.-M. Duan, *Entanglement Detection in the Vicinity of Arbitrary Dicke States,* Physical Review Letters **107**, 180502 (2011).

[191] B. Lücke, J. Peise, G. Vitagliano, J. Arlt, L. Santos, G. Tóth, and C. Klempt, *Detecting Multiparticle Entanglement of Dicke States,* Physical Review Letters **112**, 155304 (2014).

[192] D. Ulam-Orgikh and M. Kitagawa, *Spin squeezing and decoherence limit in Ramsey spectroscopy,* Physical Review A **64**, 052106 (2001).

[193] A. Sørensen, L.-M. Duan, J. I. Cirac, and P. Zoller, *Many-particle entanglement with Bose–Einstein condensates,* Nature **409**, 63–66 (2001).

[194] P. Hyllus, O. Gühne, and A. Smerzi, *Not all pure entangled states are useful for sub-shot-noise interferometry,* Physical Review A **82**, 012337 (2010).

[195] D. Gottesman, *Theory of fault-tolerant quantum computation,* Physical Review A **57**, 127 (1998).

[196] S. Aaronson and D. Gottesman, *Improved simulation of stabilizer circuits,* Physical Review A **70** (2004), 10.1103/PhysRevA.70.052328.

[197] P. Selinger, *Generators and relations for n-qubit Clifford operators,* Logical Methods in Computer Science **11**, 80 (2015).

[198] A. Rényi, in *Proceedings of the Fourth Berkeley Symposium on Mathematical Statistics and Probability, Volume 1: Contributions to the Theory of Statistics*, Vol. 4 (University of California Press, 1961) pp. 547–562.

[199] D. Poulin, *Stabilizer Formalism for Operator Quantum Error Correction,* Physical Review Letters **95**, 230504 (2005).

[200] T. Hashizume, G. Bentsen, and A. J. Daley, *Measurement-induced phase transitions in sparse nonlocal scramblers,* Physical Review Research **4**, 013174 (2022).

[201] A. R. Arab, *Lecture Notes on Quantum Entanglement: From Stabilizer States to Stabilizer Channels,* Frontiers in Physics **19**, 51203 (2024).

[202] S. R. White, *Density matrix formulation for quantum renormalization groups,* Physical Review Letters **69**, 2863 (1992).

[203] A. J. Daley, C. Kollath, U. Schollwöck, and G. Vidal, *Time-dependent density-matrix renormalization-group using adaptive effective Hilbert spaces,* Journal of Statistical Mechanics: Theory and Experiment **2004**, P04005 (2004).

[204] U. Schollwöck, *The density-matrix renormalization group in the age of matrix product states,* Annals of Physics **326**, 96–192 (2011).

[205] F. Verstraete and J. I. Cirac, *Matrix product states represent ground states faithfully,* Physical Review B **73**, 094423 (2006).

[206] F. Verstraete, V. Murg, and J. Cirac, *Matrix product states, projected entangled pair states, and variational renormalization group methods for quantum spin systems,* Advances in Physics **57**, 143–224 (2008).

[207] D. Perez-Garcia, F. Verstraete, M. M. Wolf, and J. I. Cirac, *Matrix Product State Representations,* Quantum Info. Comput. **7**, 401–430 (2007).

[208] J. Haegeman, J. I. Cirac, T. J. Osborne, I. Pižorn, H. Verschelde, and F. Verstraete, *Time-Dependent Variational Principle for Quantum Lattices,* Physical Review Letters **107**, 070601 (2011).

[209] J. Haegeman, C. Lubich, I. Oseledets, B. Vandereycken, and F. Verstraete, *Unifying time evolution and optimization with matrix product states,* Physical Review B **94**, 165116 (2016).

[210] S. Paeckel, T. Köhler, A. Swoboda, S. R. Manmana, U. Schollwöck, and C. Hubig, *Time-evolution methods for matrix-product states,* Annals of Physics **411**, 167998 (2019).

[211] M. Yang and S. R. White, *Time-dependent variational principle with ancillary Krylov subspace,* Physical Review B **102**, 094315 (2020).

[212] J. Haegeman, T. J. Osborne, and F. Verstraete, *Post-matrix product state methods: To tangent space and beyond,* Physical Review B **88**, 075133 (2013).

[213] G. Evenbly and G. Vidal, *Tensor Network States and Geometry,* Journal of Statistical Physics **145**, 891–918 (2011).

[214] M. P. Zaletel, R. S. K. Mong, C. Karrasch, J. E. Moore, and F. Pollmann, *Time-evolving a matrix product state with long-ranged interactions,* Physical Review B **91**, 165112 (2015).

[215] G. Vidal, *Efficient Simulation of One-Dimensional Quantum Many-Body Systems,* Physical Review Letters **93**, 040502 (2004).

[216] S. R. White and A. E. Feiguin, *Real-Time Evolution Using the Density Matrix Renormalization Group,* Physical Review Letters **93**, 076401 (2004).

[217] F. Verstraete, J. J. García-Ripoll, and J. I. Cirac, *Matrix Product Density Operators: Simulation of Finite-Temperature and Dissipative Systems,* Physical Review Letters **93**, 207204 (2004).

[218] T. Hashizume, J. C. Halimeh, and I. P. McCulloch, *Hybrid infinite time-evolving block decimation algorithm for long-range multidimensional quantum many-body systems,* Physical Review B **102**, 035115 (2020).

[219] M. Suzuki, *Generalized Trotter's formula and systematic approximants of exponential operators and inner derivations with applications to many-body problems,* Communications in Mathematical Physics **51**, 183 (1976).

[220] H. F. Trotter, *On the Product of Semi-Groups of Operators,* Proceedings of the American Mathematical Society **10**, 545 (1959).

[221] M. Fishman, S. R. White, and E. M. Stoudenmire, *The ITensor Software Library for Tensor Network Calculations,* SciPost Phys. Codebases , 4 (2022).

[222] M. Fishman, S. R. White, and E. M. Stoudenmire, *Codebase release 0.3 for ITensor,* SciPost Phys. Codebases , 4 (2022).

[223] S. S. Gubser, C. Jepsen, Z. Ji, and B. Trundy, *Mixed field theory,* J. High Energ. Phys. **2019**, 1 (2019).

[224] F. Q. Gouvêa, *p-adic Numbers*, 3rd ed. (Springer, Cham, 1997).

[225] A. Monna, *Sur une transformation simple des nombres P-adiques en nombres reels,* Indagationes Mathematicae (Proceedings) **55**, 1 (1952).

[226] A. Huang, B. Stoica, and S.-T. Yau, *General relativity from p-adic strings,* Advances in Theoretical and Mathematical Physics (2019).

[227] M. Heydeman, M. Marcolli, I. Saberi, and B. Stoica, *Tensor networks, p-adic fields, and algebraic curves: arithmetic and the AdS_3/CFT_2 correspondence,* arXiv: High Energy Physics - Theory (2016).

[228] B. Stoica, *Building Archimedean Space,* arXiv: High Energy Physics - Theory (2021).

[229] S. S. Gubser, M. Heydeman, C. Jepsen, M. Marcolli, S. Parikh, I. Saberi, B. Stoica, and B. Trundy, *Edge length dynamics on graphs with applications to p-adic AdS/CFT,* J. High Energ. Phys. **2017**, 157 (2017).

[230] S. S. Gubser, J. Knaute, S. Parikh, A. Samberg, and P. Witaszczyk, *p-adic AdS/CFT,* Communications in Mathematical Physics **352**, 1019–1059 (2017).

[231] Y. Bao, M. Block, and E. Altman, *Finite-Time Teleportation Phase Transition in Random Quantum Circuits,* Physical Review Letters **132**, 030401 (2024).

[232] K. Binder, *Finite Size Scaling Analysis of Ising Model Block Distribution Functions,* Zeitschrift für Physik B Condensed Matter **43**, 119 (1981).

[233] O. Melchert, H. G. Katzgraber, and M. A. Novotny, *Site- and bond-percolation thresholds in K n , n-based lattices: Vulnerability of quantum annealers to random qubit and coupler failures on chimera topologies,* Physical Review E **93**, 042128 (2016).

[234] V. Privman and M. E. Fisher, *Universal critical amplitudes in finite-size scaling,* Physical Review B **30**, 322 (1984).

[235] O. Melchert, *autoScale.py - A program for automatic finite-size scaling analyses: A user's guide,* "arXiv-physics.comp-ph" (2009).

[236] A. Sorge, Pyfssa 0.7.6, (2015).

[237] D. Barredo, S. de Léséleuc, V. Lienhard, T. Lahaye, and A. Browaeys, *An Atom-by-Atom Assembler of Defect-Free Arbitrary Two-Dimensional Atomic Arrays,* Science **354**, 1021 (2016).

[238] S. H. Shenker and D. Stanford, *Stringy Effects in Scrambling,* Journal of High Energy Physics **2015**, 132 (2015).

[239] X. Chen and T. Zhou, *Quantum chaos dynamics in long-range power law interaction systems,* Physical Review B **100**, 064305 (2019).

[240] S. Xu and B. Swingle, *Locality, Quantum Fluctuations, and Scrambling,* Physical Review X **9**, 031048 (2019).

[241] T. Zhou and X. Chen, *Operator dynamics in a Brownian quantum circuit,* Physical Review E **99**, 052212 (2019).

[242] T. Zhou, S. Xu, X. Chen, A. Guo, and B. Swingle, *Operator Lévy Flight: Light Cones in Chaotic Long-Range Interacting Systems,* Physical Review Letters **124**, 180601 (2020).

[243] G. S. Bentsen, S. Sahu, and B. Swingle, *Measurement-induced purification in large-N hybrid Brownian circuits,* Physical Review B **104**, 094304 (2021).

[244] S. Sahu, S.-K. Jian, G. Bentsen, and B. Swingle, *Entanglement phases in large-n hybrid Brownian circuits with long-range couplings,* Physical Review B **106**, 224305 (2022).

[245] F. J. Dyson, *Existence of a phase-transition in a one-dimensional Ising ferromagnet,* Communications in Mathematical Physics **12**, 91 (1969).

[246] M. E. Fisher, S.-k. Ma, and B. G. Nickel, *Critical Exponents for Long-Range Interactions,* Physical Review Letters **29**, 917 (1972).

[247] S. A. Cannas, *One-dimensional Ising model with long-range interactions: A renormalization-group treatment,* Physical Review B **52**, 3034 (1995).

[248] A. J. Daley, H. Pichler, J. Schachenmayer, and P. Zoller, *Measuring Entanglement Growth in Quench Dynamics of Bosons in an Optical Lattice,* Physical Review Letters **109**, 020505 (2012).

[249] R. Islam, R. Ma, P. M. Preiss, M. Eric Tai, A. Lukin, M. Rispoli, and M. Greiner, *Measuring entanglement entropy in a quantum many-body system,* Nature **528**, 77 (2015).

[250] A. Jamiołkowski, *Linear transformations which preserve trace and positive semidefiniteness of operators,* Reports on Mathematical Physics **3**, 275 (1972).

[251] M.-D. Choi, *Completely positive linear maps on complex matrices,* Linear Algebra and its Applications **10**, 285 (1975).

[252] T. Brydges, A. Elben, P. Jurcevic, B. Vermersch, C. Maier, B. P. Lanyon, P. Zoller, R. Blatt, and C. F. Roos, *Probing entanglement entropy via randomized measurements,* Science **364**, 260 (2019).

[253] A. Elben, S. T. Flammia, H.-Y. Huang, R. Kueng, J. Preskill, B. Vermersch, and P. Zoller, *The randomized measurement toolbox,* Nature Reviews Physics **5**, 9 (2023).

[254] M. Saffman, T. G. Walker, and K. Mølmer, *Quantum information with Rydberg atoms,* Rev. Mod. Phys. **82**, 2313 (2010).

[255] M. Morgado and S. Whitlock, *Quantum simulation and computing with Rydberg-interacting qubits,* AVS Quantum Science **3**, 023501 (2021).

[256] J. Beugnon, C. Tuchendler, H. Marion, A. Gaëtan, Y. Miroshnychenko, Y. R. P. Sortais, A. M. Lance, M. P. A. Jones, G. Messin, A. Browaeys, and P. Grangier, *Two-dimensional transport and transfer of a single atomic qubit in optical tweezers,* Nature Phys **3**, 696 (2007).

[257] M. Endres, H. Bernien, A. Keesling, H. Levine, E. R. Anschuetz, A. Krajenbrink, C. Senko, V. Vuletic, M. Greiner, and M. D. Lukin, *Atom-by-Atom Assembly of Defect-Free One-Dimensional Cold Atom Arrays,* Science **354**, 1024 (2016).

[258] D. Barredo, V. Lienhard, S. de Léséleuc, T. Lahaye, and A. Browaeys, *Synthetic three-dimensional atomic structures assembled atom by atom,* Nature **561**, 79 (2018).

[259] D. Aldous and P. Diaconis, *Shuffling cards and stopping times,* The American Mathematical Monthly **93**, 333 (1986).

[260] P. Diaconis, R. L. Graham, and W. M. Kantor, *The mathematics of perfect shuffles,* Advances in Applied Mathematics **4**, 175 (1983).

[261] M. D. Lukin, M. Fleischhauer, R. Cote, L. M. Duan, D. Jaksch, J. I. Cirac, and P. Zoller, *Dipole Blockade and Quantum Information Processing in Mesoscopic Atomic Ensembles,* Physical Review Letters **87**, 037901 (2001).

[262] R. Heidemann, U. Raitzsch, V. Bendkowsky, B. Butscher, R. Low, L. Santos, and T. Pfau, *Evidence for Coherent Collective Rydberg Excitation in the Strong Blockade Regime,* Physical Review Letters **99**, 163601 (2007).

[263] M. M. Muller, M. Murphy, S. Montangero, T. Calarco, P. Grangier, and A. Browaeys, *Implementation of an experimentally feasible controlled-phase gate on two blockaded Rydberg atoms,* Physical Review A **89**, 032334 (2014).

[264] L. S. Theis, F. Motzoi, F. K. Wilhelm, and M. Saffman, *High-fidelity Rydberg-blockade entangling gate using shaped, analytic pulses,* Physical Review A **94**, 032306 (2016).

[265] L. Isenhower, E. Urban, X. L. Zhang, A. T. Gill, T. Henage, T. A. Johnson, T. G. Walker, and M. Saffman, *Demonstration of a Neutral Atom Controlled-NOT Quantum Gate,* Physical Review Letters **104**, 010503 (2010).

[266] I. S. Madjarov, J. P. Covey, A. L. Shaw, J. Choi, A. Kale, A. Cooper, H. Pichler, V. Schkolnik, J. R. Williams, and M. Endres, *High-fidelity entanglement and detection of alkaline-earth Rydberg atoms,* Nat. Phys. **16**, 857 (2020).

[267] A. S. Buyskikh, M. Fagotti, J. Schachenmayer, F. Essler, and A. J. Daley, *Entanglement growth and correlation spreading with variable-range interactions in spin and fermionic tunneling models,* Phys. Rev. A **93**, 053620 (2016).

[268] J. Schachenmayer, B. P. Lanyon, C. F. Roos, and A. J. Daley, *Entanglement Growth in Quench Dynamics with Variable Range Interactions,* Physical Review X **3**, 031015 (2013).

[269] D. Porras and J. I. Cirac, *Effective Quantum Spin Systems with Trapped Ions,* Physical Review Letters **92**, 207901 (2004).

[270] V. Borish, O. Marković, J. A. Hines, S. V. Rajagopal, and M. Schleier-Smith, *Transverse-field ising dynamics in a Rydberg-dressed atomic gas,* Physical Review Letters **124**, 063601 (2020).

[271] P. Schauss, *Quantum simulation of transverse ising models with Rydberg atoms,* Quantum Science and Technology **3**, 023001 (2018).

[272] H.-Y. Huang, R. Kueng, and J. Preskill, *Predicting many properties of a quantum system from very few measurements,* Nature Physics **16**, 1050–1057 (2020).

[273] J. P. Covey, I. S. Madjarov, A. Cooper, and M. Endres, *2000-Times Repeated Imaging of Strontium Atoms in Clock-Magic Tweezer Arrays,* Physical Review Letters **122**, 173201 (2019).

[274] M. A. Norcia, A. W. Young, and A. M. Kaufman, *Microscopic Control and Detection of Ultracold Strontium in Optical-Tweezer Arrays,* Physical Review X **8**, 041054 (2018).

[275] M. A. Norcia, A. W. Young, W. J. Eckner, E. Oelker, J. Ye, and A. M. Kaufman, *Seconds-scale coherence on an optical clock transition in a tweezer array,* Science **366**, 93–97 (2019).

[276] A. Cooper, J. P. Covey, I. S. Madjarov, S. G. Porsev, M. S. Safronova, and M. Endres, *Alkaline-Earth Atoms in Optical Tweezers,* Physical Review X **8**, 041055 (2018).

[277] I. S. Madjarov, A. Cooper, A. L. Shaw, J. P. Covey, V. Schkolnik, T. H. Yoon, J. R. Williams, and M. Endres, *An Atomic-Array Optical Clock with Single-Atom Readout,* Physical Review X **9**, 041052 (2019).

[278] S. Saskin, J. T. Wilson, B. Grinkemeyer, and J. D. Thompson, *Narrow-Line Cooling and Imaging of Ytterbium Atoms in an Optical Tweezer Array,* Physical Review Letters **122**, 143002 (2019).

[279] M. H. Muñoz Arias, I. H. Deutsch, and P. M. Poggi, *Phase-Space Geometry and Optimal State Preparation in Quantum Metrology with Collective Spins,* PRX Quantum **4**, 020314 (2023).

[280] T. Zibold, E. Nicklas, C. Gross, and M. K. Oberthaler, *Classical Bifurcation at the Transition from Rabi to Josephson Dynamics,* Physical Review Letters **105**, 204101 (2010).

[281] M. J. Martin, M. Bishof, M. D. Swallows, X. Zhang, C. Benko, J. von Stecher, A. V. Gorshkov, A. M. Rey, and J. Ye, *A Quantum Many-Body Spin System in an Optical Lattice Clock,* Science **341**, 632 (2013).

[282] M. A. Perlin, C. Qu, and A. M. Rey, *Spin Squeezing with Short-Range Spin-Exchange Interactions,* Physical Review Letters **125**, 223401 (2020).

[283] A. S. T. Pires, *Theoretical Tools for Spin Models in Magnetic Systems*, 2053-2563 (IOP Publishing, 2021).

[284] D. D. Stancel and A. Prabhakar, *Spin Waves: Theory and Applications* (Springer, Berlin, 2009).

[285] C. Kittel, *Quantum Theory of Solids* (Wiley, New York, 1963).

[286] H. Labuhn, D. Barredo, S. Ravets, S. de Léséleuc, T. Macrì, T. Lahaye, and A. Browaeys, *Tunable two-dimensional arrays of single Rydberg atoms for realizing quantum ising models,* Nature **534**, 667–670 (2016).

[287] C. Gardiner and P. Zoller, *Quantum Noise*, 3rd ed., Springer Series in Synergetics (Springer Berlin, Heidelberg, 2004) pp. XXII, 450.

[288] C. Fromonteil, R. Tricarico, F. Cesa, and H. Pichler, *Hamilton-jacobi-bellman equations for Rydberg-blockade processes,* Physical Review Research **6**, 033333 (2024).

[289] L. Postler, S. Heu en, I. Pogorelov, M. Rispler, T. Feldker, M. Meth, C. D. Marciniak, R. Stricker, M. Ringbauer, R. Blatt, P. Schindler, M. Müller, and T. Monz, *Demonstration of fault-tolerant universal quantum gate operations,* Nature **605**, 675–680 (2022).

[290] R. Barends, J. Kelly, A. Megrant, A. Veitia, D. Sank, E. Jeffrey, T. C. White, J. Y. Mutus, A. G. Fowler, B. Campbell, Y. Chen, Z. Chen, B. Chiaro, A. Dunsworth, I.-C. Hoi, C. Neill, P. J. J. O'Malley, C. Quintana, P. Roushan, A. Vainsencher, J. Wenner, A. N. Cleland, and J. M. Martinis, *Superconducting quantum circuits at the surface code threshold for fault tolerance,* Nature **508**, 500 (2014).

[291] D. Nigg, M. Müller, E. A. Martinez, P. Schindler, M. Hennrich, T. Monz, M. A. Martin-Delgado, and R. Blatt, *Quantum computations on a topologically encoded qubit,* Science **345**, 302–305 (2014).